REPORT DOCUMENTATION PAGE

Form Approved
OMB No. 0704-0188

1. REPORT DATE *(DD-MM-YYYY)*	2. REPORT DATE	3. DATES COVERED *(From - To)*
08-09-2000	Third Annual Report	15/08/99 - 15/08/00

4. TITLE AND SUBTITLE

1997 MURI in RF Photonics: RF Photonics for Array Processing

5a. CONTRACT NUMBER

5b. GRANT NUMBER
MURI 1997 GN00014-97-1-1006

5c. PROGRAM ELEMENT NUMBER

6. AUTHOR(S)

Kelvin H. Wagner, University of Colorado, Boulder
Dana Anderson, University of Colorado, Boulder
Zoya Popovic, University of Colorado, Boulder
Randall W. Babbitt, Montana State University
Andre Kroessen, University of California, Davis
Lloyd Griffiths, George Mason University

5d. PROJECT NUMBER

5e. TASK NUMBER

5f. WORK UNIT NUMBER

7. PERFORMING ORGANIZATION NAME(S) AND ADDRESS(ES)

University of Colorado,
Optoelectronic Computing Systems Center,
Campus Box 525
Boulder, CO 80309

8. PERFORMING ORGANIZATION REPORT NUMBER

153 6702

9. SPONSORING/MONITORING AGENCY NAME(S) AND ADDRESS(ES)

Dr William Miceli,
Office of Naval Research, Code 313,
Ballston Tower #1,
Arlington, VA 22217

Dr Stephen A. Pappart
US Navy SPAWAR Systems Center
SSC-SD D825
53560 Hull St,
San Diego, CA 92152-5001

10. SPONSOR/MONITOR'S ACRONYM(S)

11. SPONSORING/MONITORING AGENCY REPORT NUMBER

12. DISTRIBUTION AVAILABILITY STATEMENT

Unlimited

13. SUPPLEMENTARY NOTES
Funded by OSD DDR&E

14. ABSTRACT
This report covers the third year of progress of the 1997 MURI on RF Photonics for Antenna Arrays at the University of Colorado, Montana State University, George Mason University, and the University of California Davis. Novel techniques for optical control and processing of the wideband RF and microwave signals encountered in phased array antennas are being developed, guided by research in spatio-temporal adaptive processing algorithms and active quasi-optical RF antenna arrays. The primary goal of this research is to develop enabling optical techniques that provide dramatic improvements in antenna array performance over conventional RF, optical, and digital techniques, allowing the efficient processing of large broadband antenna arrays. Coherent modulation and detection is made robust and practical by the use of dynamic holography in photorefractive and optical coherent transient media. This report summarizes the teams management, educational, and outreach activities, as well as the 3rd years technical progress on the constituent projects - broadband adaptive optical array processing, spatio-temporal array-processing algorithms, coherent-transient true-time-delay, photorefractive signal extraction, optical antenna control, and polymer in-line fiber modulators.

15. SUBJECT TERMS

Phased Array Antennas, coherent transients, photorefractive, RF photonics, STAP processing

16. SECURITY CLASSIFICATION OF:			17. LIMITATION OF ABSTRACT	18. NUMBER OF PAGES	19a. NAME OF RESPONSIBLE PERSON
a. REPORT	**b. ABSTRACT**	**c. THIS PAGE**	Unlimited - UL	112	
Unclassified	Unclassified	Unclassified			**19b. TELEPONE NUMBER** *(Include area code)*

Standard Form 298 (Rev. 8-98)
Prescribed by ANSI-Std Z39-18

2000 1101 115

RF Photonics for Array Processing

MURI third annual report - August 2000

Attention: **Dr. William Miceli,**

ONR 313, 800 N Quincy St., Arlington, VA 22217-5660

Principal Investigator: **Kelvin Wagner,** *CU-ECE*

Dept. of ECE and OCS, Box 425, University of Colorado, Boulder CO, 80309-0425

kelvin@optics.colorado.edu, (303)-492-4661 (5810 FAX)

http://optics.colorado.edu/MURI

University of Colorado Co-PI:	**Dana Anderson,**	*CU-Physics*
University of Colorado Co-PI:	**Zoya Popović,**	*CU-ECE*
George Mason University Co-PI:	**Lloyd Griffiths,**	*GMU-EE*
Montana State University Co-PI:	**Randall Babbitt,**	*MSU-Phys*
University of California at Davis Co-PI:	**Andre Knoesen,**	*UCD-ECE*

Contents

20001101 115

1 3rd Year Executive Summary

This report summarizes the third year of the MURI in RF Photonic Systems which assembles the University of Colorado, the University of California-Davis, Montana State University, and George Mason University into a systems oriented research team investigating the application of photonic techniques to the control and processing of RF phased arrays. Under this MURI funding, the prime contract is administered through the University of Colorado under the direction of Prof. Kelvin Wagner.

Photonic techniques are emerging as the preferred approach to a wide variety of RF tasks throughout the microwave/millimeter-wave bands, including transmission, controlling time delay, spectral filtering, mixing, frequency generation, antenna array control, beam forming, wide-band signal processing, and target recognition. Much of this development has been driven by the evolution of high frequency photonic devices such as 100 GHz detectors, 40 GHz modulators, 20 GHz lasers, and 10 THz fiber optic transmission and delay lines. The desire to find applications for these technologies often leads to the direct replacement of individual RF components with their optical counterparts, and relies on the smaller size and lighter weight of the optical components and waveguides to yield a resulting system advantage. More sophisticated applications utilize the incredibly large bandwidth of optical transmission to simultaneously wavelength-multiplex a large number of RF signals for efficient parallel transmission or to control the element time delays through dispersion. The approach of this MURI team takes RF photonics to a third level of sophistication, in which the massive parallelism possible using dynamic volume holography in photorefractive and photon-echo materials enables the implementation of optimal adaptive and nonlinear algorithms for array processing in the optical domain.

Several such RF photonic techniques are being pursued, and this MURI team is building on the strengths of each approach, and identifying the optimal combination of devices, materials, algorithms, and systems. The BEAMTAP approach (Broadband and Efficient Adaptive Method for True-time-delay Array Processing) is being investigated theoretically and implemented experimentally to demonstrate efficient adaptive beam forming using acousto-optic deflectors, traveling-fringes detectors, and photorefractive adaptive weights. The novel physics of optical coherent transients are being developed for applications as programmable RF time delays as well as array signal processors, since these nonlinear materials can directly produce the necessary delayed

RF signals as photon echoes. Both of these approaches utilize coherent beam forming in the optical domain which can improve the noise figure of optically remoted arrays and optical novelty filtering developed at CU can enable robust RF signal combination even in the presence of phase errors and drifts. Optically controlled quasi-optical active antenna arrays provide a near term test vehicle for optical controlled arrays, allowing rapid switching between polarizations, transmit/receive (T/R) mode, and frequency response, and in addition will demonstrate the capability of producing multiple simultaneous true-time-delay (TTD) beams as a front end for beam-space adaptive optical processors. Optical nonlinearities are being explored as an approach to dynamically solving the problem of signal extraction from small RF antenna arrays. Practical polymeric in-line fiber (PILF) modulators with high-speed coplanar waveguide (CPW) electrode structures are being developed as the front end RF-to-optical transducers for the antenna arrays. All of these efforts are being tied together by investigations of spatio-temporal signal processing algorithms compatible with RF photonic technology, which allows us to evaluate and compare the various optical systems techniques being investigated.

2 Education, Presentations, Outreach, and Management

2.1 MURI Team

This MURI effort has directly or indirectly funded the 6 principal investigators, 5 postdoctoral or visiting research scientists, 12 graduate students, 11 undergraduate students, 2 research assistants, and fractions of a financial manager and secretary.

2.1.1 Principal Investigators

The original MURI team of 6 PIs was joined by Andre Knoesen from UC Davis last year, and this year Ted Weverka working under MURI funding at Photonics Data Systems left the MURI team to form a new company called Network Photonics. Much of the equipment from Photonics Data Systems has been transferred to the University of California at Davis where Prof. Andre Knoesen will continue the work on PILF modulators. Weverka's project on coherent optical beam combination for phased array processing will be continued at the University of Colorado as the required front end to the BEAMTAP processor.

Table 1: Principal investigators involved in the RF Photonic Systems program.
* indicates that Weverka ended his participation in the MURI team in Jan 2000.

Researcher	Department	Institution
Kelvin Wagner	ECE/OCS	CU-Boulder
Zoya Popović	ECE	CU-Boulder
Dana Anderson	JILA	CU-Boulder
William Randall Babbitt	Physics	Montana State University
Lloyd Griffiths	ITE	George Mason University
Andre Knoesen	ECE	UC-Davis
Robert Ted Weverka*		Photonic Data Systems

2.2 Students, Post-Doctoral Researchers, and other Personnel

Table 2: MURI personnel indicating those funded by this program. Those who worked on closely related projects in collaboration with the MURI effort are indicated by *.

Researcher	Status	Position	Advisor	Dept.	Inst.
G.S.Pati	new 9/99 -	Post-doc	Wagner	OCS	CU
Kris Merkel	50%	Post-doc	Babbitt	Physics	MSU
Kevin Repasky	continuing	Post-doc	Babbitt	Physics	MSU
Mingzhen Tian	continuing	Post-doc	Babbitt	Physics	MSU
Diego Yankelevich	3/99-present	Adjunct Prof.	Knoesen	EE	Davis
Joe Shamir	8/00-10/00	Visiting MURI fellow	Wagner	OCS	CU
Vladimir Shkunov	continuing	Res. Ass. -2/00	Anderson	JILA	CU
Edilene Fotheringham	continuing	Grad Student	Anderson	JILA	CU
Valeria Damiao	continuing	Grad Student	Anderson	JILA	CU
Amy Sullivan*	Spring00 OSEP	Grad Student	Anderson	JILA	CU
Greg Kriehn	DoD fellowship	Grad Student	Wagner	OCS	CU
Paulo Silveira	continuing	Grad Student	Wagner	OCS	CU
Friso Schlottau	new 9/99-	Grad Student	Wagner	OCS	CU
Ken Anderson*	continuing	Grad Student	Wagner	OCS	CU
Jim Vian	continuing	Grad Student	Popović	ECE	CU
Darko Popovic*	continuing	Grad Student	Popović	ECE	CU
Paul Smith*	New PhD 6/00	Grad Student	Popović	ECE	CU
Bob Peters*	continuing	Grad Student	Babbitt	Physics	MSU
Randy Reibel	new(1/00)	Grad Student	Babbitt	Physics	MSU
Ijaz Zafarullah	new(5/00)	Grad Student	Babbitt	Physics	MSU
Jun Zhoa	finished (1/00)	Grad Student	Babbitt	Physics	MSU
John Campbell	new 6/00-	Grad student	Knoesen	EE	Davis
Liu Ming Wu	new 2/00-	Grad student	Knoesen	EE	Davis
Sam Weaver	left Feb 2000	Prof. Res. Asst.	Wagner	OCS	CU
Leslie Czaia	continuing	Prof. Res. Asst.	Anderson	JILA	CU
Pete Kirkpatrick	finished 12/99	BS/MS student	Popović	OCS	CU
Buz Smith	continuing	Financial Admin.		OCS	CU

Table 3: Undergraduate students who have been involved in MURI related research during the past year. Again, those who worked on closely related projects in collaboration with the MURI effort are indicated by *.

Undergrad	Status	Position	Advisor	Dept.	Inst.
Eric Hoyt	continuing	Undergraduate	Wagner	OCS	CU
Jack Hong Loui	Senior project	Undergraduate	Popović	ECE	CU
Paul Smith	Senior project	Undergraduate	Popović	ECE	CU
Alex Morrow	Senior project	Undergraduate	Popović	ECE	CU
Tom Miller	Senior project	Undergraduate	Popović	ECE	CU
Heidi Becker	Summer REU	Undergraduate	Anderson	Phys	CU
Kevin Henderson	REU	Undergraduate	Anderson	Phys	CU
John Jost	Assistant	Undergraduate	Anderson	Phys	CU
Joe Fischer*	continuing	Undergrad	Babbitt	Physics	MSU
Joe Galbraith*	graduated	Undergrad	Babbitt	Physics	MSU
Zeb Barber	new(5/00)	Undergrad	Babbitt	Physics	MSU

2.2.1 Students Graduated from the MURI program

1. Jun Zhao, January 2000, MSU, MS

2. Xiaofang Chen, May 2000, MSU MS

3. Pete Kirkpatrick, December 1999, CU BS/MS.

4. Scott A. Hamilton, Ph.D., Dissertation Title: Traveling Wave In-Line Directional Coupler Modulator, 1999, UC Davis.

5. Carl Arft, MS, Spring 2000, UC Davis.

This coming year several MURI students are expected to graduate including for example Jim Vian, Valeria Damiao, Paulo Silveira, and Ken Anderson.

2.3 Meetings

The Boulder team meets weekly to exchange information, make presentations, as well as to discuss technical and management details. The entire MURI team gathers twice a year for intellectual exchange, discussions, and review regarding scientific progress during the year. One of these meetings is primarily an internal MURI meeting, and the other is a formal review for programmatic purposes. Our second annual review was held in conjunction with the UCLA MURI review at UCLA on Dec 14 1999. The 3rd annual review will be held again jointly with the UCLA MURI team in Boulder on Oct 12-13.

2.3.1 Second Annual review

Our second annual review was held December 14, 1999 in Los Angeles at UCLA in conjunction with the third annual UCLA MURI review held on the following day. It was attended by the 7 MURI PIs, 4 of the CU MURI students, and about 20 industrial advisors and government reviewers. The view graphs from this meeting are available on the web at our MURI home page http://optics.colorado.edu/MURI/review99.

2.3.2   2nd Annual review schedule

DECEMBER 14th UNIVERSITY OF COLORADO MURI REVIEW

Time	Name	Organization	Title
8:00 - 8:30	—— Continental Breakfast ——		
8:30 - 8:35	Kelvin Wagner	(CU)	Welcome
8:35 - 8:45	Bill Miceli	(ONR)	DoD MURI Program Goals
8:45 - 9:15	Kelvin Wagner	(CU)	RF Photonic Systems Program Overview
9:15 - 9:45	Greg Kriehn	(CU)	BEAMTAP
9:45 - 10:00	Paul Biernacki	(NRL)	Fiber based photonic array steering
10:00 -10:30	Ted Weverka	(PDS)	Coherent Optical Array Processing
10:30 - 10:45	—— Coffee Break ——		
10:45 -11:00	Lloyd Griffiths	(GMU)	Issues in STAP
11:00 - 11:30	R. Babbitt	(MSU)	Coherent Transient True Time Delay
11:30 - 12:00	Andre Knoesen	(UC-Davis)	PILF modulators
12:00 - 12:30	Feedback on Morning Session		
12:30 - 1:30	—— Buffet Lunch Break ——		
1:30 - 1:45	Arnold Van Ardenne	(NFRA)	SKA and RF Photonics
1:45 - 2:00	Zoya Popovic	(CU)	Quasi-optical arrays
2:00 - 2:15	Jim Vian	(CU)	Optically controlled T/R antenna
2:15 - 2:30	Daniel Dolfi	(Thomson)	TTD & RF Photonics at
Thomson			
2:30 - 3:00	Dana Anderson	(CU)	Dynamic Holography for RF photonics
3:00 - 3:10	Zoya Popovic	(CU)	RF/Optical Techniques
class			
3:10 - 3:30	Feedback on Afternoon Session		
3:30 - 4:00	—— Coffee Break ——		
4:00 - 4:30	Planning for 2000 for RF Photonic Systems Research		
4:30 - 5:00	Additional steering committee feedback		

2.3.3 2nd Annual review attendees

University of California at Los Angeles, December 14, 1999

Name	Organization	Contact Info
Dr. Bill Miceli, Sponsor	ONR	wmiceli@onreur.navy.mil
Prof. Kelvin Wagner, PI	CU - OCS	kelvin@colorado.edu
Prof. Dana Anderson, PI	CU - Physics	dana@colorado.edu
Prof. Randy Babbitt, PI	MSU	babbitt@physics.montana.edu
Prof. Lloyd Griffiths, PI	GMU	griffiths@gmu.edu
Prof. Andre Knoesen, PI	UC - Davis - ECE	knoesen@ece.ucdavis.edu
Prof. Zoya Popovic, PI	CU - ECE	zoya@colorado.edu
Mr. Ted Weverka, PI	Photonic Data Systems	weverka@pacbell.net
Ms. Edilene Fotheringham, GRA	CU - Physics (Anderson)	fotherin@jilau1.colorado.edu
Mr. Greg Kriehn, GRA	CU - OCS (Wagner)	kriehn@colorado.edu
Ms. Ming Zhen Tian, GRA	MSU - Physics	tian@physics.montana.edu
Mr. Jim Vian, GRA	CU - ECE (Popovic)	vian@colorado.edu
Dr. Arnold van Ardenne	NFRA	ardenne@nfra.nl
Dr. Paul Biernacki	NRL	biernack@ccf.nrl.navy.mil
Dr. Jaap Bregman	NFRA	bregman@nfra.nl
Dr. Daniel Dolfi	Thomson-CSF/LCR	daniel.d.d.dolfi@lcr.thomson.fr
Dr. John Gallo	BAE Systems	
Dr. Anthony Jacomb-Hood	Lockheed Martin M&S	anthony.w.jacombhood@lmco.com
Dr. Kyung Kim	Lockheed Martin TAS	
Dr. Stuart Kingsley	SRICO, Inc.	
Dr. Jian Ma	Rockwell Science Center	ma@rsc.rockwell.com
Dr. Michael Nesnidal	Focused Research	
Dr. Irwin Newberg	Raytheon	
Dr. James Nichter	AFRL	
Dr. Steve Pappert	SPAWAR	spappert@nosc.mil
Dr. Azad Siahmakoun	Rose-Hulman Inst of Tech	
Dr. Richard Sparks	MTT-S	
Mr. Michael St. John	St. John Scientific, LLC	
Dr. Gregory Tangonan	HRL Laboratories	tangonan@hrl.hac.com
Dr. Larry Thomas	Toyon Research Corp	
Dr. Timothy Van Eck	Lockheed Martin M&S	
Dr. Michael VanBlaricum	Toyon Research Corp	mikevanb@toyon.com
Dr. George Webb	Innova Labs Inc/UCSD	
Prof. Ming Wu	UCLA	wu@ee.ucla.edu
Dr. Daniel Yap	HRL Laboratories	

2.3.4 3rd year MURI team Interactions

1. Nov 17 1999: Visit by Charles Garvin of CTI to discuss collaboration on RF photonics, LIDAR, and optical processing.

2. Nov. 19, 1999: Presentation by G. Kriehn on BEAMTAP at OCS retreat.

3. Nov 19, 1999: Presentation by K. Anderson on photon echo array processing at OCS retreat.

4. Dec 14, 1999: CU MURI Review at UCLA attended by Wagner, Popović, Anderson, Griffiths, Babbitt, Weverka, Knoesen, Fotheringham, Kriehn, Tian, Vian, and 20 industry and government advisors.

5. Dec 15, 1999: Researchers including Wagner, Babbitt, Knoesen, Fotheringham, Kriehn, Tian, and Vian attended UCLA MURI review.

6. Dec 20-21, 1999: Jaap Bregman from NFRA visits CU to discuss RF photonics collaborations with Wagner, Popović, Vian, Kriehn, and Schlottau.

7. Jan 7, 2000: Greg Kriehn presents BEAMTAP talk at URSI annual meeting in Boulder.

8. Jan 31, 2000 Dave Carrott from Task visits to discuss with Wagner past and future collaborations with Litton on Optical RF Processing.

9. Feb 11, 2000: Jim Harvey from ARO visits to discuss upcoming programs in RF and Photonics with Wagner and Popović.

10. Feb 13, 2000: Dave Brady from University of Illinois visits to discuss possible collaborations in integrated sensor processing.

11. Feb 16-18, 2000: Wagner and Kriehn attend PSAA meeting in Monterey.

12. March 13, 2000: Dave Pepper from Hughes visits CU Boulder to discuss collaborations with Anderson, Wagner, and Popović.

13. March 21, 2000: Ted Weverka of Network Photonics meets with Wagner to discuss future collaborations extending ideas developed in the MURI to fiber optics communication. Joint development of multimode fiber dispersion compensation system planned.

14. March 29-30, 2000: Wagner attends OIDA roadmap planning meeting for RF Photonics in LA.

15. April 7, 2000: Wagner and Babbitt visit Boeing to present MURI research to Geoff White and Michael Hamilton. Agreement to collaborate and to provide access to Boeing array technology is discussed.

16. May 14-17, 2000: Jean-Louis Legouet from CNRS in Orsay visits for collaborations and experiments on spectral hole burning processing of RF signals.

17. May 14-July 20, 2000 Loic Menagere from CNRS in Orsay visits for extended collaborations and experiments on spectral hole burning processing of RF signals.

18. May 17, 2000: Kelvin visits Sanders for discussions on optical processing.

19. May 25-26, 2000: Wagner attends Acoustooptic-2000 meeting in Brugge, Belgium

20. May 29-30,2000: Wagner visits Jaap Bregman at NFRA in Netherlands for discussion on array processing for the Square Kilometer Array (SKA) and the applications of RF photonic techniques.

21. May 31, 2000: Wagner visits Daniel Dolfi at Thomson for collaborations on traveling fringes detectors developed at Thomson in BEAMTAP processor.

22. June 18-23, 2000: Silviera attends Optics in Computing 2000 in Quebec City and presents sonar array processing results.

23. June 29, 2000: Wagner visits Honeywell for discussions on radar imaging.

24. June 30, 2000: Wagner attends WOMBAT kickoff meeting at Rose-Hulman Institute of Technology as a member of the advisory board to this Navy center in RF photonics.

25. July 9-12, 2000: Visit by Kelvin Wagner and Ken Anderson to Bozeman, to attend Persistent Spectral Hole Burning Meeting in Big sky.

26. July 12-22, 2000: Ken Anderson works with Kris Merkel at MSU Bozeman on photon echo processing for phased arrays, demonstrates TTD array steering using novel acoustooptic technique (patent pending).

27. Aug 6-8, 2000: Wagner attends the DARPA Integrated Signal Processing workshop organized by Dave Brady and held in Boulder. Presented BEAMTAP as an ISP system.

28. Aug 11-14, 2000: Lloyd Griffiths visits Boulder for discussions with Wagner, Popović, Vian, Kriehn, and Silveira.

29. Aug 4-Oct 20, 2000: Joseph Shamir from Technion in Israel visits with the CU MURI team and collaborates with Wagner on analyzing the BEAMTAP processor using operator algebra.

30. Krishna Mohan of Lund Institute in Sweden has visited with Kris Merkel on several occasions to develop an fiber optic amplifier at 793 nm for optical coherent transient applications. This technology is being transfered to Colorado and a joint JOP grant is to be submitted.

31. Mark Neifeld of the University of Arizona visited with W. R. Babbitt and Spectrum Lab on several occasions to discuss information capacity, signal fidelity, and delay resolution issues in optical coherent transient devices.

32. The Workshop on Applications of Spectral Hole Burning 2000 was held in Big Sky, Montana, July 9-12, 2000, organized by Alan Craig of MSU. Researchers from all over the world came to discuss the physics and applications of optical coherent transient devices.

33. W. R. Babbitt and his group have worked closely on MURI related research with the researchers in the groups of Rufus Cone, Alex Rebane, and John Carlsten of MSU Physics and MSU Spectrum Lab, including Alan E. Craig, Pete Selin, Tiejun Chang, Zack Cole, Alex Dimitrov. Kris Merkel and Kevin Repasky have been jointly funded by Spectrum Lab and the MURI.

34. W. R. Babbitt has started a company, LightSmyth Technologies, with Thomas W. Mossberg of the University of Oregon. The company is exploiting a new device technology processes RF-photonic (multi-GHz) signals in the optical domain, with applications in the optical networking marketplace.

35. Dana Anderson visited Daniel Dolfi and Collaborators at Thomson CSF in Orsay, France, Summer 2000.

36. Diego Yankelvich visited Larry Dalton and collaborators at University of Southern California, June 2000.

37. Frequent visits from Prof. Harris group members to UC Davis.

38. Prof. Shiao Min Tseng visited UC Davis to discuss fabrication of inline fiber coupler, Fall 1999.

2.4 Additional Collaborations and Related Research

The MURI has enabled a wide variety of collaborations among the PIs as well as with other groups. In this section some notable collaborations are discussed and outgrowths from the MURI into new areas are mentioned.

1. Prof. Popović collaborated with Prof. Anderson on the demonstration of a 2-channel optical processor for a quasi-optical (QO) receiving array. A complete system was engineered and characterized, starting from the microwave 10-GHz active antenna front end, to the photodetector and RF demodulator circuits. The system is able to adaptively separate a strong jammer from a signal over shared bandwidth. This could not have been accomplished without multidisciplinary experience in microwave engineering, optics, and electronics. The graduate students involved in the project are now competent in both optics and RF engineering, and the first demonstration of a complete system is now practically completed.

2. Prof. Popović collaborated with Prof. Griffiths on adaptive algorithms for lens array antennas. They have applied an LMS adaptive algorithm to a lens antenna array and compared it to a standard 2-D antenna array in terms of noise and adaptation (learning) speed. They are currently working on a paper that summarizes the results and points to the advantages of quasi-optical arrays for adaptive front ends.

3. Profs. Babbitt and Wagner are working together on a DEPSCOR project that is investigating applications of photon echo processing to radar systems. This additional interaction will greatly benefit the MURI program since it will allow Prof. Wagner to undertake photon echo experiments not supported by the MURI as well as direct Prof. Babbitt's work beyond true-time-delay towards fully adaptive processing. Recent results include a preliminary demonstration of true-time-delay array beam steering using novel acoustooptic steering techniques in combination with chirped photon echoes (patent pending). [DEPSCOR]

4. Prof. Babbitt, PI, Co-founded a new company, LightSmyth Technologies, that uses new device technologies to perform processing of optical signals in telecommunication networks. While these devices are not OCT based, there are many parallels to OCTs and the insights learned will benefit the MURI project. Mingzhen Tian, who has been with the project for two years and is becoming a permanent member of the MSU team as a research scientist, runs the day to day operation of Prof. Babbitt's Coherent Transients Lab. Dr. Kris Merkel and Dr. Kevin Repasky, research scientist in MSU Spectrum Lab, will continue to be part of the MURI team, both directly and in collaborations between MURI and MSU Spectrum Lab.

5. Prof. Knoesen collaborated with Prof. Larry Dalton of the University of Southern California to incorporate the new nonlinear polymeric materials developed by Prof. Larry Dalton into modulator devices.

6. Prof. Knoesen collaborated with Prof. Shiao-Min Tseng of the National Tsing Hua University of Taiwan to obtain long interaction length half-couplers used in in-line modulators.

7. Prof. Knoesen collaborated with Intelligent Fiber Optic Systems Inc., Sunnyvale CA. to extend inline fiber devices to tunable in-line filters.

8. Prof. Knoesen collaborated with Prof. James S. Harris of Stanford University to extend inline fiber concepts to in-line GaAs/AlGaAs modulators, filters, detectors, and emitters.

Other related grants include:

1. "Quasi-optics," ARO MURI in Quasi-Optical Power Combining, Co-PI: Zoya Popović, with Caltech, UCSB and U of Hawaii.

2. "Low-power electronics for wireless," NSF, $1.5 million, Co-PI: Zoya Popović, with Varanasi, Maksimovic, Brown.

3. "Adaptive optical processing for arrays in wireless base stations," NSF, $250K, PIs: Zoya Popović with Dana Anderson. Profs. Popović and Anderson received a NSF grant under the wireless communications initiative to demonstrate how the optical processor developed under this MURI can be applied to wireless channels with interference.

4. "Diversity in wireless systems," NSF wireless program, $800K, Co-PI: Zoya Popović, Scharf, Varanasi, with U of Wisconsin.

5. "Low-power electronics," ARO MURI, Co-PI: Zoya Popović with U of Michigan.

6. "High performance correlators based on spectral hole burning technology", NASA, PI: Alan Craig, Co-investigators: W. R. Babbitt, J. L. Carlsten, and R. L. Cone, $2M/year, 4/99-4/04.

7. "Advanced Coherent Transient Systems and Devices," Air Force Office of Scientific Research, PI: W. R. Babbitt, $457,844 (plus $9,749 cost-share), 3/98- 2/01.

8. "Wide-Band Optical True-Time-Delay and Adaptive Beamforming," Army Research Office PI: W. R. Babbitt, $299,199 (plus $149,899 cost-share) 5/98- 4/01

9. "Optically-controlled RF switch for polarization-diversity wireless communication receiver," NSF wireless program, PIs Zoya Popović, Mahesh Varanasi, Louis Scharf.

10. "MURI in atom optics," PI Dana Anderson.

11. "NSF ITR investigating ultrafast non linear optics switching," $499,000, 2000-2003, PI Kelvin Wagner with Co-PI Frank Wise at Cornell.

12. "Low-index polymer structures integrated in in-line fiber devices", UC Micro in collaboration with intelligent fiber optic systems, $38,080, 1999-2000, PI Andre Knoesen.

13. "Tunable add-drop in-line fiber multiplexer devices for fiber optic systems", UC Core in collaboration with Intelligent Fiber Optic Systems, $183,083, 1999-2001, PIs Andre Knoesen and Diego Yankelvich.

2.4.1 Awards and Honors for the PIs and students

1. "A Transmit/Receive Active Antenna with Fast Low-Power Optical Switching," J. Vian, Z. Popović, *2000 IEEE IMS Symposium Digest*, pp.847–850, Boston, MA, June 2000. *Awarded the 2nd Prize in Best Student Paper Competition. The conference had over 11,000 attendees and about 160 papers competed for Best Student Paper Awards. 3d Prize was shared by Caltech and the University of Michigan.*

2. Prof. Wagner is giving an invited talk at MWP 2000 on BEAMTAP in a special session on Photonic Systems for Arrays.

   Gregory Kriehn, G. S. Pati, Paulo E. X. Silveira, Friso Schlottau, Kelvin H. Wagner, Daniel Dolfi and J. P. Huignard, Demonstration of optical beam forming using BEAMTAP *Invited Talk, IEE Microwave Photonics MWP-2000*, Oxford UK, September 2000.

3. Prof. Popović is also giving an invited talk at MWP 2000 on optically controlled Quasi-optical antennas.

   J. Vian, Z.Popović, "Optical Control of Microwave Circuits and Antennas," *Invited Talk, IEEE MWP Topical Meeting*, Oxford, UK, September 2000.

4. Kelvin H. Wagner, Greg R. Kriehn, Andrew J. M. Kiruluta, and Paulo E. X. Silveira, RF-Photonic adaptive-array processing, *Invited Paper* at SFO Horizons d'optique, Bordeaux, France, Sept 8 1999.

5. K. H. Wagner, K. E. Anderson, K. D. Merkel, and W. R. Babbitt "Photon Echo Adaptive Array Processor" *Invited Paper* presented at 6th Int. Meeting of Hole Burning and Related Spectroscopies: Science and Applications (HBRS'99), September 18-23, 1999, Hourtin, France.

6. RF Photonic Systems for Array Control and Processing – An overview of the RF Photonic Systems for Antenna Arrays MURI, Kelvin H. Wagner, Zoya Popović, Dana Anderson, W. R. Babbitt, L. Griffiths, A. Knoesen, R. T. Weverka, *Invited Paper*, DARPA Photonic Systems for Antenna Applications Symposium, PSAA-10, February 2000.

7. J. Vian, Z.Popović, "Optically-controlled T/R active lens array," *Invited presentation, 1999 URSI General Assembly Digest*, pp.674, Toronto, Canada, August 1999.

8. Zoya Popović was elected Senior Member of the IEEE.

9. Zoya Popović received a Humboldt Research Award from the Alexander von Humboldt Foundation, Germany.

10. OTHER: Two of the Co-PIs have a new daughter, Fiona Popović Anderson, 7 months.

2.5 MURI Publications

2.5.1 Papers published in 2000 (since 8/15/99)

1. K.D. Merkel and W. R. Babbitt, "Optical coherent transient continuously programmed continuous processor," Optics Letters, 24, 172-174 (1999).

2. K. D. Merkel, Z. Cole, and W. R. Babbitt, "Signal correlator with programmable variable time delay based on optical coherent transients," J. of Luminescence, 86 375-382 (2000).

3. K. D. Merkel, R. D. Peters, P. B. Sellin, K. S. Repasky and W. R. Babbitt, "Accumulated programming of a complex spectral grating," accepted for publication in Optics Letters.

4. M. Tian, J. Zhao, Z. Cole, R. Reibel, and W. R. Babbitt, "Dynamics of Broadband Accumulated Spectral Gratings in Tm3+: YAG," submitted to JOSA B.

5. K.D. Merkel, W.R. Babbitt, K.E. Anderson, and K.H. Wagner, "Variable-time delay optical coherent transient signal processing," Optics Letters, 24, 1386-8 (1999). (related paper funded by DEPSCOR or AFOSR)

6. T.L. Harris, Y. Sun, W.R. Babbitt, R.L. Cone, J.A. Ritcey, and R.W. Equall, "Spatial spectral holographic correlator at 1536nm using 30-symbol quadriphase and binary-phase-shift keyed codes," Optics Letters, 25, 85-7 (2000). (related paper funded by DEPSCOR or AFOSR)

7. K. D. Merkel and W. R. Babbitt, "Continuous waveform variable true-time delay by optical coherent transients," Optics Comm. 180, 103-110 (2000). (related paper funded by DEPSCOR or AFOSR)

8. C. Sjaarda Cornish, L. Tsang, and W. R. Babbitt, "Demonstration of highly efficient photon echoes in an absorbing medium," accepted for publication in Optics Letters. (related paper funded by DEPSCOR or AFOSR)

9. Gregory Kriehn, Andrew Kiruluta, Paulo E. X. Silveira, Sam Weaver, Shawn Kraut, Kelvin Wagner, R. Ted Weverka, and Lloyd Griffiths, "Optical BEAMTAP beam-forming and jammer nulling system for phased-array antennas", Applied Optics, vol 39(2), pp 212-230, Jan 10, 2000.

10. Paulo E. X. Silveira, G. S. Pati and Kelvin H. Wagner, Optical FIR Neural Networks, to be submitted to Applied Optics, October 2000.

11. Paulo E. X. Silveira, G. S. Pati and Kelvin H. Wagner, Experimental demonstration of an optoelectronic sonar adaptive array, to be submitted to Applied Optics, November 2000.

12. D. Z. Anderson and R.W. Brockett and N. Nuttall, Information dynamics of photorefractive two-beam coupling, Phys. Rev. Lett., 82 no. 7, 1418-21, 1999.

13. V. Damaio, E. Fotheringham, L. Czaia, V. Shkunov and D.Z. Anderson, Photorefractive Crystal Spheres and Disks, in preparation.

14. D.Z. Anderson, V. Damaio, D. Popović, Z. Popović, S. Romanish, and A. Sullivan, Optical Carrier Suppression by two-beam coupling in a photorefractive medium, in preparation.

15. D.Z. Anderson, V. Damaio, E. Fotheringham, D. Popović, Z. Popović, S. Romanish, and A. Sullivan, Optically Smart Active Antenna Array, in preparation.

16. D.Z. Anderson, V. Damaio, E. Fotheringham, "Photorefractive two-beam coupling modules", submitted to Applied Optics.

17. Arft, C.; Yankelevich; D. R., Knoesen, A.; Mao, E.; Harris, J. S.; "In-Line Fiber Evanescent Field Electro-optic Modulators," Journal of Nonlinear Optical Physics and Materials, Vol. 9, No. 1, 2000, p. 79-94.

18. Mao, E.; Yankelevich, D. R.; Lin, C.-C.; Solgaard, O.; Knoesen A.; Harris, J.S. Jr.; "Wavelength-selective semiconductor in-line fiber photodetectors," Electronics Letters, vol.36, No.6, IEE, 2000. p. 515-16.

19. Mao, E.; Yankelevich, D. R.; Lin, C.-C.; Solgaard, O.; Knoesen A.; Harris, J.S. Jr.; "Narrow-band light emission in semiconductor-fibre asymmetric waveguide coupler", Electronics Letters, vol.36, No.16, IEE, 2000, p. 1378-9.

2.5.2   Conference Presentations during 2000 (since 8/15/99)

1. Kelvin H. Wagner, Greg R. Kriehn, Andrew J. M. Kiruluta, and Paulo E. X. Silveira, "RF-Photonic adaptive-array processing", *Invited Paper* at SFO Horizons d'optique, Bordeaux, France, Sept 8 1999. [MURI]

2. K. H. Wagner, K. E. Anderson, K. D. Merkel, and W. R. Babbitt "Photon Echo Adaptive Array Processor" *Invited Paper* presented at 6th Int. Meeting of Hole Burning and Related Spectroscopies: Science and Applications (HBRS'99), September 18-23, 1999, Hourtin, France. [MURI]

3. K. Anderson and K. Wagner, "High bandwidth multiple channel communications using multimode fiber spatial spectral holographic dispersion compensation", paper TuH2, OSA annual meeting, Santa Clara Sept 28 1999. [DEPSCOR]

4. K. Wagner, A. Kiruluta, G. Kriehn, P. E.X. Silveira, S. Weaver, D. Dolfi, "Photorefractive-based true-time-delay beamforming using a traveling fringes detector", paper TuT3, OSA annual meeting, Santa Clara Sept 28 1999. [MURI]

5. Kelvin H. Wagner, Gregory Kriehn and Paulo E. X. Silveira, "RF-Photonic Adaptive array processing", Proc. of the National Radio Science Meeting (URSI), p 238, Boulder CO, January 2000. [MURI]

6. RF Photonic Systems for Array Control and Processing – An overview of the RF Photonic Systems for Antenna Arrays MURI, Kelvin H. Wagner, Zoya Popović, Dana Anderson, R.W. Babbitt, L. Griffiths, A. Knoesen, R. T. Weverka, *Invited Paper*, DARPA Photonic Systems for Antenna Applications Symposium, PSAA-10, February 2000.

7. Kelvin H. Wagner, Gregory Kriehn and Paulo E. X. Silveira, "Experimental demonstration of broadband adaptive beam forming using the BEAMTAP algorithm", DARPA Photonic Systems for Antenna Applications Symposium, PSAA-10, February 2000. [MURI]

8. Paulo E. X. Silveira, G. S. Pati and Kelvin H. Wagner, "Optical implementation of a single-layer finite impulse response neural network", Proc. Int. Conf. on Optics in Computing, SPIE vol. 4089, pp 656-667 Quebec City, June 2000. [MURI]

9. Gregory Kriehn, Paulo E. X. Silveira, G. S. Pati, Friso Schlottau and Kelvin H. Wagner, "BEAMTAP RF-photonic adaptive-array processing", Interactions between Microwaves and Optics summer school, Autrans France, August 2000. [MURI]

10. Gregory Kriehn, G. S. Pati, Paulo E. X. Silveira, Friso Schlottau, Kelvin H. Wagner, Daniel Dolfi and J. P. Huignard, "Demonstration of optical beam forming using BEAMTAP", *Invited Talk, IEE Microwave Photonics MWP-2000*, Oxford UK, September 2000. [MURI]

11. J. Vian, Z. Popović, "Optically-controlled T/R active lens array," *Invited presentation, 1999 URSI General Assembly Digest*, pp.674, Toronto, Canada, August 1999. [MURI]

12. P. Kirkpatrick, Z. Popović, "An X-band dielectric resonator electro-optic modulator," presented at the 2000 National URSI Meeting, Boulder, Colorado, January 2000. [MURI]

13. J. Vian, Z. Popović, "A Transmit/Receive Active Antenna with Fast Low-Power Optical Switching," 2000 IEEE MTT-S International Microwave Symposium, pp.847–850, Boston, June 2000. **(Awarded the 2nd prize in Best Student Paper Competition.)** [MURI]

14. D. Anderson, V. Damiao, E. Fotheringham, D. Popović, S. Romisch, Z. Popović, "Optically Smart Active Antennas," 2000 IEEE MTT-S International Microwave Symposium, pp.843–846, Boston, June 2000.

15. J. Vian, Z.Popović, "Optical Control of Microwave Circuits and Antennas," *Invited Talk, IEEE MWP Topical Meeting,* Oxford, UK, September 2000.

16. M. Tian, Z. Cole, K. D. Merkel, J. Zhao, and W. R. Babbitt "Accumulated Photon Echoes in a Tm3+:YAG Crystal by picosecond pulses," poster presentation at 6th Int. Meeting of Hole Burning and Related Spectroscopies: Science and Applications (HBRS'99), September 18-23, 1999, Hourtin, France. [MURI]

17. K. D. Merkel, K. Repasky, and W. R. Babbitt "Demonstration of a continuously programmed optical coherent transient processor," presented at 6th Int. Meeting of Hole Burning and Related Spectroscopies: Science and Applications (HBRS'99), September 18-23, 1999, Hourtin, France. [MURI/AFOSR/DEPSCOR]

18. K. D. Merkel, P. B. Sellin, R. D. Peters, K. S. Repasky and W. R.Babbitt, "Accumulated Complex Spectral Gratings using a Frequency Stabilized Laser," Workshop on Applications of Spectral Hole Burning 2000, Big Sky, Montana, July 9-12, 2000.

19. R. D. Peters, P. B. Sellin, K. S. Repasky, and W. R. Babbitt, " Frequency Stabilization of a Ti:Sapphire Laser to a Non-Persistent Spectral Hole in Tm:YAG," Workshop on Applications of Spectral Hole Burning 2000, Big Sky, Montana, July 9-12, 2000, poster.

20. R. Reibel, M. Tian, and W. R. Babbitt, " Optical Nutations on Three Pulse Accumulated Photon Echoes," Workshop on Applications of Spectral Hole Burning 2000, Big Sky, Montana, July 9-12, 2000, poster.

21. Z. Barber, R. Reibel, and W. R. Babbitt, "Applications of Binary Phase Shift Keying for Inhomogeneously Broadened Materials" Optical Science and Laser Technology Conference, Bozeman, Montana, August 14-16, 2000, poster.

22. K. Merkel, P. B Sellin, R. D. Peters, K. S. Repasky and W. R. Babbitt, "Accumulated Complex Spectral Gratings Using a Frequency Stabilized Laser," Optical Science and Laser Technology Conference, Bozeman, Montana, August 14-16, 2000.

23. M. Tian, R. Reibel, and W. R. Babbitt, "GHz Band True Time Delay and Auto-Correlation Via Accumulated Picosecond Photon Echo Process" Optical Science and Laser Technology Conference, Bozeman, Montana, August 14-16, 2000.

24. K. D. Merkel, Z. Cole, and W. R. Babbitt "Programmable variable time delay signal correlator based on six-wave mixing optical coherent transients," poster presentation at 6th Int. Meeting of Hole Burning and Related Spectroscopies: Science and Applications (HBRS'99), Sept. 18-23, 1999, Hourtin, France. [DEPSCOR]

25. K. D. Merkel, Z. Cole, and W. R. Babbitt, "Signal correlator with programmable variable time delay based on optical coherent transients," IEEE Lasers and Electro-Optics Society 1999 Annual Meeting, Nov. 8-11, 1999, San Francisco, CA. [DEPSCOR]

26. R. L. Cone, Y. Sun, F. Knz, N. M. Strickland, T. L. Harris, C.W. Thiel, T. Bttger, G. Reinemer, W. R. Babbitt, R. W. Equall and R. L. Hutcheson, R. M. Macfarlane, and J. A. Ritcey, "New Rare Earth Materials, Material Concepts, and Demonstrations of Spectral Hole Burning Applications," presented at 6th Int. Meeting of Hole Burning and Related Spectroscopies: Science and Applications (HBRS'99), September 18-23, 1999, Hourtin, France. [AFOSR]

27. A. Rebane, A. Tchouassi-Djiki, and W. R. Babbitt, "Ultrafast frequency-conversion holograms by photo-induced gratings in glass," IEEE Lasers and Electro-Optics Society 1999 Annual Meeting, Nov. 8-11, 1999, San Francisco, CA. [NSF MONTS]

28. C. Sajaarda Cornish, L. Tsang, W.R. Babbitt. "Demonstration of highly efficient photon echoes in absorbing media," in Conference on Lasers and Electro-Optics, Technical Digest (Optical Society of America, Washington DC, 2000), pp. 216-217, May 2000, San Francisco, CA.

29. C. Sajaarda Cornish, L Tsang, and W.R. Babbitt, "A study of the energy source for photon echoes" in Conference on Lasers and Electro-Optics, Technical Digest (Optical Society of America, Washington DC, 2000), p. 491, May 2000, San Francisco, CA.

30. Z. Cole, K. Merkel, and W.R. Babbitt, "Atomic coherence state phase conjugation in optical coherent transients," in Conference on Lasers and Electro-Optics, Technical Digest (Optical Society of America, Washington DC, 2000), pp.68-69, May 2000, San Francisco, CA.

31. C. Sjaarda Cornish, W. R. Babbitt, and L. Tsang, "Experimental Demonstration of Highly Efficient Photon Echoes in an Absorbing Medium." Workshop on Applications of Spectral Hole Burning 2000, Big Sky, Montana, July 9-12, 2000.

32. D.Z. Anderson, V. Damaio, E. Fotheringham, D. Popović, Z. Popović, S. Romanish, and A. Sullivan, "Optically Smart Active Antenna Array", MTT, Boston MA, June, 2000.

2.5.3   Patents and Applications

1. K. D. Merkel and W. R. Babbitt, "Variable Time Delay Optical Coherent Transient Signal Processing," Provisional Patent Filed September 15, 1999. [DEPSCOR]

2. "In-Line Polymeric Construct for Modulators, Filters, Switches and Other Electro-Optic Devices," U.S. Patent No. 6,047,095, Awarded to: Knoesen, A.; Yankelevich, D. R.; Hamilton, S. A.; Abbot, N. L., Hill, R. A. and Bjorklund, G. C., April 4, 2000.

2.6   Classes taught by PIs relating to MURI research

Prof. Popović's new book "Introductory Electromagnetics" was published this year and has already been used at CU and adopted by several other Universities.

Dr. Wagner and Dr. Anderson jointly taught a highly revised graduate-level Advanced Optics Lab in Fall of 1999 developed for interdisciplinary students with interests in Physics and Electrical Engineering. Several of the MURI graduate students were involved either as TAs or in taking the class.

Last year Prof. Popović taught a new special topics graduate course *RF/optical techniques,* that covered some common methods and components used at both RF and optical frequencies (wavelengths). The objective of the course was to present two different views of the same electromagnetic technique, phenomenon, or circuit component. Examples of methods that were compared include: Fourier optics and antenna analysis, Gaussian beams at optical and millimeter waves, diffraction theory, and basic field theorems. Examples of components that are compared include: polarizers, lenses, waveguides, directional couplers, retroreflectors, phase conjugators, and soliton transmission structures. The course concluded with a conference where students presented projects they worked on during the last month of the course. The presentations were judged by industry members, and Best Paper Award was given. A digest of this mini conference was published for assessment purposes (available upon request).

1. Wagner, CU ECEN 5696, Fourier Optics, Fall 2000, graduate.

2. Wagner, CU ECEN 6006, Nonlinear Optics, Spring 2000, graduate.

3. Wagner, CU ECEN 5156, Physical Optics, Fall 1999, graduate.

4. Wagner and Anderson, CU ECEN 5606, Fall 1999, graduate.

5. Anderson, CU PHYS 4510, Fall 1999, undergraduate.

6. Popović, CU ECEN 5004, RF/optical techniques, Spring 1999, graduate.

7. Popović, CU ECEN , Transmission/Antenna Lab, Fall 1999, graduate.

8. Babbitt, MSU Physics 500-14, Optical Coherent Transient Seminar Spring 2000, graduate.

9. Babbitt, MSU Physics 500-14, Optical Coherent Transient Seminar Fall 1999, graduate.

10. Babbitt, MSU Physics 353, Holography-Laser Photography, Spring 2000, undergraduate.

11. Knoesen, UC Davis EEC236, Nonlinear Optical Applications, Fall 1999, graduate.

3   Photorefractive Adaptive Array Processing

Principal Investigator: Kelvin Wagner, University of Colorado, Dept of ECE

A detailed analysis of an imaging BEAMTAP system using a closed loop configuration enabling both broadband beam forming and jammer nulling has been published in Applied Optics,[1] with BEAMTAP simulations similar to those described in Sec. 5 presented on the front cover of the issue. In addition, experimental results showing the open-loop capabilities of the BEAMTAP system have already been presented, demonstrating broadband beam forming on simulated signals from a phased-array.[2-4] The system uses an acousto-optic deflector (AOD) to perform the RF to optical time-delay line (TDL) for programming the beam-steering look angle, a photorefractive crystal to adaptively store and adjust the integrated weights, and a scrolling output photodetector implemented with a traveling-fringes detector (TFD) used in a novel hole-resonant transport mode of operation to allow for the squint-free processing of RF array signals from an array as large as 20 meters in diameter. Finally, read-write isolation has been demonstrated using polarization multiplexing of the simulated signals from the antenna array, which allows for closed-loop adaptation to be performed.

Figure 1 schematically illustrates the optical architecture of the BEAMTAP system. A single coherent laser is divided with two beam splitters with amplitude reflectances a_r and a'_r, and amplitude transmittances a_t and a'_t, respectively, to drive both the fiber-feed network and the BEAMTAP processor. The fiber-feed network from the phased array is shown on the left-hand side. An incident RF wavefront is detected by each antenna element in the antenna array and the detected signals are used as the input signals to a bank of electro-optic modulators (EOMs), whereby the modulated light from the EOMs is fiber remoted to the optical processor. The diffracted light from the AOD interferes with signals from the array, which are imaged through lens system L_0 to form gratings in the photorefractive (PR) crystal. Diffraction of the phased-array signals off this grating is detected by a synchronous TFD, which has a carrier velocity matched to the magnified acoustic velocity of the AOD by the lens systems L_1 and L_2—producing a resonant charge carrier distribution $q(x_2, t)$. The output signal $o(t)$ is amplified by g_1, passed through a band-pass filter (BPF), subtracted from the desired signal $d(t)$, amplified by g_2, and fed back into the AOD as the feedback signal $f(t)$ to close the adaptive feedback loop necessary for the system to cancel any jamming signals present in the signal environment. A Rochon prism, linear polarizer (LP), and spatial filter (SF) are used for the read–write isolation of the AOD beam from the diffracted phased-array signals off the grating. The illustrated system places the photorefractive crystal in the image plane of the fiber feed and the AOD, and uses orthogonally propagating fields, for illustrative purposes.

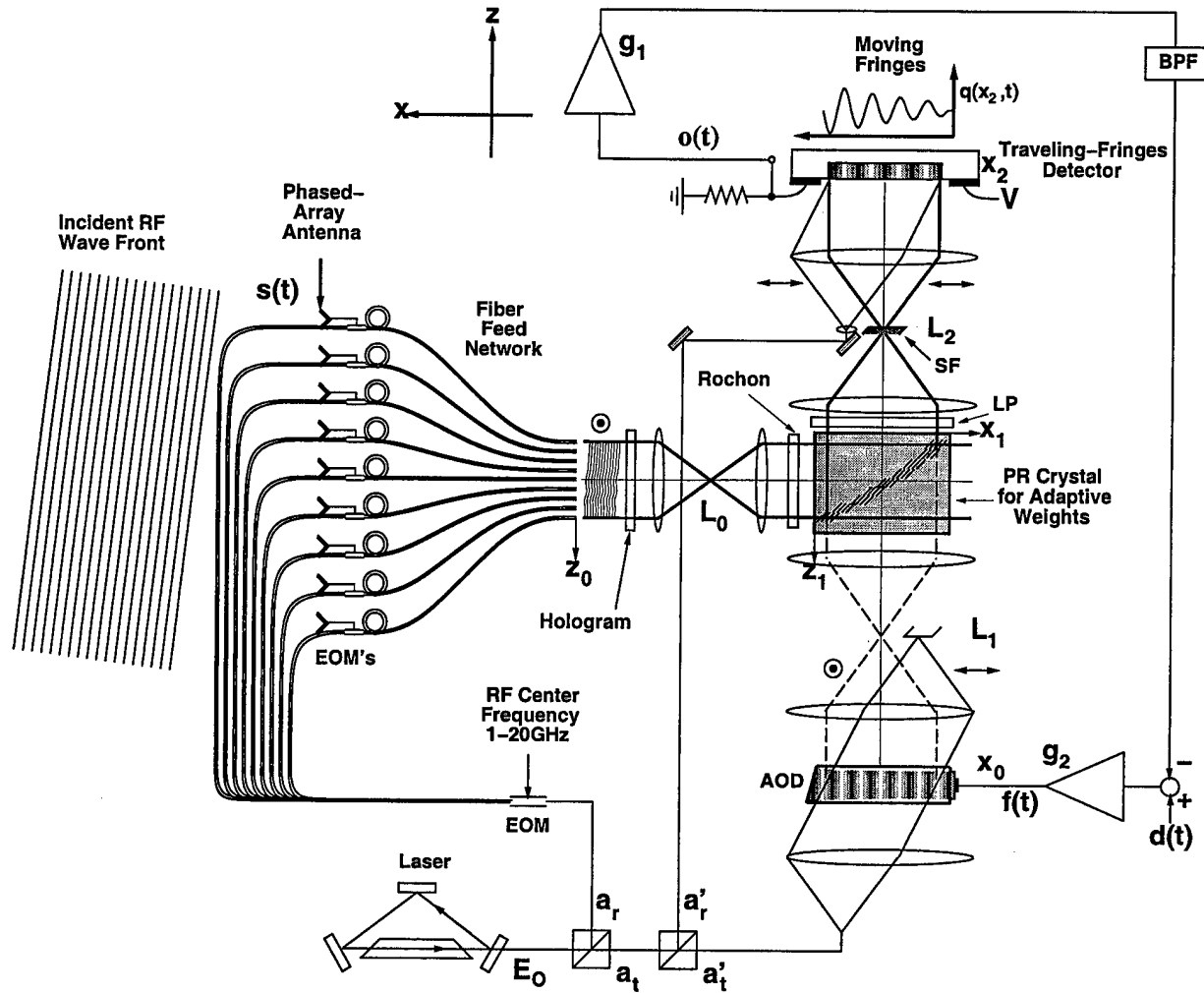The final output signal is given by

Figure 1: Optical BEAMTAP architecture showing the antenna element signals applied to electro-optic modulators (EOMS) whose coherently modulated output propagate through the fiber array feed mainfold on the left into the processor. The traveling wave acousto-optic device (AOD) is imaged through the photorefractive (PR) crystal onto the synchronously propagating traveling fringes detector, and the interference is time-integrated in the PR to act as the adaptive weights.

$$\tilde{o}(t) = R\,\kappa_2 \int\limits_{-T_D/2}^{T_D/2} \sum_{n=1}^{N} \tilde{s}_n(t - t_n + \tau_x - t_{r_2}) \times$$

$$\int\limits_{-\infty}^{t-T} g_2\left[\tilde{d}(t_2 + (T - t_d)) - g_1\tilde{o}(t_2)\right]\tilde{s}_n^*(t_2 - t_n + \tau_x - t_{r_2})\,dt_1\,d\tau_x, \quad (1)$$

which shows that a cross-correlation is formed between fixed delayed versions of the signal from the antenna array and a delayed version of the feedback signal, which is then convolved with the instantaneous signals from the array to provide the final output $\tilde{o}(t)$. The behavior of this equation can best be visualized by transforming to the spatio-temporal frequency domain and

algebraically manipulating the spectra to solve for $\tilde{O}(f)$. At steady-state with $t \gg T$, where T is the round trip delay present in the system, the output signal is a spatio-temporal convolution of the signal from the phased array with the cross-correlation function of the delayed feedback signal with the delayed version of the phased array signal. When transformed to the spatio-temporal Fourier domain Eq. 1 becomes

$$\tilde{O}(f) = \sum_{k_l} \tilde{S}(k_l, f) \frac{\frac{g}{g_1} \alpha \left| \tilde{D}(f) \right|^2 e^{i2\pi f(T - t_d)} \delta \left(k_l - \frac{f}{c} \sin\theta_r \right) * b(k_l, f)}{1 + g \sum_{k_l} \sum_j \left| \tilde{J}_j(f) \right|^2 \delta \left(k_l - \frac{f}{c} \sin\theta_j \right) * b(k_l, f)}, \tag{2}$$

where $b(k_l, f) = T_d \operatorname{sinc}(T_d f) N d \operatorname{sinc}(N d k_l)$ denotes the spatio-temporal blur function. The linear adaptive array output frequency response is given by a weighted signal spatio-temporal frequency spectrum which is summed across all spatial frequencies

$$\tilde{O}(f) = \sum_{k_l} \tilde{S}(k_l, f) \tilde{T}(k_l, f). \tag{3}$$

This allows the steady-state spatio-temporal transfer function of the BEAMTAP processor to be defined as

$$\tilde{T}(k_l, f) = \frac{\frac{g}{g_1} \alpha \left| \tilde{D}(f) \right|^2 e^{i2\pi f(T - t_d)} \delta \left(k_l - \frac{f}{c} \sin\theta_r \right) * b(k_l, f)}{1 + g \sum_{k_l} \sum_j \left| \tilde{J}_j(f) \right|^2 \delta \left(k_l - \frac{f}{c} \sin\theta_j \right) * b(k_l, f)}. \tag{4}$$

The maximum array sensitivity is along the tilted locus in spatio-temporal frequency space corresponding to the desired signal AOA, with a bandwidth tuned to the power spectrum of the steering signal $|D(f)|^2$ (actually flattened by the LMS dynamics). This output achieves the full array gain of N, as the beam-forming operation has a linear phase that time delays the arriving signal to time align it with the known reference signal. Jammer nulling is accomplished by an inverse filter (the denominator) that acts as a power nuller to any jamming signals present in the signal environment at their respective angles of arrival [denoted by the $\delta \left(k_l - f/c \sin\theta_j \right)$ term] and frequency spectrums.

Beam steering is driven by the known component $\alpha \tilde{d}(t)$ of the desired signal detected at the array $r(t) = \alpha \tilde{d}(t) + \alpha' \tilde{d}'(t)$, which can be either time or code multiplexed with the spectrally overlapping unknown desired signal $\alpha' \tilde{d}'(t)$, as described in Sec 5.2. The TFD output contains both $\tilde{d}(t)$ and $\tilde{d}'(t)$ weighted proportionally to α and α', respectively, since they are broadcast by a single transmitter and arrive on the array with identical phase fronts. At steady state the amplitude of the known component at the differencing node adaptively adjusts to a nearly exact match of the known reference signal; thus just after the differencing node, the known component is cancelled, and the unknown desired signal $\alpha' \tilde{D}'(f)$ remains detected with the full array gain and all of the jammers optimally extinguished.
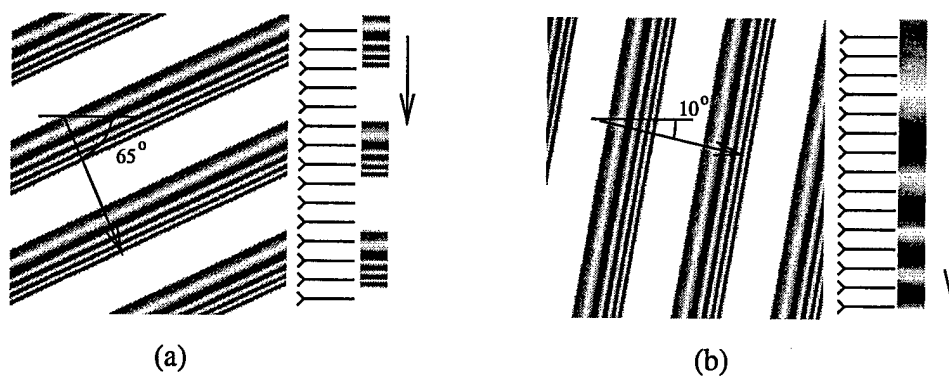
(a) (b)

Figure 2: Time-slices for different angles of arrival.

3.1 Antenna-Array Emulator

In order to test the BEAMTAP processor, a phased array of antennas had to be emulated, since antenna arrays with thousands of elements, each with a fiber optic feed, are not currently available in our lab. Thus we designed an emulator to essentially act as an optical beam steering unit for a phased-array antenna. Signals to be transmitted are generated using an acousto-optic deflector (AOD), and the signals are steered to different angles using an adjustable anamorphic prism pair. The time delay is generated by acoustic propagation in the AOD, which serves to simulate the time delay present between different antenna elements for a given angle of arrival (AOA). Anamorphic magnification of the prism pair allowed us to scale the time delay, which results in variable angles of reception.

3.1.1 Emulator concept

Signals impinging on an antenna array at different angles result in temporal signal slices which are magnified versions of each other. For larger angles of incidence (measured with respect to the normal of a linear antenna array), an arbitrary point on the wavefront has a longer transit time across the array than the same point of a wave impinging the array at a smaller AOA. This effect is shown in Fig. 2 (a) and (b) respectively. This figure shows that the instantaneous time slice for varying angles of incidence at the array are simply magnified versions of the time-slice which is obtained in the end-fire position. One way to create these variably-magnified slices of data without an actual antenna array involves the use of an AOD. As the acoustic waves carrying the RF information propagate through the crystal, they spatially and temporally modulate the light which is being deflected. This is analogous to the RF signal scrolling across the array and modulating light in fibers connected to each individual antenna element with an electro-optic modulator (EOM). In a physical antenna array, the magnification of the time-slice occurs through the signal source arriving at a different AOA. In the simulator, a change in incidence angle could be caused by changing the speed of the acoustic wave, but since this is impractical, magnifying the transverse profile of the existing time-slice is chosen as an alternative. This magnification can
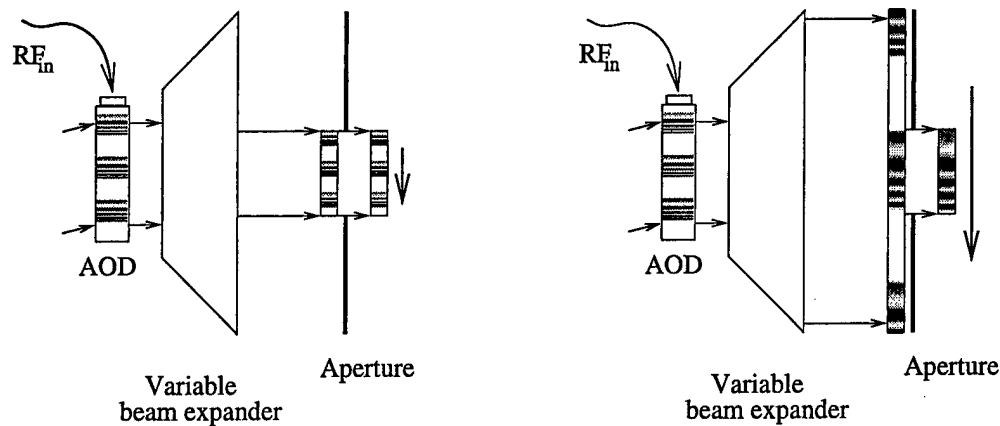
Figure 3: Use of an AOD to generate spatio-temporally varying signals which are analogous to those generated by an antenna array.
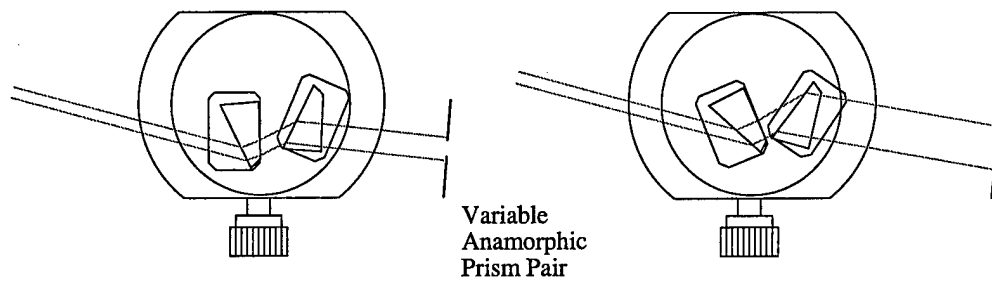

Figure 4: Anamorphic prism pair at two different magnifications. When the light from the AOD is passed through these, the apparent angle of arrival for the two shown cases is different.
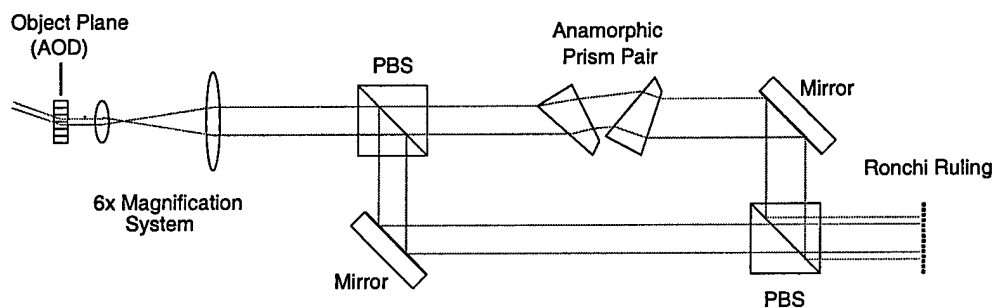

Figure 5: Simulator configuration used to probe angular sensitivity pattern of BEAMTAP processor.

be performed with an anamorphic prism pair. The process is shown in Fig. 3. By changing the magnification of the variable beam expander, different AOAs can be simulated. In the simulator we have designed, the variable beam expansion is performed by an adjustable anamorphic prism pair, as shown in Fig. 4.

The initial purpose of the emulator is to probe the angular receptivity pattern of the adapted BEAMTAP processor. For this, a grating is written in the photorefractive crystal with one

polarization, and an orthogonally polarized, anamorphicly-magnified version of the same beam is used to probe the grating. The two orthogonally–polarized beams will both carry information from the same AOD. This process is illustrated in Fig. 5, and requires the two beams to be exactly co-propagating since the grating in the photorefractive crystal is extremely Bragg selective. An angular deviation would result in a Bragg-mismatched readout, thereby falsifying the actual angular sensitivity pattern.

3.1.2 First experiments

After assembling a system like the one shown in Fig. 5, it was determined that the anamorphic prism pair adjuster (PPA) angularly deviated the beam in the horizontal direction when different magnifications were accessed. Since this is unacceptable due to the Bragg selectivity of the photorefractive crystal, the PPA was mounted on a rotation stage and a set of electomechanical actuators were used to change the magnification and the PPA's rotation angle. This allowed for compensation of the angular deviation created by different magnification settings. This setup worked well initially, since expanded beams were being used. However, once the beams were focused into the photorefractive crystal, it was determined that the angular deviation is also accompanied by a lateral shift. This shift also generated an erroneous readout of the adaptive weights within the photorefractive crystal, so another degree of freedom (DoF) to provide lateral correction must be added. Currently, a third electromechanical actuator is being considered, or using a self correcting geometry which involves two passes of the light through the prism pair.

3.2 Traveling-Fringes Detector

The traveling-fringes detector (TFD) used in BEAMTAP processor is a photo-conducting layer of GaAs that uses a resonantly enhanced amplitude of the photocarrier grating for broadband detection of optically modulated high frequency RF signals. Dolfi at Thomson originally developed this device due to its large conversion efficiency at high (microwave) frequencies and a high optical saturation level owing to its large detection volume. We are collaborating with Dolfi to utilize, in addition to its broadband detection, the physical time delay associated with TFD operation which makes it suitable for true-time-delay processing in the optical BEAMTAP system. In this section, we report the enhanced time-delay capability of the device as a tap-delay line, using a novel resonant hole transport process.

3.2.1 Principles of broadband detection and resonant hole transport

The TFD device provided by Dolfi at Thomson was grown using molecular beam epitaxy (MBE) on a semi-insulating GaAs substrate. Figure 6a shows the physical dimensions of the device and its layered cross-section showing an active 5 μm thick layer of photo-conducting
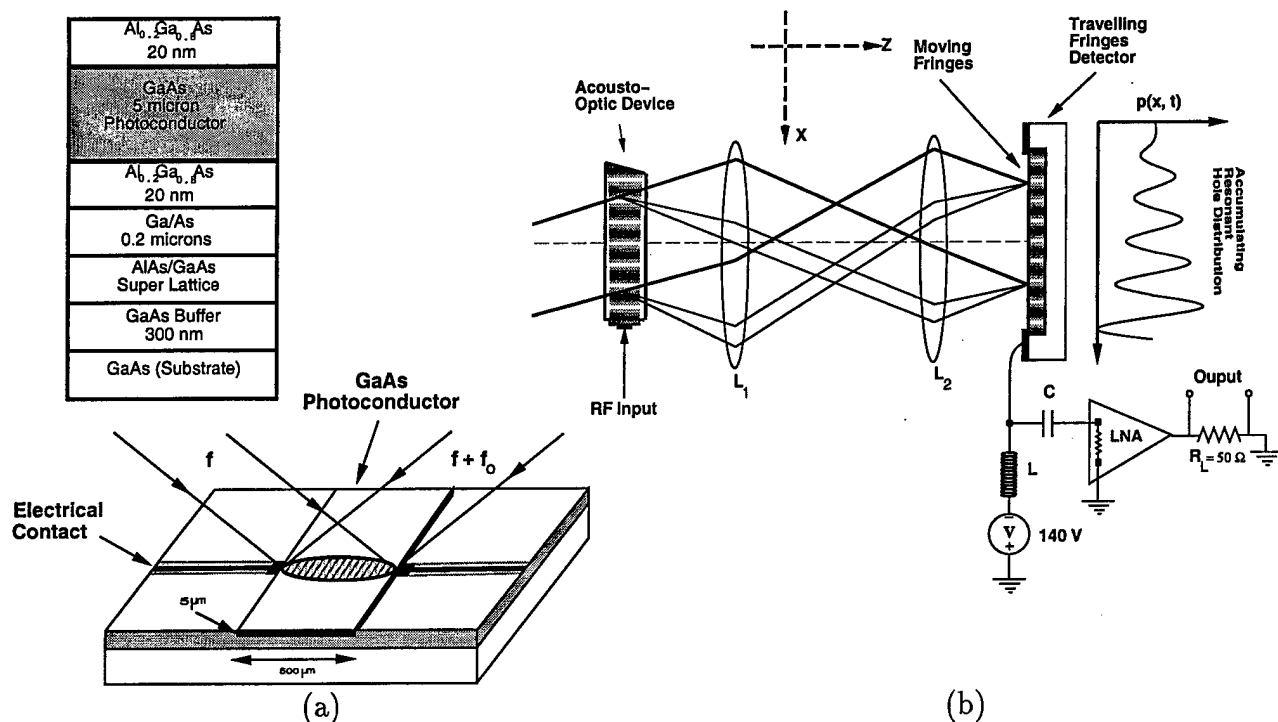
Figure 6: (a) Multi-layered structure of the Thomson TFD device. The structure of the device is used with interferometric traveling fringes produced by interference of the frequency shifted beams. (b) Experimental setup used to verify broadband detection of an RF signal using the resonant hole transport process. A $4f$-imaging system with unit magnification was used.

GaAs. This layer is sandwiched between two 20 nm thick transparent layers of AlGaAs to minimize surface recombination and extend the intrinsic photocarrier lifetime from a few to tens of nanoseconds, which is required for the BEAMTAP array processing application.

Resonantly enhanced amplitude detection in the TFD relies on a synchronous drift of generated photocarriers with a moving interference pattern formed by the superposition of frequency shifted coherent laser beams. When a DC electric field E is applied across the device, photogenerated carriers drift under the influence of the field velocty. The resonance condition is established when the interference moving fringe pattern velocity $v_{gr} = \frac{\lambda}{2sin(\frac{\theta}{2})}$, where θ is the angle between the frequency-shifted interfering beams, is matched to the drift velocity $v_d = \mu E$, where μ is the carrier mobility of the photogenerated carriers. Since the charge carriers synchronously travel with the interference pattern in the entire detection volume, the delivered microwave power is increased either by taking advantage of the photoconductive gain $G = \frac{\tau}{\tau_t}$, where τ is the carrier lifetime and τ_t is the transit time of the photogenerated carriers across the interelectrode distance, or by using a high optical saturation level. In Dolfi's original scheme the interfering beam angle θ was fixed, which limited the bandwidth—although center frequencies up to 15 GHz were demonstrated.

For broadband detection of an RF signal, the angle θ must be changed with frequency. This is accomplished using an AOD in conjunction with the TFD, as shown in Fig. 6b. We previously
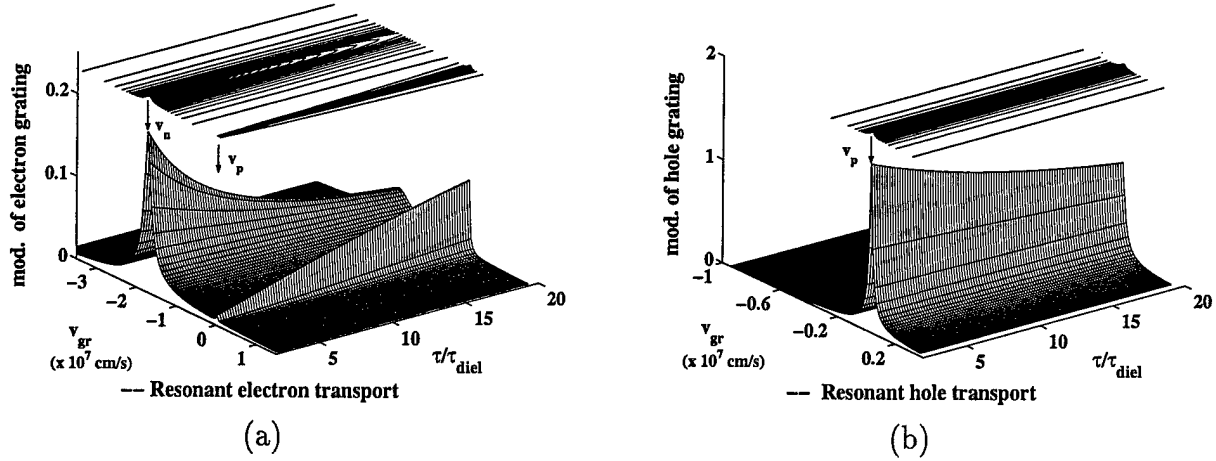
Figure 7: Resonance in modulation of the photocarrier (a) electron and (b) hole gratings, showing the influence of space-charge resulting from ambipolar diffusion in the lifetime limited regime ($\tau/\tau_{diel} \gg 1$).

demonstrated this mode of operation using resonant electron transport in the device. An optical $4f$-imaging system is used to form a moving interference pattern between the undiffracted beam and the frequency-shifted diffracted beams produced by the AOD. The frequency and angle preserving nature of diffraction from AOD ensures that the interference patterns resulting from various diffracted components of a broadband signal move at the same velocity irrespective of their frequency. At resonance, the magnitude of the applied DC field can be suitably chosen such that $v_{gr} = v_d$ equals the acoustic velocity v times a magnification factor M associated with the imaging system, i.e $v_{gr} = v_a M$.

The finite transit time $\tau_t = \frac{l}{v_d}$ of the photocarriers across the interelectrode distance l (500 μm) of the TFD gives rise to time-delay in signal detection. This is a useful feature, as it enables the device to be used as a tap-delay-line (TDL) in the optical BEAMTAP processor. For true-time-delay processing applications, last year's report demonstrated a nearly uniform broadband response over the bandwidth of interest (750 MHz - 1250 MHz) and the time-delay capabilities (5 ns) of the device using electron transport. Since the mobility of photogenerated holes μ_p (≈ 200 cm^2/Vs) in GaAs is significantly lower than the electron mobility μ_n (≈ 8500 cm^2/Vs), it was anticipated that the magnitude of the achievable time-delay could be increased by approximately 40 times if resonant hole transport could be exploited instead. This would dramatically increase the usefulness of the device for true-time-delay processing applications.

In order to model and gain insight into the process of resonant transport of photocarriers in the photoconductor, rate equations for electron and hole density modulations were used and solved under the weak intensity modulation approximation:

$$\frac{\partial \delta N}{\partial t} = \eta I_o(x,t) - \delta N\left(\frac{1}{2\tau} + \frac{1}{2\tau_{diel}^n}\right) - \delta P\left(\frac{1}{2\tau} - \frac{1}{2\tau_{diel}^n}\right) + D_n\frac{\partial^2 \delta N}{\partial x^2} - v_d^n\frac{\partial \delta N}{\partial x} \qquad (5)$$

$$\frac{\partial \delta P}{\partial t} = \eta I_o(x,t) - \delta P \left(\frac{1}{2\tau} + \frac{1}{2\tau_{diel}^p} \right) - \delta N \left(\frac{1}{2\tau} - \frac{1}{2\tau_{diel}^p} \right) + D_p \frac{\partial^2 \delta P}{\partial x^2} - v_d^p \frac{\partial \delta P}{\partial x}, \tag{6}$$

where $I_o(x,t)$ is the spatio-temporal moving interference pattern, δN and δP are photocarrier modulations, D_n and D_p are diffusion constants, τ_{diel}^n and τ_{diel}^p are dielectric relaxation time constants, and v_d^n and v_d^p are drift velocities—each for electrons and holes, respectively. Equations 5 and 6 were solved simultaneously to obtain the magnitude of the photocarrier gratings. Solutions for the modulation amplitude of electrons and holes are plotted in Fig. 7 using the appropriate transport parameters for GaAs. Besides the predicted resonances in photocarrier modulations, the results show the effect of the internal space-charge field resulting from ambipolar diffusion on the magnitude of photocarrier gratings in the life-time limited regime (i.e., carrier lifetime τ is large compared to the dielectric relaxation time τ_{diel}). As shown in the figure, characteristic resonance ($v_{gr} = v_p$) observed in resonant hole transport has a higher magnitude and is sharply defined over fringe velocity compared to that observed in resonant electron transport. Screening of resonantly drifting holes by electrons due to dielectric relaxation also produces an electron (complementary-hole) resonance in electron modulation that may significantly reduce the sensitivity at hole resonance when τ is comparable τ_{diel}. These results suggest that material characteristics of the device can be suitably tailored to extend the photocarrier lifetime and/or lower the diffusion response in order to use the specific resonant transport desired for the device application. Lifetimes of several tens of nanoseconds may be obtained at low intensity, but because recombination in GaAs increases with carrier density, the lifetime will decrease at higher optical powers.

3.2.2 Hole Resonant Transport Experimental Results

In our experiments, resonant hole transport has been demonstrated by reversing the applied DC voltage across the device. The magnitude of the applied field was reduced to 2.8 kV/cm due to the decrease in hole mobility and the low saturation velocity when compared to electrons. The magnification associated with the optical imaging system shown in Fig. 6b was accordingly adjusted to meet the resonance condition for hole transport. A $4f$ imaging system using unit magnification formed an image of the illuminated AOD aperture (225 x 75 μm) onto the active area of TFD. During detection, the optical power in the undiffracted beam was maintained close to 15 mW and the diffraction efficiency of the AOD was measured to be approximately 8 % over the bandwidth of interest.

To verify signal detection using resonant hole transport detection, a single frequency signal at 1 GHz was applied to the AOD. The output from the TFD was fed to a wideband bias-tee that filtered out the DC bias voltage from the RF signal generated by the TFD before amplification using successive stages of low noise RF amplifiers, as shown in Fig. 6b. The detected signal power was found to be 20 dB lower than the value reported earlier for resonant electron transport, and
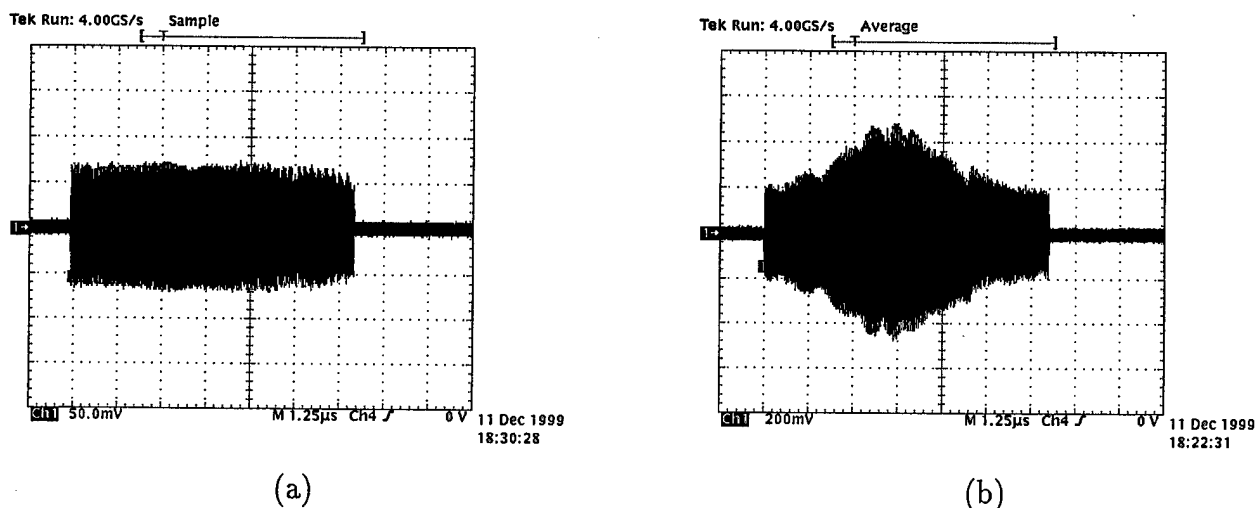
(a)   (b)

Figure 8: (a) 8 μs 250 MHz bandwidth pulse-compressed chirp input into the AOD. (b) The detected output after amplification shows the reconstruction of the chirp signal using the detector in a novel hole-resonant transport mode of operation.

can be ascribed to the inefficiency of device properties and electrical contacts to support hole transport detection in the material.

Resonant response of the TFD to an 8 μs double sideband 250 MHz chirp centered at a 1 GHz carrier frequency is shown in Fig. 8, with the detected signal being faithfully reproduced with a small amount of ringing present in the output. The small 2-3 dB ripple in response was observed over the entire bandwidth of interest. However, a substantial drop in response was observed at high frequencies ($\geq$ 1.1 GHz). Such an effect can be attributed to a reduction in the saturation velocity of photogenerated carriers due to low hole mobility. The response at high frequencies experienced this drop since the lower saturation velocity optimizes the transit time but reduces the sensitivity of the device. The effect is further believed to be compounded by non-optimal impedance matching at the TFD output.

Increased time-delay capabilities of the device with resonant hole transport have been verified using the 8 μs chirped pulse with 250 MHz of bandwidth. Linear time-delay across the TFD was achieved by translating the device and correlating the detected signal with the reference signal without any translation. To predict the maximum achievable time delay, the device was translated by 250 μm and the response was correlated with the reference signal. After capturing the waveform using a high bandwidth digital oscilloscope, digital filtering was performed to remove the undesirable harmonics from the signal spectrum. The signal was then down converted to baseband. Figure 9 shows a time-delay of 60 ns associated with the translation of 250 μm. This illustrates an increase in achievable time-delay approximately by a factor of 20 when using the resonant hole transport process instead of an electron one. This also suggests the appropriateness of the device to be used as the input TDL in the BEAMTAP processor.

250 MHz Chirp Correlation

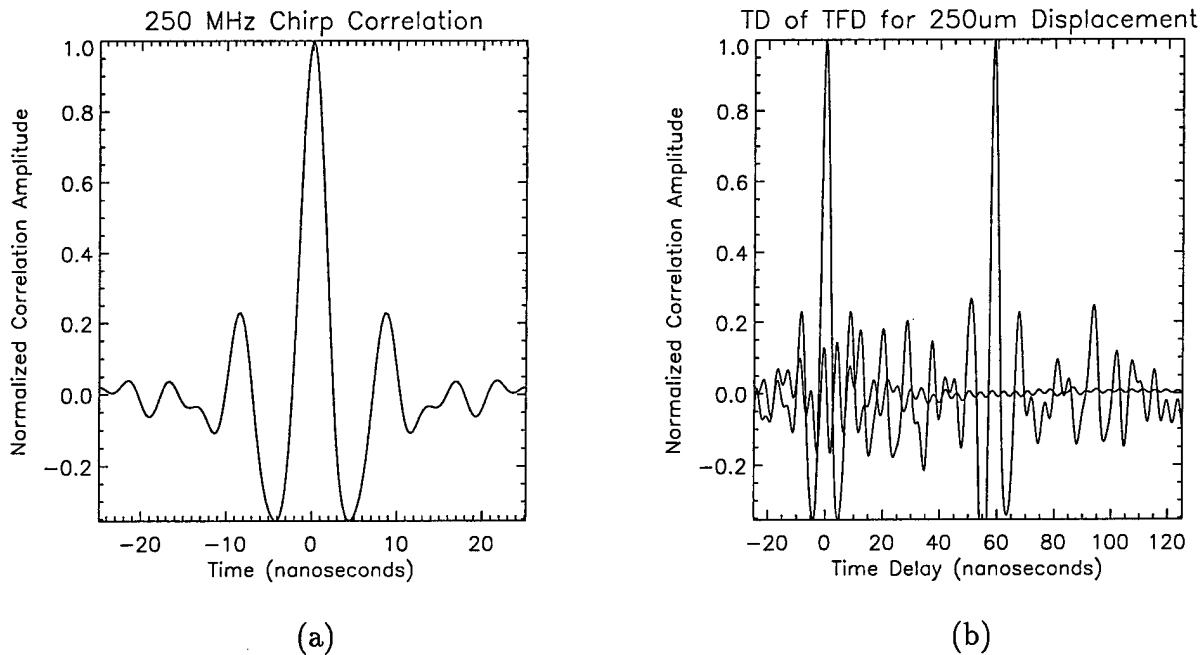TD of TFD for 250um Displacement

(a)

(b)

Figure 9: (a) Digital filtering and performing an auto-correlation of the output allows for the generation of nanosecond pulses. Shown here is the auto-correlation of a 250 MHz bandwidth chirp, generating a 4 ns pulse. (b) After translating the detector 250 μm, the detected output is cross-correlated against the original detected output, showing a shift in the correlation peak with 60 ns of time delay with respect to the original auto-correlation of the detected waveform. This time delay allows the detector to be used as a scrolling tap-in delay line for the optical implementation of the BEAMTAP algorithm.

3.2.3 Future Considerations

A TFD device designed with a suitable ohmic (metal-semiconductor) contacts could replenish holes at the input electrode that have drifted across the photoconductive layer. Such a device would compensate for low hole mobility, high probability of recombination, and improve the device sensitivity. For practical purposes, a metallic layer with a suitable dopant species—donor or acceptor atoms—could be used to grow the ohmic contacts. The contact can usually considered to be acceptable if it can supply the required current density with a voltage drop that is small compared to the drop across the active region of the device. For resonant hole transport, a p-type contact for GaAs such as Au/Zn/Au with Zn acceptors could be chosen.

The sensitivity and signal-to-noise ratio (SNR) of the device at high frequencies could be increased by a couple orders of magnitude using an impedance matching network at the output of the device. This would reduce the reflections or return losses resulting from parasitic and lumped electrical elements across the TFD. We are recently exploring the interfacing of an AC-coupled wideband transimpedance amplifier with the device. A simple circuit analysis is being used to emulate the TFD's signal current with source a resistance and capacitance to design the interface circuit for the transimpedance amplifier. The moving interference pattern and dynamic

photoconductive nature of the device however, poses a problem in measuring its true electrical characteristics. An improved impedance matched interface circuit will be designed taking into account various considerations such as transimpedance gain, frequency bandwidth, input drive voltages, and saturation characteristics.

By suitably engineering a quantum well structure using alternate n- and p-type GaAs layers, electron and hole transport could be firmly confined and permitted to different layers in the growth direction, respectively. In the final phase, we will investigate the possibility of such a quantum well structure in the device in order to extend the carrier life-time as required.

3.3 Read-Write Polarization Multiplexing

Having developed an emulator for the antenna array and by using the TFD in a hole-resonant transport process, an open-loop version of the experimental implementation of the optical BEAM-TAP processor described in Sec. 3 has been demonstrated. In addition, a polarization read-write multiplexing technique has been used for read-write isolation. Figure 10 shows the experimental implementation of the read-write polarization multiplexing technique used to isolate the writing beams from that of the reading beam within the photorefractive crystal. The vertically polarized light from a Coherent 5W Verdi laser was initially passed through a half-wave plate and Glan laser prism to act as a variable attenuator before being spatially filtered and collimated by a 50 mm focal length lens. The beam was then split into two separate beams via an additional wave plate and polarizing beam splitter. One beam was fed into the simulator arm of the processor, and the other beam was input into the feedback arm. Light which entered the simulator arm of the processor was focused into an AOD, which served to act as the simulated array of signals from an antenna array as described in Sec. 3.1. The first diffracted order was allowed to pass though an iris while the DC beam was blocked, with the diffracted light off the acoustic grating then being imaged into two separate anamorphic prism pairs acting as variable beam expanders. The light which entered each of the two prism pairs were orthogonally polarized such that the $\hat{o}$-polarized and $\hat{e}$-polarized beams served as the reading and writing beams, respectively, within the photorefractive crystal. Adjusting the prism pair angle served to magnify the image of the AOD, and simulated a change in the AOA of a signal impinging upon an antenna array. Each of the two beams were adjusted separately, which enabled the simulation of arbitrary AOAs for both the writing and reading beams, respectively. The two beams were then passed though polarizers to purify their states of polarization before being recombined with a polarizing beam splitter, having accounted for any lateral and angular deviations in the beams with the electromechanical actuators attached to the prism pair mount. This combined read-write beam was then fed into an SBN photorefractive crystal.

Light in the feedback arm was first compressed in the lateral direction so that when focused into the second AOD, the beam was 75 μm tall (which was the height of the transducer) and
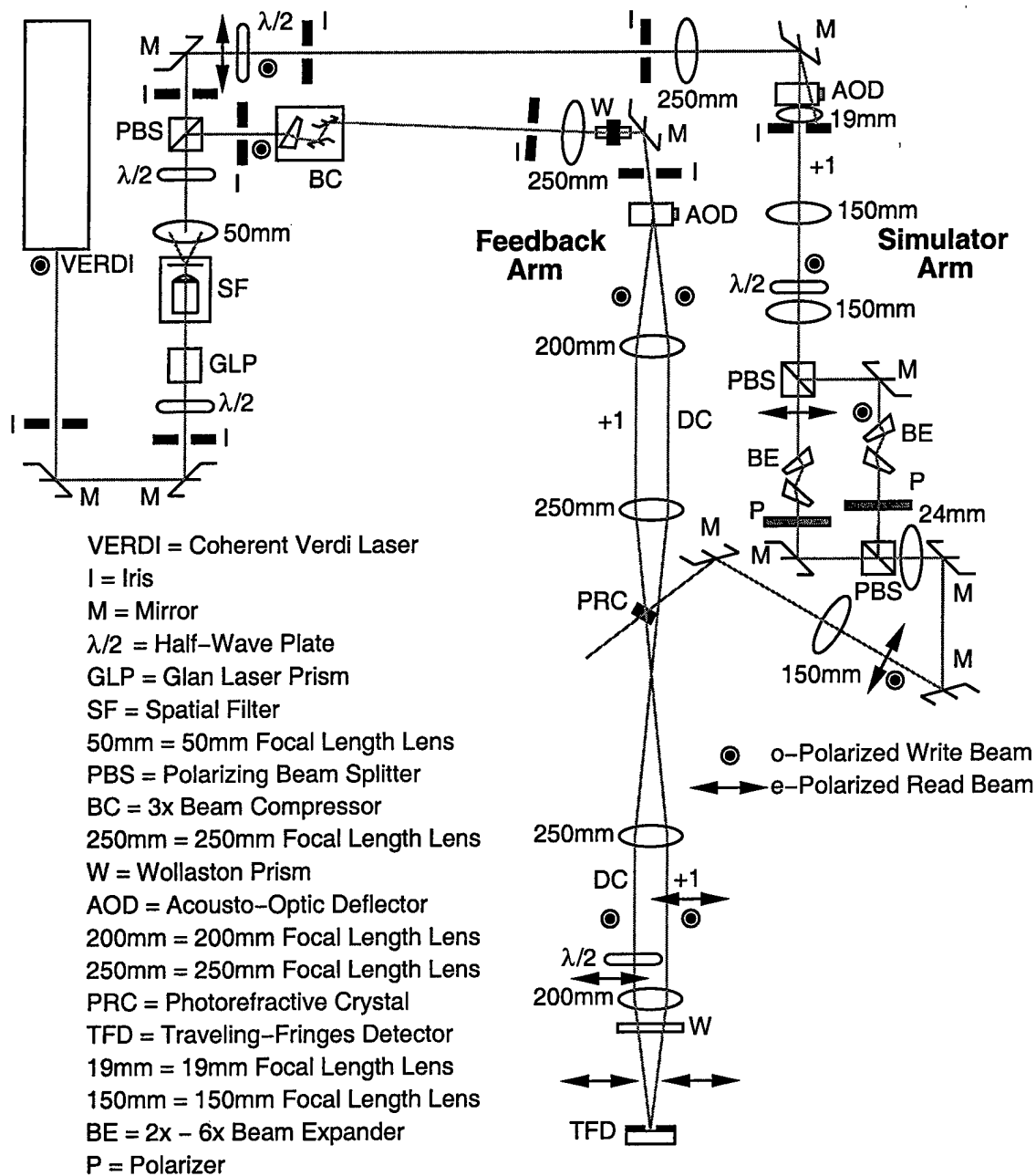
VERDI = Coherent Verdi Laser
I = Iris
M = Mirror
λ/2 = Half–Wave Plate
GLP = Glan Laser Prism
SF = Spatial Filter
50mm = 50mm Focal Length Lens
PBS = Polarizing Beam Splitter
BC = 3x Beam Compressor
250mm = 250mm Focal Length Lens
W = Wollaston Prism
AOD = Acousto–Optic Deflector
200mm = 200mm Focal Length Lens
250mm = 250mm Focal Length Lens
PRC = Photorefractive Crystal
TFD = Traveling–Fringes Detector
19mm = 19mm Focal Length Lens
150mm = 150mm Focal Length Lens
BE = 2x – 6x Beam Expander
P = Polarizer

Figure 10: Detailed layout of the read-write polarization multiplexing architecture for isolation of the ô-polarized write beam from the ê-polarized read beam.

225 μm long—creating a tap-delay line with a total delay of 53.6 ns. The first diffracted order was then imaged into the photorefractive crystal where it interfered with the ô-polarized writing beam from the simulator arm of the BEAMTAP processor. Both the writing beams had a high degree of polarization purity ($\approx$ 40 dB) so that leakage of the writing beam into the reading beam could be minimized. The geometry of the setup was chosen such that the ê-polarized reading beam was Bragg matched to the dynamic holographic grating which formed within the photorefractive

| Single Tone Beamformed Output with Read/Write Isolation | Isolation of Writing Beam | Single Tone RF Feedthrough |
| (a) | (b) | (c) |
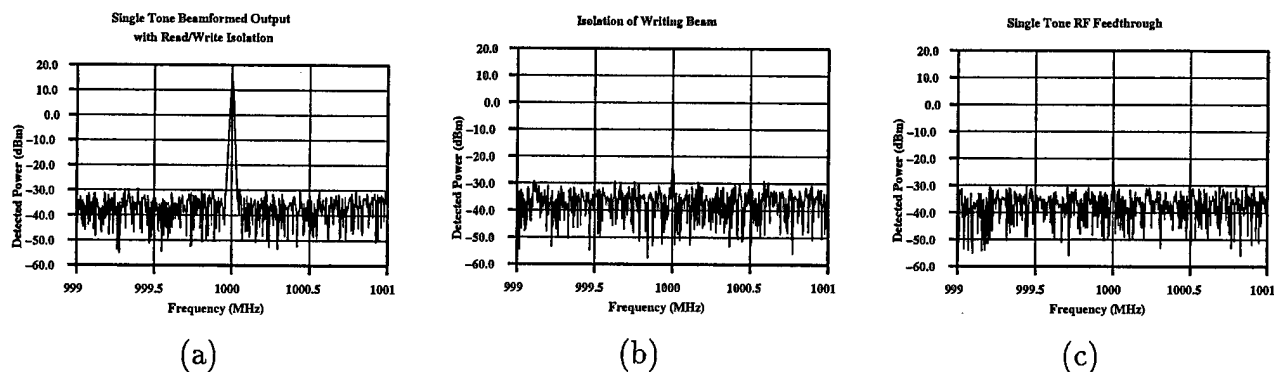
Figure 11: (a) Beam forming of a single 1 GHz tone with read-write polarization multiplexing. The detected power is that of the ê-polarized read beam. (b) The RF feedthrough in the system is of the same order of magnitude of the leakage of the writing beam. Note that the isolation of the writing beam is within 3 dB of the RF feedthrough. (c) The RF feedthrough in the system is of the same order of magnitude of the leakage of the writing beam. Note that the isolation of the writing beam is within 3 dB of the RF feedthrough.

crystal between the two ô-polarized writing beams. This reading beam thus effectively read out the weight matrix formed by the cross-correlation formed between the simulated array of signals in the simulator arm with the desired signal from the feedback arm of the processor. Since the diffracted ê-polarized reading beam was co-propagating with the writing beam containing the desired signal from the AOD, the two orthogonally polarized beams were passed through a Wollaston prism in order to spatially separate them. The interferometric reference DC beam with vertical polarization was passed through a half-wave plate to rotate the polarization to horizontal to match the ê polarized diffracted beam and was focused onto the TFD, where it interfered with the diffracted read-out beam from the photorefractive crystal. Since the velocity of the photogenerated carriers were resonantly matched to the velocity of the interference pattern, the detected output contained the coherent addition of each of the simulated antenna array element provided by the simulator arm of the BEAMTAP processor.

Figure 11a shows the detected beam-formed output for a single 1 GHz tone using the read-write polarization multiplexing technique. The detected power which is shown is that of the ê-polarized read beam, since the read and write beams were spatially separated using the final Wollaston prism shown in Fig 10. When light from the read beam was blocked in the simulator arm of the processor, the signal detected at the output of the TFD was minimized since the writing beam was isolated from the reading beam. Figure 11b shows that the writing beam has been isolated from the reading beam by 40 dB. Further reduction can be achieved by the use of polarization-angle multiplexing as described in the January issue of Applied Optics.[1] However, note that the RF feedthrough in the system, as shown in Fig. 11c, is within 3 dB of the leakage from the writing beam, showing that a substantial amount of isolation has been achieved.

20 MHz Beamformed Chirp with Read/Write Isolation
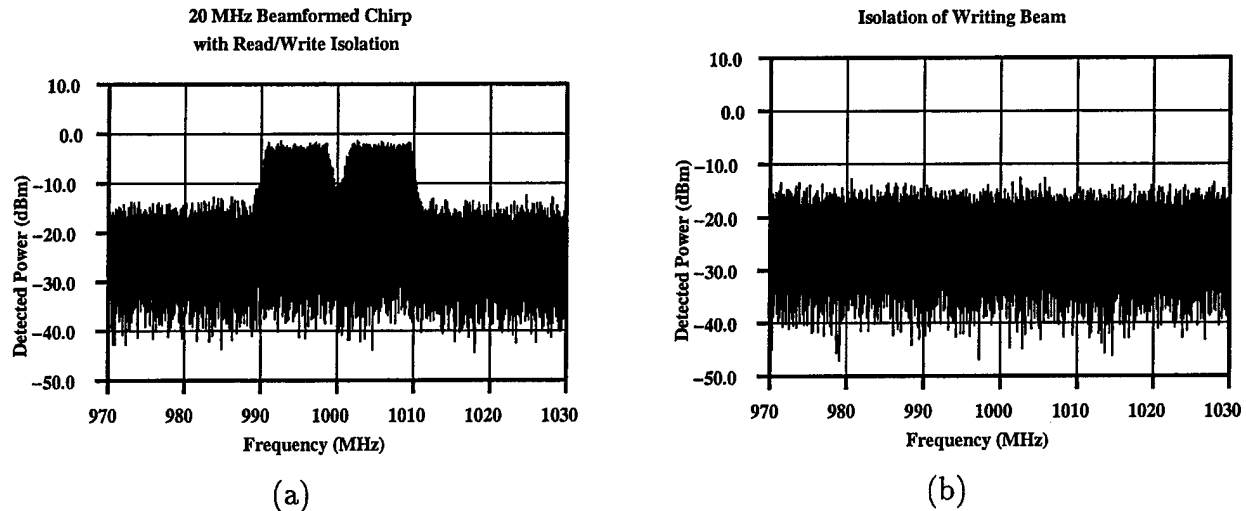
Isolation of Writing Beam

Figure 12: (a) Detection of a chirp spanning 20 MHz with read-write isolation. (b) Isolation of the writing beam is such that its power level is below the noise floor of the spectrum analyzer.

Finally, Figs. 12a and 12b show the detection of a chirp spanning 20 MHz with the read-write isolation technique and the isolation of the writing beam from the reading beam, respectively. Notice that the spectrum of the chirp has been faithfully reconstructed so that the detected output contains the coherent addition of each of the simulated antenna array signals, and has achieved the full coherent gain of the beam-formed output as described the BEAMTAP algorithm.

3.4 Sonar adaptive array

During the course of the year, an architecture of an optical adaptive array processor which operates at sonar frequencies has been implemented in order to verify the simulation tools used to demonstrate the effectiveness of the BEAMTAP algorithm. Both open and closed loop adaptation have been performed, and the simulation results have been verified. This system uses a more conventional time-delay-and-sum LMS adaptive antenna architecture to contrast with and to serve as a comparison to the BEAMTAP architecture.

3.4.1 Optical Architecture

Figure 13 schematically illustrates the optical architecture used in this adaptive array implementation. A scrolling spatial light modulator (SLM) is used in order to represent delayed versions of the input signal, composing the spatio-temporal plane $\underline{s}(k)$. This plane is diffracted by an adaptive hologram and is spatially integrated at the output differential heterodyne detector, producing the scalar output signal $o(k)$, which is subtracted from the desired signal $d(k)$
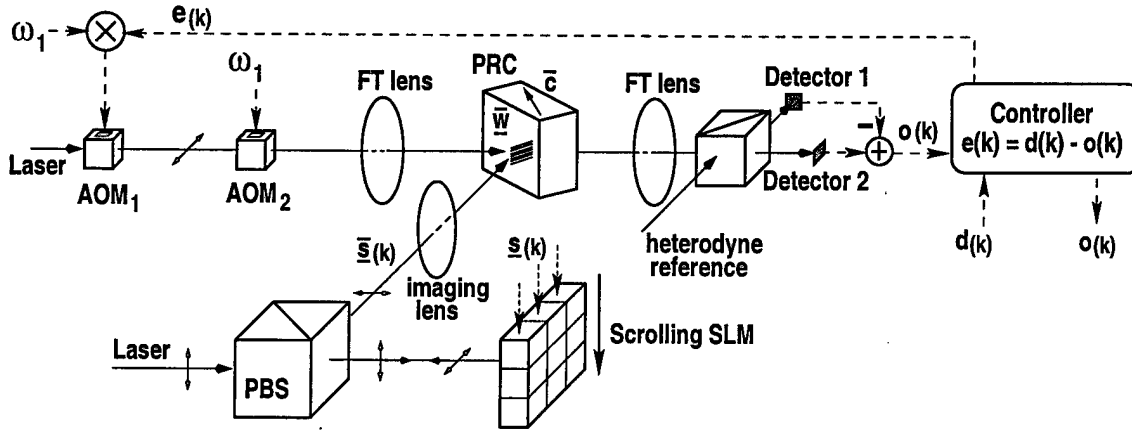
Figure 13: Architecture of an optical adaptive-array processor operating at sonar frequencies.

to produce the feedback error signal $e(k)$. The error signal modulates the first acousto-optic modulator AOM_1, and AOM_2 is used in order to bring the RF Doppler shifted signal back to baseband. The interference pattern between the beams conveying the error signal and the input plane performs the outer-product necessary to adapt the holographic weights $\overline{w}$.

3.4.2 Implementation

Figure 14 shows a picture of the experimental setup, with the beam path illustrated by the grey arrows. The scrolling SLM is implemented using a ferroelectric liquid crystal (FLC) SLM, in which the successive frames simulate the continuous arrival of acoustic sonar waves at an arbitrary AOA. The adaptive hologram is implemented with a photorefractive $BaTiO_3$ crystal. A lock-in amplifier (not shown) is used to detect and correct phase drifts in the reference beam by compensating with a mirror mounted on a piezoelectric crystal in the reference beam path. This provides the optical processor with long term stability.

3.4.3 Experimental Results

After adaptation is complete, the photorefractive weights converge to the spatio-temporal auto-correlation of the desired signal. In each column the spatial position of the correlation is determined by the relative time delay between the input signal wavefront at the corresponding antenna element and the desired signal, which varies according to the range from the source to that antenna element. For a far-field signal, the source is effectively seen at infinity, and this auto-correlation is produces a straight slice tilted at an angle proportional to the sine of the AOA of the input signal. For a near-field signal emitting a spherically diverging wavefront the distance from the source to a specific antenna element varies quadratically and the auto-correlation slice is, therefore, curved.

Figure 15 shows an image of the input beam being diffracted from the photorefractive crystal
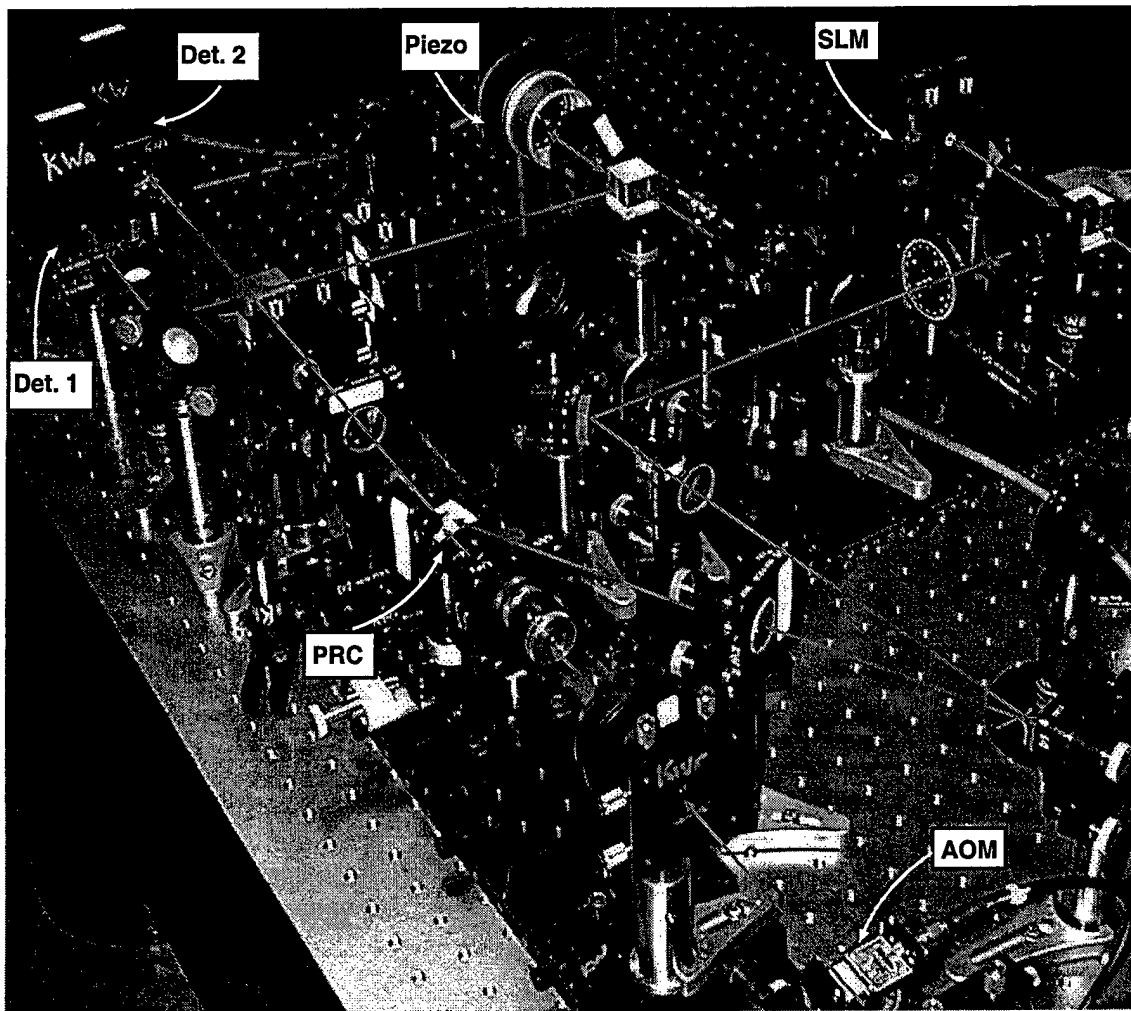
Figure 14: Optical implementation showing the scrolling SLM, acousto-optic modulator, photorefractive crystal, phase stabilizing piezo-mounted mirror, and differential heterodyne detector. The grey arrows show the various beam paths.

after adaptation with a far-field input signal was used, which yields a straight correlation pattern. The tilt varies adaptively with the AOA of the input signal, as expected. Figure 16 shows the same image when a near-field input signal is used. Notice the characteristic tilt and curvature of the correlation slice. Also notice that these images allow for an accurate determination of the spatial position of the source.

Since this processor implements a correlation-cancellation loop, it is also capable of nulling jammers. The following results illustrate the detection of a broadband signal in the presence of a narrowband jammer. Figure 17 depicts the output spectrum when the loop is open, showing the presence of a strong jammer at 280 Hz. Figure 18 depicts the output spectrum after the feedback loop is closed, showing that the detected jammer has suffered a power reduction close to 30 dB. The remaining spectrum corresponds to that of the desired broadband signal.
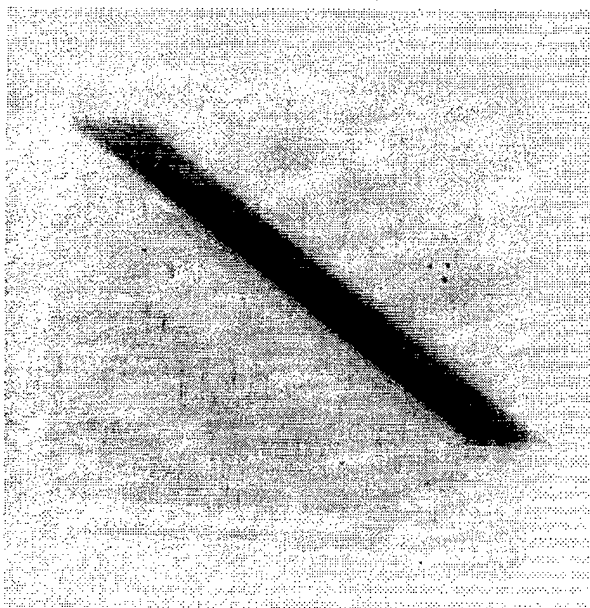
Figure 15: Image of the input beam after diffraction from the photorefractive crystal, showing the correlation between the desired signal and the input signal when the source is located in the far-field.
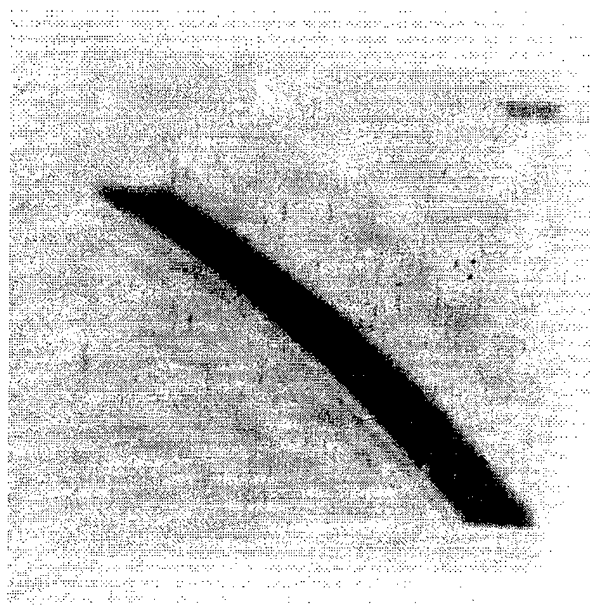
Figure 16: Image of the input beam after diffraction from the photorefractive crystal, showing the correlation between the desired signal and the input signal when the source is located in the near-field.
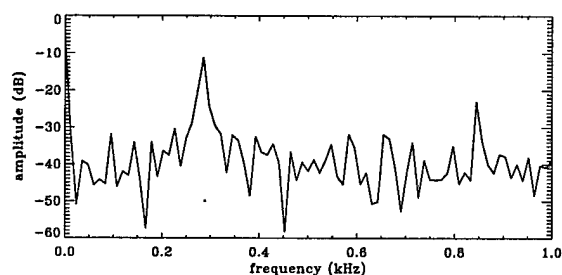
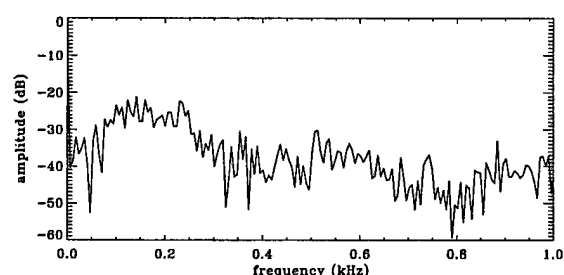Figure 17: Output before closed-loop adaptation, showing the presence of a strong jammer.

Figure 18: Output after adaptation, showing 30 dB of jammer nulling.

3.5   3rd year BEAMTAP Progress Summary

Table 4 provides a description of the completed progress during year three. The hole resonance response of the TFD has been characterized, and a transimpedance amplifier is being used to improve the SNR. In addition, new TFD detectors are being designed using semiconductor CMOS technology in order to optimize the performance of the detector. The multi-signal emulator was created, and although the emulator has not yet been used to probe the system's angular response, applications to transmission have been investigated. Recently much progress has been

Table 4: Year 3 Progress

Year 3 Plans	Completed	In Progress
Characterize TFD Hole Resonance		
Demonstrate high TB product	×	
Explore device optimization and fabrication	×	
Multi-Signal Emulator		
Probe system angular response		×
Investigate applications to transmission	×	
Demonstrate BEAMTAP System		
RF feedthrough isolation	×	
Implement read/write multiplexing	×	
Close feedback loop for jammer nulling		×
Investigate All-Optical BEAMTAP System		
Demonstrate fiber TDLs and coherent fan-in		×
Explore 1.06 μm star couplers vs. side tapped arrays		×
Characterize 1.06 μm AODs		×
Characterize 1.06 μm EOMs	×	
Additional Year 3 Progress	**Completed**	**In Progress**
Single-Layer FIRNN Sonar Processor Implemented		
Scrolling FLC-SLM acts as antenna tapped-delay line	×	
AOMs implement modulated feedback arm	×	
Microcontroller board calculates feedback	×	
Differential heterodyne detection used for stabilization	×	
Lock-in amplifier stabilizes reference beam phase	×	
Experimental Demonstration of FIRNN System		
Open-loop beam forming operation demonstrated	×	
Closed-loop jammer nulling operation demonstrated	×	
CCD input and Fourier plane images captured	×	
Imaging of photorefractive weights performed	×	
Experimental Adaptation Parameters Explored		
Adaptation to near field signals demonstrated	×	
Narrowband jammer nulling demonstrated	×	
Broadband jammer nulling demonstrated	×	
Multiple signal detection demonstrated	×	
Multiple jammer nulling demonstrated	×	
Circular array beam forming demonstrated	×	
Circular array jammer nulling demonstrated	×	

made in isolating the RF feed through in the system, and polarization multiplexing for read–write isolation has been implemented. Once the system response has been optimized over the full bandwidth, the feedback loop will be closed in order to provide the jammer-nulling capabilities of the BEAMTAP processor.

During year 3 we also began a new and originally unplanned effort to implement an optical time-delay-and-sum LMS antenna array beamformer, and have made substantial progress with a full operational system operating on simulated sonar array data. Experimental demonstration of the system includes open- and closed-loop beam forming and jammer nulling, successful capture of the input and Fourier plane images of the scrolling-delay line to compare the experimental results with simulations, dynamic imaging of the photorefractive weights, as well as an exploration of the experimental adaptation parameters. Adaptation to near field signals, narrowband and broadband jammer nulling, multiple signal detection, multiple jammer nulling, and circular-array beam-forming and jammer-nulling experiments have all successfully been performed using the adaptive FIRNN system.

3.5.1 BEAMTAP Plans for Year 4

Table 5 outline the plans for year four. Specifics include further exploration of TFD technology to optimize the time-delay capabilities of the device with respect to the overall device efficiency, as well as fabrication and testing of silicon based devices. Compensation for the lateral shift introduced in the anamorphic prism pairs between the read and write beams will be corrected so that the multi-signal emulator can be used to probe the system angular response. In addition, the read/write multiplexing technique will be optimized over the full 500 MHz bandwidth so that the feedback loop can be closed in order to perform jammer nulling in the BEAMTAP system. Finally, once the 1.06 μm AODs arrive, the devices will be fully characterized so that the feasibility of implementing the all-optical BEAMTAP system can be determined.

3.6 BEAMTAP Progress and SOW

Described below is the BEAMTAP phased-array processing statement of work from original MURI '97 Photonics for RF Array Processing proposal. The proposed plan for Phase 1 is compared with our progress, and the plan for Phase 2 is discussed in light of subsequent developments.

3.6.1 BEAMTAP phased-array processing SOW and Phase 1 progress

1. The optoelectronic BEAMTAP algorithm will be fully explored, its operation verified, limitations will be identified, and numerical simulations will be performed.

   - During the past three years under Phase 1 of the program, the opto-electronic BEAM-TAP algorithm has been fully explored, its operation has been verified theoretically and numerically, and the limitations in its performance have been identified.

Table 5: BEAMTAP Plans for Year 4 - from 1999 report and MURI proposal

Year 4 Plans
Further Explore TFD Technology
Optimize time-delay capabilities vs. efficiency
Fabricate and test silicon based devices
Multi-Signal Emulator
Compensate for lateral shift between read/write beams
Probe system angular response
Demonstrate BEAMTAP System
Optimize read/write multiplexing over full bandwidth
Close feedback loop for jammer nulling
Investigate All-Optical BEAMTAP System
Demonstrate fiber TDLs and coherent fan-in
Explore 1.06 μm star couplers vs. side tapped arrays
Characterize 1.06 μm AODs

2. A main-beam-forming optical BEAMTAP processor will be demonstrated using acousto-optic technology and tap-in delay line technology implemented using an off-the-shelf TDI CCD.

   - Beam forming has been successfully implemented over an 80 MHz bandwidth in addition to read-write multiplexing over a 20 MHz bandwidth, which is required in order to close the adaptive loop for broadband jammer cancellation.

3. A GaAs TDI CCD array will be designed, simulated and fabricated by MOSIS to extend the speed of the detector used to implement BEAMTAP, and it will be incorporated into the beam forming BEAMTAP processor.

   - The experimental system has been implemented using acousto-optic and photorefractive technology, but uses a traveling-fringes detector (TFD) in place of the TDI CCD as the tap-in delay line. The TFD was used due to the operating frequency limitations on currently available CCD technology. As a result, new silicon TFD devices, instead of CCD devices, have been designed and are currently being fabricated by MOSIS

in order to achieve greater sensitivity. If successful, an optimized detector will be incorporated into the beam-forming BEAMTAP processor.

4. A performance comparison will be made between the BEAMTAP approach and the CT approach to phased array processing. Strengths and weaknesses of each design will be evaluated, and a decision will be made as to which parts of each research area will be continued.

- A systems level analysis of the BEAMTAP system has been completed, but is still in progress for Coherent Transient array processing. Until both approaches are experimentally demonstrated and evaluated, a fair comparison of the technological strengths and weaknesses can not be completed. Consequently, the comparison of these approaches will be delayed until Phase 2 of the MURI program.

Substantial progress not originally envisioned in the MURI SOW has been additionally made, and is highlighted here.

- A fully functional optical time-delay-and-sum adaptive array processor has been designed, built, demonstrated, and characterized. Although this system operates at a substantially lower bandwidth (more appropriate for sonar array processing) it provides a valuable testbed for many of the issues to be faced in the BEAMTAP implementation.

- Development of a new architecture, the cohered fiber all-optical BEAMTAP, which uses the optical propagation in fibers in order to provide us with the necessary time delay for true-time delay processing—without requiring the use of TDI-CCDs or AOMs and thus allows for a full 20 GHz processing bandwidth, has been completed.

3.6.2 BEAMTAP Phase 2 plans

The originally planned activities for Phase 2 of the MURI in the BEAMTAP project are shown below, and are discussed in light of our plans for the next two years.

1. A fully adaptive BEAMTAP beam forming and multiple broadband jammer cancellation system will be constructed using RF photonics technology, and its performance will be characterized under a wide variety of spatio-temporal signal environments. Performance areas such as SINR, nulling bandwidth, spur-free dynamic range, and adaptation time will be quantified for comparison purposes.

2. Advanced beam forming algorithms, new devices, and new methods of antenna control will be most aggressively included at this point of photonic system evaluation and design update. If feasible a BEAMTAP adaptive nuller will be combined with a quasi-optical beam forming front end.

During the next two years under Phase 2 of the project, the fully adaptive BEAMTAP beam forming and multiple broadband jammer nulling system will be implemented using the RF photonics technology mentioned above. Like the FIRNN adaptive sonar processor which has already been successfully implemented and characterized, the BEAMTAP processor will be characterized under a wide variety of spatio-temporal signal environments. The noted areas such as SINR, nulling bandwidth, spur-free dynamic range, and adaptation time will be quantified for comparison purposes. In addition, the advanced beam forming algorithms, devices, and implementations will continue to be pursued and evaluated in the design of the final processor.

4 Optical Coherent Transient True-Time-Delay

Principal Investigator: W. R. Babbitt, Montana State University, Dept of Physics

This year we continued our investigation of the continuously programmed true-time delay (TTD) in optical coherent transient (OCT) materials. We have developed a simulator based on coupled Maxwell-Bloch equations to achieve high echo efficiency of continuous programming in a thick medium. The calculation on 10 GHz bandwidth indicates the echo efficiency is maximized at 7 % for an optimum thickness of $\alpha L = 3.5$, which is more than one order of magnitude higher than what is obtained with thin media. We have also performed extensive experimental studies on the dynamics of the accumulation of spectral grating over a 10 GHz bandwidth which match well with our simulations. The grating dynamics have been studied in two cases where the probe pulse is either coherent or incoherent with the programming pulses, respectively. The later one mimics the case of simple OCT TTD while the former one may be useful to enhance the signal strength in envisioned adaptive beam forming systems.

As we planned for this year, continuous programming at a 4 kHz repetition rate were performed. We observed 0.3 % echo efficiency on the steady state of the thin medium. A large part of our effort continues to be focused on demonstrating TTD on signal with up to 10 GHz bandwidth. While we have probed the broadband-programmed medium with a CW laser beam, we have not yet put high bandwidth modulation on this optical carrier due to the low damage threshold of our broadband modulator. To solve this problem, we proposed and did initial testing of an injection locking diode laser system, in which a high power free running slave diode is locked to a low power broadband-modulated master diode to generate up to a 100 mW optical beam, sufficient to meet our needs. The setup and the characterization of the system are in progress. As a short-term alternative to using the broadband modulator, a 4-bit data pulse was generated from a single 30 ps laser pulse passed through a multi-path delay line. The data mimicked a signal with a bandwidth greater than 2 GHz and preliminary results with a delay of about 10 ns were promising.

We have also theoretically and experimentally studied the spectral filtering of broadband phase modulated optical signal to enhance the processing and detection of broadband RF signals. Spectral filtering can be used to turn a phase modulated signal into an amplitude modulated signal to reduce the complexity in the detection system. We developed a new type of stabilized laser source by locking the frequency of a CW Ti:Sapphire laser to a non-persistent spectral hole burnt in the Tm^{3+}:YAG crystal. A stability of less than 6 kHz jitter over 3 ms has been achieved, ideal for our demonstrations. We demonstrated the continuous programming of TTD at low bandwidth with the stabilized laser and studied the dynamics of the build-up to steady state. Continuously programmed chirped TTD and auto-correlations have also been successfully demonstrated.

4.1 Dynamics of 10 GHz spectral grating: Simulation

In the first year report, the steady state analysis of continuously programmed, continuous processing of an OCT TTD device was presented for optically thin media. In the second year, the dynamics of the grating build-up in continuously programmed devices was investigated. These analyses showed that accumulated gratings could produce recall efficiencies on the order of 50 % of the perfect photon gated system, or roughly less than 1 % in a thin medium ($\alpha L < 1$). This year, a simulator was developed that could calculate the build-up and absolute recall efficiency of an OCT TTD device with an optically thick medium. In order to achieve high echo efficiency with accumulation we studied the echo efficiency versus medium thickness. The simulation was based on the coupled Maxwell-Bloch equations. A variant of the simulator was developed under our AFOSR grant to demonstrate that non-continuously (single-shot) programmed optical coherent transient memory that can have recall efficiencies greater than 100%. This was confirmed experimentally. In the case of memory, the first (programming) pulse and the third (recall) pulse act effectively as pumps from which energy is tapped on average from the spectral population grating producing gain. In the case of continuously programmed OCT TTD in material systems under study (Tm:YAG), inversion of the population can not be maintained at any spectral component. Thus, efficiencies exceeding 100% are not possible in Tm:YAG. However, thick media can be used to increase the efficiencies. Efficiencies versus absorption length were calculated for a 4 kHz repetition rate of the programming pulses and for pulse area of 0.1π. For 4 kHz, the efficiency was maximized at 7 % around $\alpha L = 3.5$. This is significantly higher than expected from thin sample calculations. Slightly higher efficiencies could also be achieved by optimizing the material and input pulse parameters. Additional gain could be achieved if a level system that produced inversion was employed. Conversely, gain can be achieved outside the OCT material via optical fiber amplifiers, which are being developed by the MSU Spectrum Lab.

4.2 Dynamics of 10 GHz spectral grating: Simulation

In last year's report, preliminary experiments on the dynamics of TTD 10 GHz gratings in Tm^{3+}:YAG were performed. This year we performed extensive experimental studies on the dynamics of the broadband spectral grating. Our mode-locking Ti:Sapphire laser with regenerative amplifier is capable of delivering Fourier transform limited, 7 ps, 300 μJ pulses at a repetition rate greater than 1 kHz. Filtering by an external etalon provided 50 μJ, 30 ps laser pulses. The experimental setup of the three-beam accumulated stimulated photon echo with a box geometry was described in last year's report. The two programming pulses along beams 1 and 2 are separated by delay time of 0.7 ns, and the probe beam is applied 0.2 ns after the second programming pulse. Initially, the dynamics of the accumulated grating were studied by inserting an optical chopper that periodically blocked the programming pulses while beam 3, containing the probe pulses, remained unblocked at all times. The chopper frequency was synchronized to a
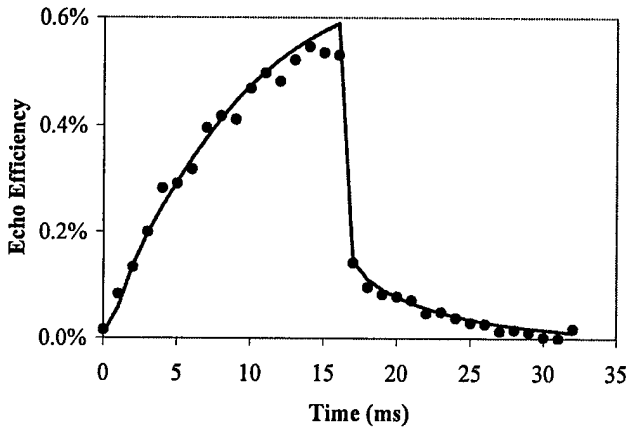
Figure 19: Accumulation with repetition rates of 1 kHz on 17 GHz bandwidth with the programming pulses were controlled by an optical chopper, and are thus coherent with probe pulse. Echo efficiencies were measured within the programming cycle of 32 ms. The dots represent the experimental results and lines represent the corresponding simulations.
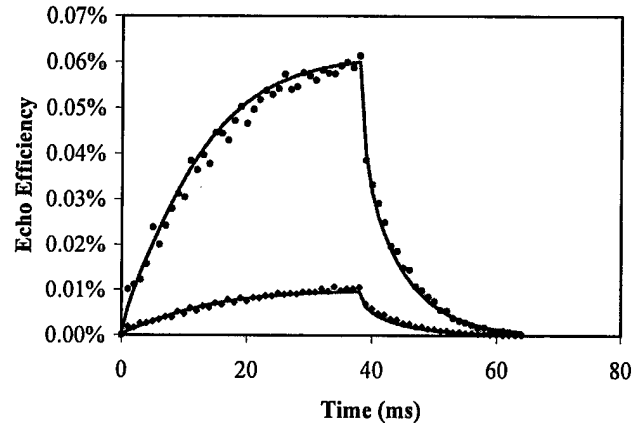
Figure 20: Accumulation with repetition rate of 1 kHz on 17 GHz bandwidth with the programming pulses were controlled by an AOM, and are thus incoherent with respect to probe pulse. Echo efficiencies were measured within the programming cycle of 64 ms with 38 programming and probe laser shots and 26 probe-only laser shots. Experimental results of the average of 512 cycles were plotted in dots and the corresponding simulation in lines.

sub-harmonic (1/32) of the 1 kHz laser frequency, yielding 16 accumulation shots with programming pulses unblocked and 16 grating probe shots with the programming pulses blocked. Beam 3 was attenuated using a neutral density filter of roughly O.D. = 0.5 to avoid saturation from the probe. In Fig. 19, the dots are experimental results of the echo efficiency versus accumulation time. The solid curve is the simulation. The sudden drop after blocking the programming beams is due to two effects. First is the decay of the excited state grating to the ground state. The lifetime of the excited state T_1 is 800 μs, and the branching ratio of the excited atoms that decay to the bottleneck rather than straight to the ground state is 0.56. This results in less than a 10% drop. The second effect is more significant due to the fact that there is a second grating accumulated in the medium that results in an echo at the same time and in the same direction as the expected signal. This results from beams 1 and 3 acting as programming beams and beam 2 acting as a probe beam. The echo is phase matched in the same direction as the echo resulting from pulse 3 probing the grating of beams 1 and 2. This added contribution to the echo signal only occurs when beams 1 and 2 are unblocked since it is stimulated by beam 2. The contributions are roughly equal in amplitude and the detected signal is the square of the output amplitude. We see a drop of roughly a factor of 4 due to this effect after beams 1 and 2 are blocked.

Typically in continuously programmed, continuously processed TTD, the phase relationship between pulses 1 and 2 would be the same for all programming pulse pairs in order to achieve coherent accumulation, while pulse 3 would be an uncorrelated data stream and incoherent with respect to pulses 1 and 2. To demonstrate the dynamics of the single grating under the conditions expected for the continuously programmed OCT, we introduced an acousto-optic modulator (AOM) in place of the chopper. Since the AOM frequency is not synchronized with the laser repetition rate, the AOM has the effect of introducing a random phase between beam 3 and beams 1 and 2 (which have a fixed phase relationship). This resulted in pulses 1 and 2 having constant phase relation with respect to each other, but random phase relation with respect to pulse 3. Thus, the grating due to beams 1 and 2 accumulated coherently, while the grating due to beams 1 and 3 accumulated incoherently. The ratio of the signals from these two gratings drops roughly with the number of laser shots. The echo signals generated by the coherent and incoherent grating could add constructively or destructively, but on average the combined signal would be that of only the coherent grating. Figure 20 shows the results for 38 laser shots with all three beams unblocked followed by 26 laser shots with only the probe beam unblocked. We no longer see the dramatic drop when pulses 1 and 2 are blocked. The fluctuations of the echo signal during accumulation are likely the result of the incoherent build-up of the grating due to pulses 1 and 3. The maximum echo efficiency is about 0.06 %, agreeing with our simulations under these non-optimized parameters. As we planned for this year, we increased the repetition rate to 4 kHz (the laser's maximum repetition rate) to investigate the accumulation dynamics when the repetition period is shorter than the excited state lifetime, and to improve the echo efficiency. An AOM was set to allow 66 programming and probe laser shots and 62 probe-only laser shots. Figure 21 shows the results for full (O.D. in beam 3 only, upper trace) and attenuated (O.D. in all beams, lower trace) programming. The fit parameters, as expected, are the same as in Fig. 20 since the laser pulse energies were roughly the same in both cases. The echo efficiency for full programming power (upper curve) was about 0.3 %, close to the value expected for a relatively thin sample.

The significance of the above results for coherent and incoherent probes is the care that must be taken in the application of the probe beam. Good agreement with the simulation results enables us to model the effects and performance of systems with various coherent properties. In the case of pure TTD devices, the probe should be incoherent with respect to the programming pulses. Yet, in the case of adaptive beam forming, coherence between the programming and the probing beams could be used to enhance the signal output, as seen above. The results also show that in the case of pure TTD, since incoherence is preferred, the laser that probes the media can be a separate laser from that which programs the media, allowing for greater flexibility in the design of the system.

To study the dynamics of the grating on a continuous basis, we probed the broadband continuously programmed medium with a CW laser, which will be used in the future as the RF signal
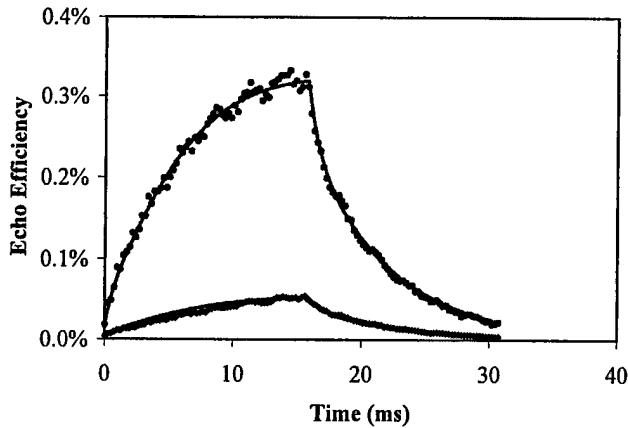
Figure 21: Accumulation with repetition rate of 4 kHz on 17 GHz bandwidth with the programming pulses were controlled by an AOM, and are thus incoherent with respect to probe pulse. Echo efficiencies were measured within the programming cycle of 31 ms with 66 programming and probe laser shots and 62 probe-only laser shots. Experimental results of the average of 512 cycles were plotted in dots and the corresponding simulation in lines.
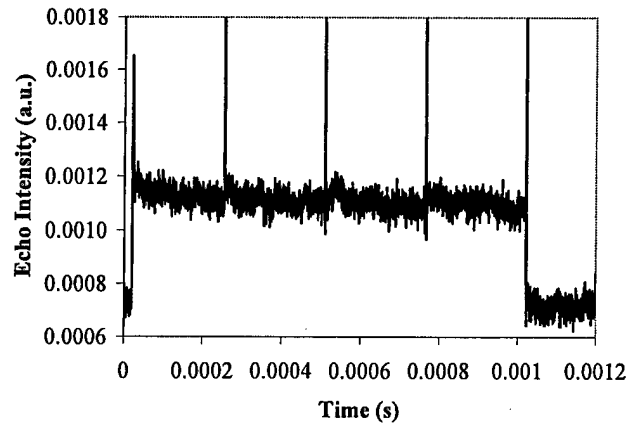
Figure 22: Detected echo power when probed with a 1 ms-long pulse at the steady state of the spectral grating on 17 GHz band showing grating droop and refresh. The grating was created and maintained by continuously programming at 4 kHz repetition rate. The spikes are scattered light from the programming pulses.

carrier in broadband TTD demonstrations. The medium, a Tm:YAG crystal, was programmed by repeating two 30 ps pulses at 4 kHz. The probe beam was a 1 ms-long pulse from a CW Ti:Sapphire laser modulated by an AOM. Figure 22 shows the echo intensity from the medium programmed to the steady state. (The spikes are scattered light from the programming pulses.) Although the spectral grating is periodically refreshed to steady state, it decays between two programming pulses. Thus the ratio of the echo efficiency before and after a programming pulse pair depends on the time interval between the two programming pulses. For 4 kHz repetition rate, the ratio is greater than 0.8. This ratio can be made closer to 1.0 if the repetition rate is increased. This demonstration also shows the ability to probe a grating produced by one laser with separate laser.

An interesting effect was observed during the above CW probe experiment. When the CW laser beam was sufficiently strong, such that the Rabi frequency of the beam was much greater than the repetition and coherent decay rate, we saw in a time scale of a few microseconds a nutation-like variation on the echo intensity. The peak was about twice that of the echo intensity in the steady state. Its properties are still under study, but may be attributed to the combined effect of optical nutation and the interplay of the absorption and dispersion gratings in the medium. More significantly however, is that rather than saturating the grating and the

output going to zero, the output only drops to 50 % of its initial value after several Rabi cycles, which may be due to the complementary index grating that accompanies the absorptive grating. This effect will be explored further under our AFOSR grant.

4.3   Preliminary demonstration of 10 GHz true time delay

A large part of our effort continues to be focused on the demonstration of TTD for signals having up to 10 GHz of bandwidth in an OCT material. We planned on carrying out these demonstrations in Tm:YAG using the output of a mode-locked Ti:Sapphire picosecond laser with a regenerative amplifier to program the material and the modulated output of a continuous Ti:Sapphire ring laser to probe the programmed TTD. The design for this experiment was presented in last year's report. Unfortunately, the maximum optical power output of our broadband modulator (damage limited) is below that which is needed to produce a clearly detectable broadband output signal. A means for amplifying the lower output power of the broadband modulator is therefore needed, and we are pursuing a broadband injection locking technique to accomplish this. Preliminary results are encouraging and are discussed in the next section. An alternative to injection locking is the use of an optical fiber amplifier being developed by Spectrum Lab. We will evaluate both paths and employ one of these techniques to accomplish our goal of demonstrating OCT TTD over a 10 GHz bandwidth before the end of the year.

As a short-term alternative to the broadband modulator, a 4-bit data pulse generator was produced by passing the output of the picosecond laser through a series of beam splitters and delays. As above, the picosecond laser output was filtered by an etalon to provide 30 ps, 75 μJ pulses at a 1 kHz repetition rate. The laser output pulses were split into three beams: two programming pulses and one pulse to enter the data pulse generator. The data generator produced a 4-bit data pulse where the delays between the pulses could be adjusted independently. The intervals between the consecutive bits of the data pulse were 420 ps, 610 ps and 420 ps, respectively. The two programming beams crossed in the crystal with a small angle ($\approx$ 1/50 rad). The delay between pulses 1 and 2 was set to 12.4 ns. The data pulse was combined with and entered the sample in the same direction as beam 1. The energy of each programming pulse was 25 μJ and the energy of each bit of data pulse was 3 μJ. The medium was first programmed with 32 programming pulse pairs controlled with an AOM while an optical chopper blocked the data pulse. The data pulse was then sent into the medium when the programming pulse pairs were shut down at 1 ms. Figure 23 shows the input sequence which mimics a 2 GHz bandwidth input signal. Figure 24 shows the resultant output signal for our preliminary experiments with the data generator. The four main peaks on the right are the true-time-delayed signal. Note that the input sequence has two pre-pulses. This was due to the double pulses coming from the picosecond laser system, and also in part caused the pulse height fluctuations seen in the output signal. The discrepancy between the input data pulse and the detected output pulse is
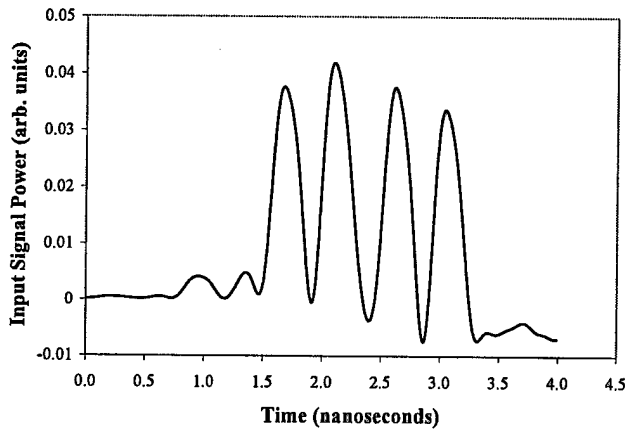
Figure 23: The 4-bit input data pulse before being sent into the broadband true-time delay generator programmed iwth a 12.4 ns delay. The intervals between the consecutive bits are 420ps, 610ps and 420ps. The pre-pulse is due to the double-peak mode of the picosecond laser system.
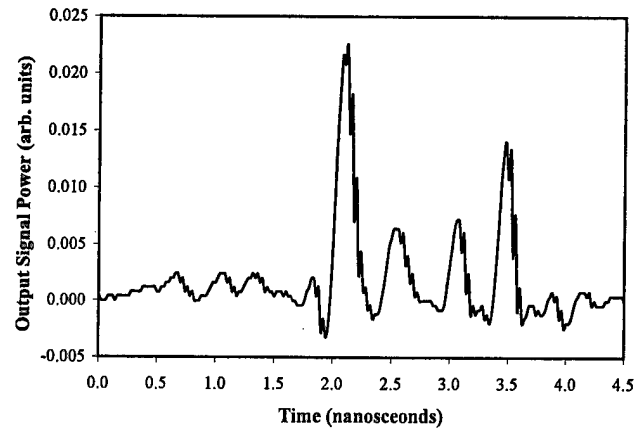
Figure 24: The 4-bit output signal from the true-time delay generator with 12.4ns delay. The origin of the time-scale is not the same as in Figure 23. The bit-to-bit height fluctuation was caused by the double-peak mode of the picosecond laser system and the imperfection of the spatial overlap of input 4 data bit with the programmed spot in the medium. Both situations have been corrected, but too late for inclusion in this report.

due to differences in the spatial overlap of the programming pulses with the individual beams that make up the 4-bit data pulse. Both situations are correctable and improved results are expected shortly.

4.4 Injection locking as a source for amplification of phase modulated carriers

Over the past several years, significant improvements have been made to electro-optic modulators. Among these improvements is a significant increase in bandwidth in excess of 20 GHz. However, these modulators are built using waveguide structures in $LiNbO_3$. Thus, in order to stay below the photorefractive damage in these modulators the optical power must be kept very low. This causes a problem, as the photon echo process usually requires a high amount of optical power. In order to overcome this problem within a reasonable time frame, a process to amplify the optical signal after being modulated by the broadband phase modulator was needed. A theoretically promising amplification process for these high bandwidth signals was found in the form of injection locking. Injection locking involves taking two lasers, one as the master and one as the slave, and injecting light from the master into the slave laser. This injected signal can then overcome the natural lasing of the slave laser and force the slave to lase and amplify the

master laser signal.

In the current research, an external cavity diode laser (ECDL) and a free running diode laser (FRDL) were used to do a preliminary test on the injection locking. The ECDL, in conjunction with a 1.8 GHz resonant phase modulator, was used as the master laser and the FRDL as the slave. The injected optical power at 790 nm was approximately 100 μW and the amplified signal from the FRDL was over 70 mW. An optical spectrum analyzer was used to scan the FRDL before locking and the FRDL after locking. The injection of the modulated master laser into the FRDL caused the FRDL to lock on to and to produce an amplified version of the master laser signal. The amplified signal had phase modulation sidebands that were 1.8 GHz apart, as expected. As a result, this preliminary experiment has shown that injection locking can be used to amplify phase modulated signals. Theoretically, this process can amplify broadband signals up to the relaxation frequency of the FRDL. With the correct choice of diodes and reflectivities we expect that this process will meet our needs for amplification of low power, broadband signals for the demonstration of broadband true-time-delay.

4.5   Spectral filtering and detection of broadband phase modulated optical signals

The question arises as to what is the most efficient and best means of encoding RF information onto an optical signal for phased array radar applications. There are several modulation options such as amplitude, phase, or frequency modulation, along with various modulation techniques including single sideband modulation. An important question that must be asked is what happens to these signals as they travel through the absorbing inhomogeneously broadened materials used in this study especially—when the spectral width of the modulated optical signal reaches the bandwidth of the material's broadening.

To help answer these questions a computer program was used to simulate the effects of modulating an optical carrier. The program simulates the optical carrier and allows the user to modulate the carrier with any one of the above mentioned modulation schemes. This allows realistic simulation of signals that will be encountered in any phased array radar system. The simulation employs two types of spectral filtering, transmissive and absorptive. Absorptive filtering is used if one wishes to simulate the effects of an absorption line on the signal as it passes through the material. However, transmissive filtering must be used to simulate any echo type signals as the photon echo process roughly follows first order scattering theory. Results from simulations show significant amplitude modulation from broadband phase modulation with bandwidths on the order of the spectral filter bandwidth.

Experiments were run to test the simulator for both transmissive filtering using etalons and absorptive filtering using the transition at 793.3 nm in Thulium. A broadband integrated optic phase modulator was used to CW modulate the 793 nm optical carrier from 1 to 13 GHz. A
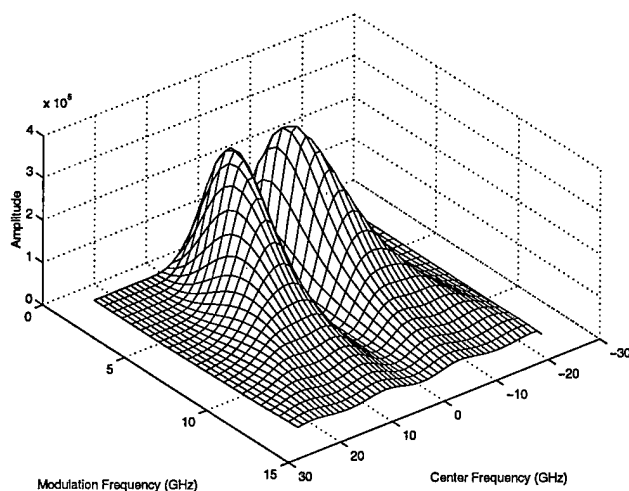
Figure 25: Simulation showing the amplitude of the induced power modulation as a function of the spectral filter center frequency and the phase modulation frequency for transmissive filtering.
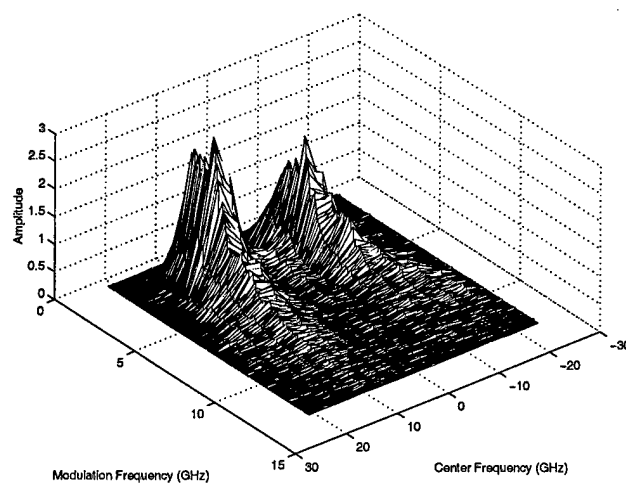
Figure 26: Experimental results for transmissive filtering using an etalon with a FWHM of 14 GHz. The plot shows the amplitude of the induced power modulation as a function of the spectral filter center frequency and the phase modulation frequency. The result compares well with simulation.

broadband detector (13.5 GHz bandwidth) was used in conjunction with a network analyzer to run the experiments. Figure 25 shows the simulated amplitude of the induced amplitude modulation from phase modulation as a function of center frequency and phase modulation frequency. Figure 26 plots the experimental results from an etalon with a FWHM of 14 GHz. Good agreement between the two plots is apparent. In Fig. 27, absorptive filtering using the Thulium transition is used to induce amplitude modulation from the phase modulated carrier. The amplitude of the induced amplitude modulation is plotted as a function of the phase modulation frequency, and both experimental and simulated results are shown.

Since such significant amplitude modulation was seen, the question arose as to whether or not this process could be used to some benefit. Thus phase shift keyed signals whose bandwidth was the same as the transmissive filters were simulated. The time-averaged output showed a distinct and detectable signal when the carrier frequency was close to the center frequency. Essentially, the phase shift keying was beat with itself to produce a detectable signal. This process could possibly be utilized to reduce complexity in detection systems by essentially removing the need to heterodyne detect phase shift keyed signals. Experiments to test this method for detecting phase shift keyed signals is in progress and will likely be finished in the coming months. These results will aid us in the determination of the proper signal modulation and detection schemes to use to optimize system performance.
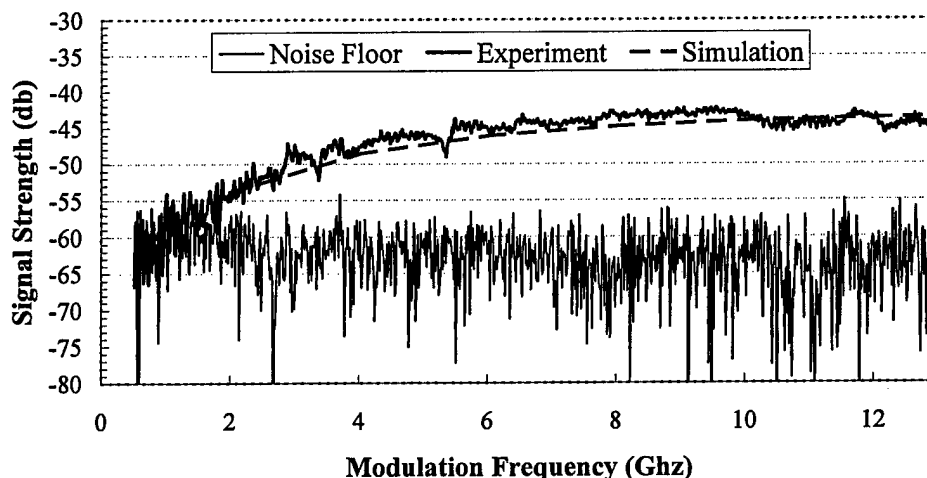
Figure 27: Experimental and simulation results using the Thulium transition at 793 nm as an absorptive filter to turn phase modulation into amplitude modulation. The plot shows the RF signal strength versus the modulation frequency. In this plot the optical carrier is tuned approximately 30 GHz off from the center frequency of the transition, which was measured to have a full-width-half-maximum of roughly 30 GHz.

4.6 Low bandwidth demonstration of continuous programming of a TTD

In this section we demonstrate the accumulation of a complex spectral grating by the repeated application of a pair of low power optical programming pulses to a non-persistent inhomogeneously broadened transition in Tm:YAG at 4.5 K, and subsequent probing of the material in order to investigate the buildup dynamics towards steady state. The necessary frequency stability for accumulation was provided by a novel technique for locking a CW Ti:Sapphire laser to a regenerating transient spectral hole in the same transition. A collinear application of the programming and probe pulses was used. Grating accumulation was demonstrated for a periodic spectral grating, representing a true-time delay. This work represents a step towards demonstrating an optical coherent transient continuously programmed continuous TTD processor.

To achieve accumulation of a complex spectral grating, a constant phase relationship between the programming pulses must be maintained. For a continuous-wave laser source that is crafted into programming pulses, its frequency stability is critical. The condition for the laser frequency jitter, $\delta\nu_0$, is that $\delta\nu_0 \ll (1/2\tau_{prog})$ over several times T_g, where τ_{prog} is the duration of a programming pulse pair. In the next section we discuss the stabilization techniques used to achieve sufficient laser stability for the low bandwidth demonstrations.

The experimental low bandwidth demonstrations were performed in single dipole Tm:YAG (0.1 % at., absorption coefficient of roughly 2 cm^{-1}), maintained at 4.5 K in a continuous flow liquid helium cryostat. The continuous-wave output of an Argon-pumped Ti:Sapphire laser,
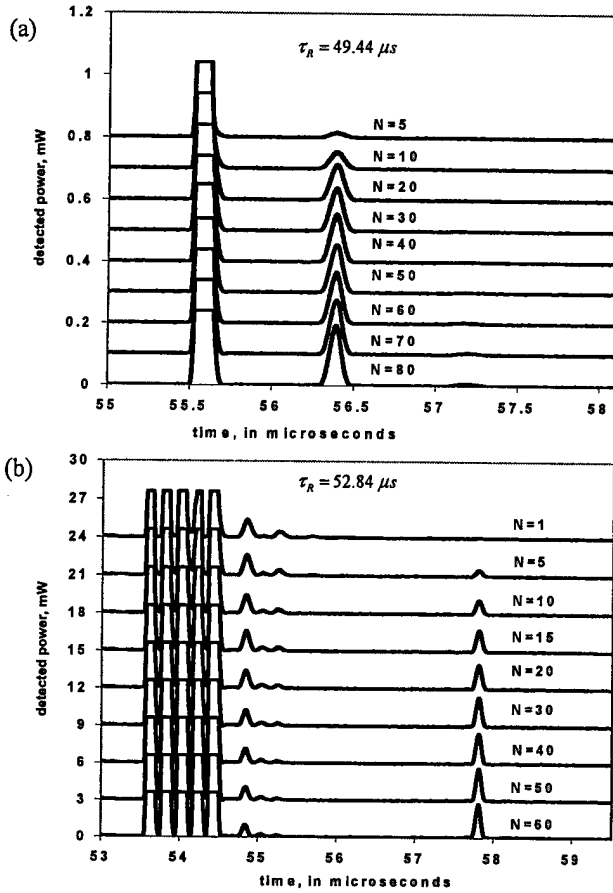
Figure 28: Plots of the emitted output signal from an accumulated grating as a function of the number of times, N, that the programming pulse pairs were repeated. (a) True time delayed signal: the single probe pulse is on the left, followed by the true time delayed echo signal on the right. (b) Correlation signal processing: the applied probe pulse is on the left, representing a 5-bit sequence data pulse $\{+,+,+,-,+\}$ modulated in amplitude and phase, followed by spurious echo signals and the auto-correlation peak of that data with the stored pattern.
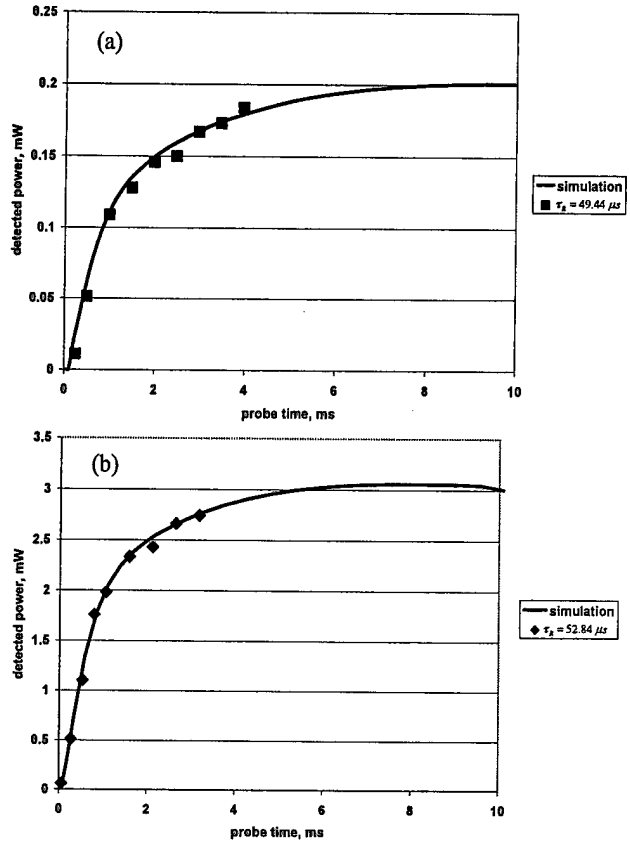
Figure 29: Plot of the peak power of the emitted echo signals corresponding to Figure 28 (a) and (b), respectively, against the time that the grating was probed, showing the dynamics of the spectral grating buildup towards steady state with a frequency stabilized laser. Simulated curves are also shown for an optically thin sample.

resonant with the Tm^{3+} on the $^3H_4 - {}^3H_6$ transition at 793.2 nm ($T_M = 25$ μs, upper state lifetime $T_1 = 800$ μs, bottleneck lifetime $T_b = 9$ ms), was first directed towards a double passed 80 MHz acousto-optic modulator (AOM) that introduced necessary corrections in order to keep the laser frequency locked to a transient spectral hole in the IBT in a separate 7 mm long Tm:YAG crystal at 4.5 K. Further details are in the next section. A measurement made during the demonstration showed the stability, when locked to a spectral hole, established an upper

limit of 13 kHz rms frequency jitter over 60 μs (measurement limited), compared to roughly 500 kHz rms when the laser was locked to an external reference cavity. The frequency-locked continuous-wave beam was crafted into pulses by a 125 MHz AOM and focused into a 140 μm spot ($1/e^2$ diameter) on the sample. All the optical pulses were applied colinearly to eliminate the effects of path length changes due to vibrations. After a pair of optical pulses was repeated N times, the grating was then probed with an optical pulse that stimulated an emitted signal, the strength of which represented the strength of the accumulated spectral grating.

The two reference pulses in each pair were separated by τ_{21}=800 ns, the pulse pairs were repeated every τ_R=49.44 μs, each at a power of 14 mW. After the pulse pair was applied N times, a single probe pulse with a power of 150 mW (not shown) was applied τ_R after the last programming pulse pair. Figure 28(a) shows single shot captures of the probe pulse and the emitted output signal for varying values of N, as detected after the sample. The time scale for each plot is offset by time $(N-1)\tau_R$. Figure 29(a) plots the strength of each signal peak versus the time in which the grating was probed. The total duration of the entire sequence of pulse pairs was limited to roughly 4 ms by the record length of the digitized RF signals produced by the AWG at 1 Gs/s. Thus, for the longest record length, the gratings were not completely in steady state when probed. For comparison to the data points, a simulation curve is shown, produced by integrating the optical Bloch equations for an optically thin sample. It is worth noting that when the Ti:Sapphire laser was locked only to an external reference cavity rather than to a spectral hole, the output signals either fluctuated dramatically or disappeared. Similar experiments were done to demonstrate continuously programmed optical processing (correlation) under our AFOSR grant and are shown in Fig. 28b and Fig. 29b. Recently, these results have been extended to 20 ms in our collaboration with MSU Spectrum Lab.

4.7   External stabilization of a Ti:Sapphire ring laser

A frequency stable laser source is necessary for studying the effects of continuous programming on optical coherent transient materials, which are best done at low bandwidths (much less than a GHz). The setup we used was adapted from experiments conducted by Profs. Cone and Carlsten of the MSU Physics Department based on the Pound-Drever-Hall technique. We were able to improve the frequency stability of an argon-ion pumped Coherent 899 Ti:Sapphire ring laser by using the transition in Tm^{3+}:YAG at 793 nm.

Figure 30 shows the setup for locking the laser. The output of the laser was first directed towards an acousto-optic modulator (AOM) in a double-pass configuration to correct the frequency of the laser. Part of the deflected beam ($\approx 1\ \%$) was passed through an electro-optic modulator (EOM) to add sidebands at 15.5 MHz to the fundamental frequency of the laser. The EOM output was then propagated through a 7 mm long Tm^{3+}:YAG crystal in a continuous flow liquid helium cryostat at 4.5 K. The detected signal output from the crystal was then mixed with the
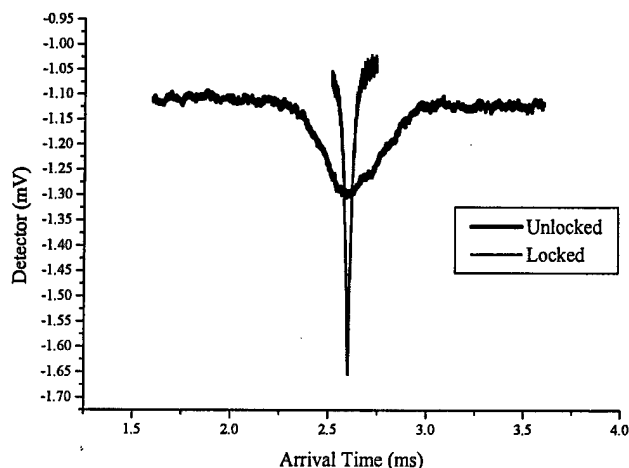
Figure 30: Apparatus for stabilizing the frequency of an argon pumped Ti:Sapphire ring laser. The electro-optic modulator (EOM) is used to put frequency sidebands on the fundamental at 15.5 MHz before it is sent to a 7 mm long 0.1 % Tm:YAG crystal. The signal detected after the crystal is mixed and processed to provide the frequency corrections to the acousto-optic modulator (AOM).

Figure 31: Comparison of hole widths with external locking on and off. When the external locking system is turned off, the frequency jitter is such that a narrow hole cannot be burned. However, when the external locking is turned on, we can see that the hole becomes significantly narrower and deeper, an indication that the frequency jitter has been substantially reduced.

same 15.5 MHz signal used to drive the EOM with the appropriate phase. The mixed signal was then used to drive a servo amplifier that drives the AOM. Long-term drift was also compensated by integrating the output of the servo amplifier to apply a voltage to the comparator internal to the laser reference cavity.

Stability measurements were made in a separate 15 mm long Tm^{3+}:YAG crystal in the same cryostat. The stabilized CW output was sent through two more AOM's. The first AOM was used to make a long (1 ms) pulse to program the material, and the second was used to generate a linear frequency scan (5 MHz in 5 ms) of the hole created with the first AOM. Any difference between the expected arrival time of the center of the hole, and the actual arrival time, translated directly into a shift of the frequency of the laser. The laser had an internal reference cavity to give it a stability of 500 kHz over 600 μs and $\approx$ 2 MHz over 3 ms. Locking to the spectral hole improved the stability to less than 6 kHz jitter over 3 ms. Figure 31 shows how the hole width varied between locked and unlocked modes of operation.

Based on the results of this work, a similar system was built to stabilize the Ti:Sapphire laser in the MSU Spectrum Lab and is now being used extensively in their correlation experiments. The improved frequency stability has been used in the demonstration of accumulated complex

spectral gratings with brief pulses (true-time delay) and with 5-bit barker codes (correlation). It has also been used to study how the grating builds up in time up to 20 ms and for the accumulation of chirped programming pulses.

4.8   3rd Year Optical Coherent Transients Progress Summary

Table 6 provides a description of the completed progress during year three. A Ti:Sapphire ring laser was stabilized and locked to a non-persistent hole and used to demonstrate fully continuously programmed TTD at low bandwidths, in addition to increasing the 10 GHz TTD continuous programming to a 4 kHz repetition rate. New progress has also been made which was not originally in the initial MURI proposal statement of work. A Maxwell-Bloch simulator of optical coherent transient TTD was developed to optimize efficiencies. The effects of coherence between the programming and probe pulses were simulated and measured, and the ability of spectral filtering to enhance signal detection has been theoretically and experimentally studied.

By the end of this year, we plan to have completed our demonstrations with the 4-bit data pulse and use this to investigate TTD signal fidelity and delay resolution up to several gigahertz. We will then implement our injection locking technique to produce broadband modulated signals up to 10 GHz that will be analyzed in the time and frequency domain for fidelity, delay resolution, and efficiency.

4.8.1   Optical Coherent Transient Plans for Years 4 - 5

In the next two years, the above system will be used to demonstrate spatial multiplexing of delays and the steering of a two-element antenna with OCT TTD. With the results of our experimental work and simulator, we will, in collaboration with the University of Colorado, design and analyze various OCT TTD systems and evaluate their performance. Integration of OCT TTD and signal processing into adaptive beam forming systems will be investigated and system designs will evaluated with the goal of implementing multi-gigahertz beam forming using OCT TTD materials.

4.9   Optical Coherent Transient Progress and SOW

Described below is the Optical Coherent Transient True-Time-Delay statement of work from the original '97 Photonics for RF Array Processing proposal. The proposed plan for Phase 1 is compared with the progress made by MSU PI's group and collaborators. We are close to being on track, with significant additional progress to report.

Table 6: OCT Year 3 OCT Progress - from 1999 report and MURI proposal

Year 3 Plans	Completed	In Progress
Develop stabilized system to lock Ti:Sapphire ring laser to a non-persistent spectral hole	×	
Use stabilized laser to demonstrate fully continuously programmed TTD at low bandwidth	×	
Increase continuous programming of 10 GHz TTD to 4KHz repetition rate	×	
Demonstrate TTD of signals in the 10 GHz bandwidth regime		×
Carry out phase and delay resolution measurements up to 10 GHz		×
Measure efficiency, bandwidth, delay range, and output fidelity up to 10 GHz		×
Steer a two-element antenna with OCT TTD (by 2001)		planned for 2001
Year 3 Additional Progress	**Completed**	**In Progress**
Develop Maxwell-Bloch Simulator of OCT TTD and use to optimize efficiencies	×	
Simulate and measure the effects of coherence between the programming and probe pulses	×	
Study theoretically and experimentally the ability of spectral filtering to enhance signal detection	×	
Develop injection locking system for amplifying output of high bandwidth modulator		×
Build multi-path delay line to create 4-bit data pulses for high bandwidth measurements		×

4.9.1 Optical coherent transient SOW and Phase 1 progress

1. An analytical investigation of continuously programmable optical coherent transient (OCT) true-time-delay regenerators will be undertaken. Studies will include delay resolution on wide-band signals (>10 GHz).

- We have simulated and experimentally verified the grating build-up dynamics for a continuously programmed material in Tm:YAG in both the low (40 MHz) and high bandwidth (17 GHz) regimes. This was aided by our development of a stabilization system to lock Ti:Sapphire ring laser to a non-persistent spectral hole, providing optimum performance. We frequency stabilized the Ti:Sapphire laser to demonstrate fully continuously programmed TTD at low bandwidth. We designed and assembled an experimental set-up that will lead to full demonstrations and characterization of continuously programmed true-time-delay in high bandwidth (17 GHz) regimes. Preliminary results of TTD of mock data pulses were obtained and final results are expected by the end of phase 1. These will include phase and delay resolution measurements up to 10 GHz. A Maxwell-Bloch Simulator of OCT TTD for thick medium was development, experimentally tested, and used to predict optimum efficiencies.

2. A practical OCT material capable of performing coherent transient processing for phase array radar applications will be developed.

   - We have surveyed a number of materials and found that thulium doped materials to offer the best performance based on their broad inhomogeneous linewidths (translates to broadband RF photonics processing), long dephasing time (translates to large time-bandwidth-product). Erbium doped materials offer the advantage of 1.5 micron operation, but its spectral diffusion characteristics are not as good as thulium, though there may be solutions to this. Both materials should prove to be practical and their usage will depend on required specifications of the system.

3. 10 GHz or greater simultaneous processing and delay, multicast beam forming, and spatial multiplexing of delays will be demonstrated using OCT materials.

   - A preliminary demonstration of simultaneous delay and correlation of a 4-bit data pulse with over 10 GHz bandwidth was performed and full results are expected by the end of Phase 1. Experiments demonstrating multicast beam forming and spatial multiplexing are in progress. The effects of coherence between the programming and probe pulses in multi-delay systems were simulated and measured. The simulator can be used to investigate the effects of interference in spatially overlapped delays. Demonstrations of high bandwidth delays depend on the manner of modulation and detection. We have studied theoretically and experimentally the ability of spectral filtering to enhance signal detection and will continue to explore various modulation options. We are developing an injection locking system for amplifying the output of the high bandwidth modulator that will give us more flexibility in the type of programming and processing system which can be demonstrated.

4.9.2 Optical coherent transient phase 2 plans

The originally planned activities for phase 2 of the MURI in the optical coherent transient project are shown below, and are discussed in light of our progress to date.

1. Using the results of the theoretical studies and the OCT materials development, beam forming on a two element 10 GHz radar antenna using optical coherent transient processing will be experimentally demonstrated.

2. As detailed in the BEAMTAP SOW section, a performance analysis of OCT processing will be carried out, and will potentially result in significant system re-design.

The 4-bit data pulse system using our injection locking technique to produce 10 GHz broadband modulated signals will be used to demonstrate spatial multiplexing of delays and the steering of a two-element antenna with OCT TTD. With the results of our experimental work and simulator, we will, in collaboration with the University of Colorado, design and analyze various OCT TTD systems and evaluate their performance. Integration of OCT TTD and signal processing into adaptive beam forming systems will be investigated and system designs will evaluated with the goal of implementing multi-gigahertz beam forming using OCT TTD materials.

5   Adaptive Array Algorithm Simulations

Principal Investigator: Lloyd Griffiths, George Mason University and Kelvin Wagner, University of Colorado, Dept of ECE

Based on the previously developed simulation tools, new simulations have been created in order to study several cases of interest, two of which are reported here. The first case concerns the effect of multiple input jammers on the final signal to interference plus noise ratio (SINR) of the system. The second case concerns the use of a pseudo-random sequence added to the broadband pilot signal, supporting the claim that previously unknown information can be conveyed by pointing the antenna pattern towards a known "desired" pilot signal.

5.1   The Effect of Multiple Jammers on the System's Final SINR

The LMS algorithm, on which BEAMTAP is based, has the ability to null multiple simultaneous jammers, but the null depth may decrease with the number of jamming sources. Similarly, wideband jammers may be harder to null than narrowband jammers. In addition, the nulling dynamics may also depend on the number of jammers and their bandwidth. Simulations were developed to test and demonstrate these behaviors for BEAMTAP.

Figure 32 shows the spatial-temporal spectrum of a broadband desired chirp at broadside in the presence of 16 broadband jammers (all covering the same 1 to 4 GHz bandwidth), incident on the array at random angles, as detected by the 64–element antenna array with 64 taps in the two delay lines—which are the only taped-delay lines (TDLs) required for the BEAMTAP algorithm. Notice that the presence of multiple jammers causes the jammer spectrum to cover a large area of the spatial-temporal spectrum, with the area proportional to the number of jammers present. The SINR evolution during adaptation, as shown in Fig. 33, is shown as a function of the number of jammers present in the spatio-temporal signal environment, where the number of jammers is varied from 1 to 256. The total jammer power is held constant as more jammers are added. Notice that the SINR always presents a quick initial improvement followed by a constant value at steady state provided that the learning rate is kept within its convergence boundary. However, the rate of adaptation is seen to slow down in the presence of more jammers.

Figure 34 shows a plot of the final SINR versus the number of jammers present with the jammers kept at least 0.2 rad away from the angle of arrival (AOA) of the desired signal. Since the jammers are randomly placed in space, an average of 7 runs were used in order to present statistically significant results. Notice that the SINR decays smoothly with the number of jammers, at a constant rate of about 1 dB per 25 jammers. In Fig. 35 however, the jammers were allowed to be randomly distributed over all angles, including the AOA of the desired signal. Consequently, when the jammer density reaches a critical value, the SINR drops drastically since the probability of jammers overlapping with the desired signal (*e.g.* main beam jammers) increases.
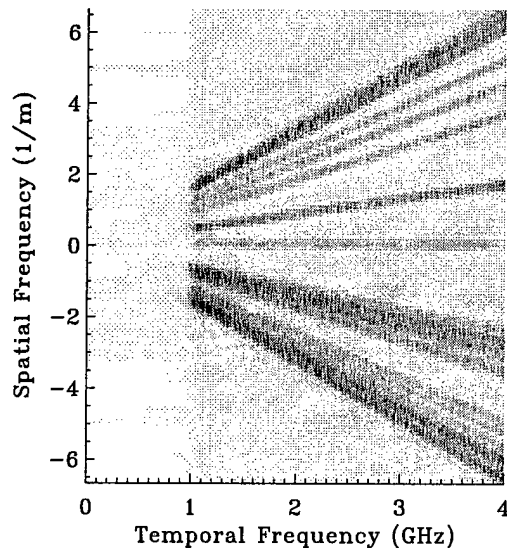
Figure 32: Spatio-temporal Fourier transform of the multiple jammer input signal, as detected by the antenna array.
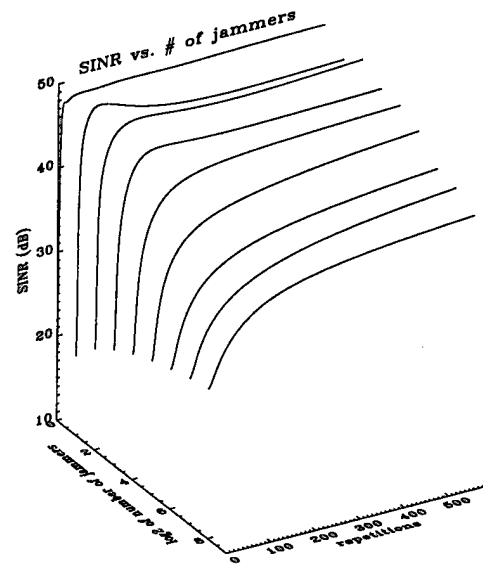

Figure 33: SINR progression during adaptation for an exponentially increasing number of jammers.
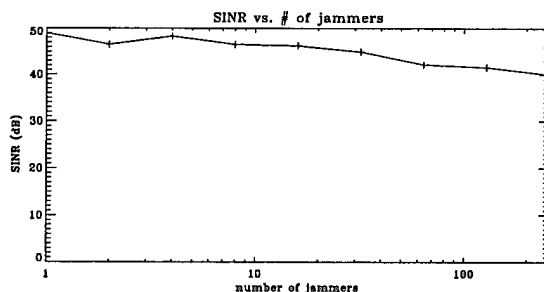

Figure 34: Final SINR versus number of jammers. Jammers are kept 0.2 radians away from the AOA of the desired signal.
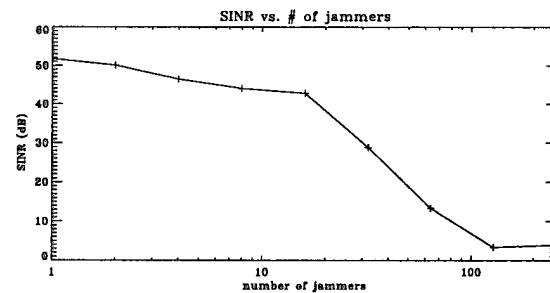

Figure 35: Final SINR versus number of jammers. A sharp decrease in performance is detected when the number of jammers is larger than 16.

This drop-off point is proportional to the number of antenna elements in the system, since more antenna elements allow the antenna directivity pattern to have a narrower main lobe, increasing its angular discrimination.

We also studied the relationship between the number of jammers present and the adaptation time required to reach the steady state value for the SINR. Initially, it was expected that more time would be required to reach steady state, as more jammers would cause a larger spread of the eigenvalues governing the adaptation, and thus reduce the rate of convergence. Such an effect was
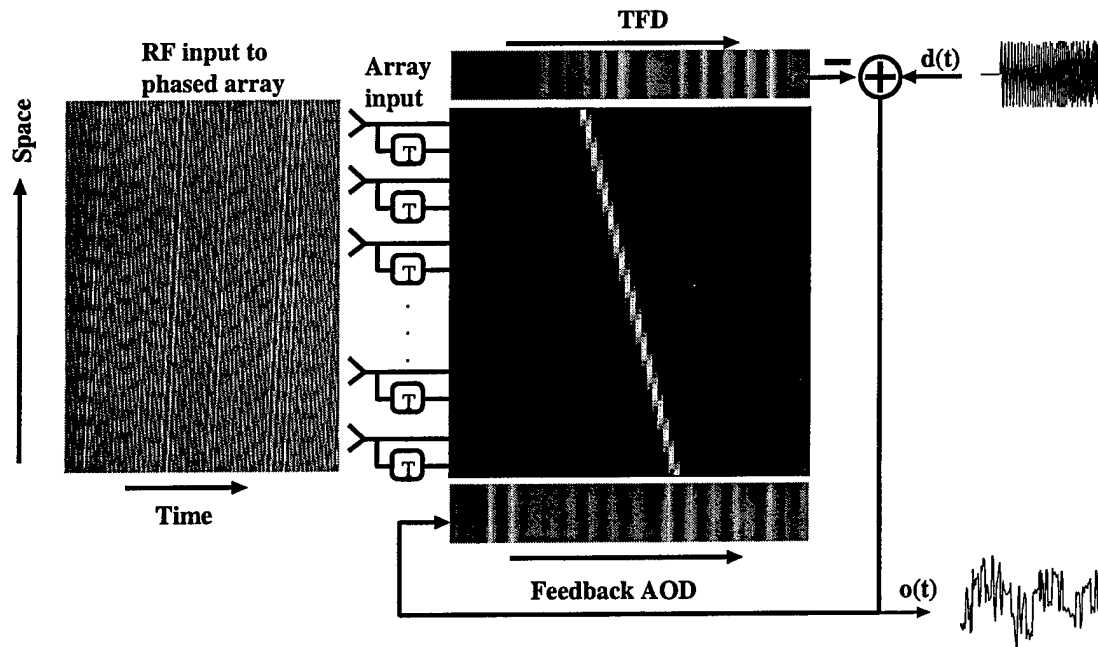
Figure 36: BEAMTAP array used for communications. The incoming RF wavefronts are detected by the antenna array and are multiplied by the adaptive weights. The output delay line delays and time integrates the partial products, producing a signal which is subtracted from $d(t)$, the pilot signal. At steady state, the remaining signal consists of a projection of the input signal in a direction orthogonal to that of the pilot signal, providing us with the information signal, which occupies the same spectrum of, but which is uncorrelated with, the pilot signal.

observed. However, this effect is accompanied by a reduction in the final SINR, which thereby decreases the number of iterations necessary to reach steady state. Therefore, no substantial decrease in the dynamic performance of the array has been observed.

5.2 BEAMTAP array for communication

Antenna array adaptation is performed by the use of the BEAMTAP algorithm, which is a modified version of the least mean square (LMS) algorithm requiring the presence of a previously known "desired" signal in the input. One might question the utility of this algorithm when used for communication between a remote signal source and the receiving antenna array, since if the transmitted signal is already known, a question arises as to how unknown information can be transmitted. However, arbitrary information can still be effectively transmitted by adding it to a known signal (piggy-back), as shown in Fig. 36. The incoming RF signal, which consists of the low power information signal added to a pilot signal, and possible jammers, is detected by the antenna array and is locally multiplied by the adaptive weights. The partial products are temporally delayed and accumulated at the output delay line, producing a signal which is
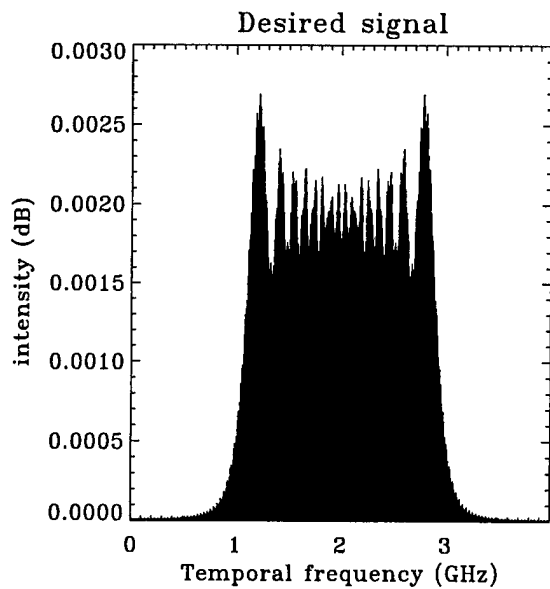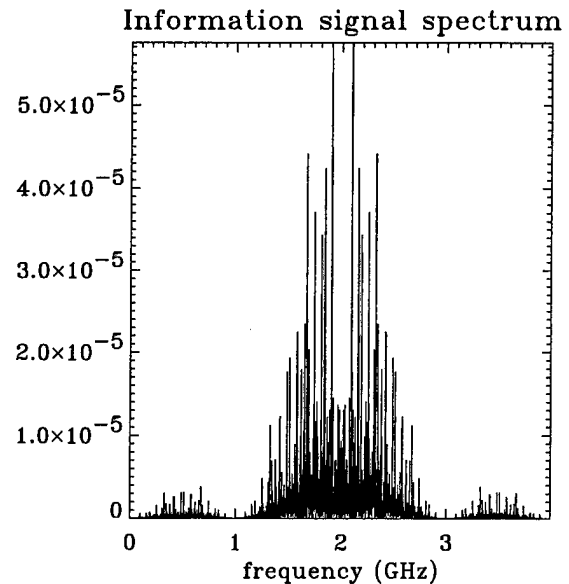
Figure 37: Spectrum of "desired" pilot signal.

Figure 38: Spectrum of information bearing pseudo-random sequence.

subtracted from $d(t)$, the pilot signal. The difference is then fed to the feedback delay-line and its outer product with a delayed version of the input is used to adapt the weights. At steady state, the remaining signal consists of a projection of the input signal in a direction orthogonal to that of the pilot signal—providing us with the information signal, which occupies the same spectrum of the pilot signal, but is uncorrelated with it.

Figure 37 depicts the spectrum of the known broadband signal which functions as a pilot steering signal, redirecting the antenna pattern towards its source upon adaptation. After adaptation, the weights project the spatio-temporal input signal towards the direction of the desired signal such that the feedback error signal becomes orthogonal to the desired signal. Consequently, any orthogonal information which is super-imposed on the desired signal, even if at low power, will stand out in the feedback signal. Figure 38 depicts the spectrum of an unknown PNBPSK signal, which was generated by a pseudo-random number sequence (making it spread-spectrum), and then modulated to the same center frequency and the same bandwidth as the desired signal so that their frequency spectra overlap. This signal was then strongly attenuated and added to the known pilot signal, generated by a far-field source.

Because the power of the information signal can be kept low, adaptation is not hindered. Figure 39 demonstrates this by showing the receptivity pattern after adaptation in the presence of the information signal shown in Fig. 38 and a broadband jammer. Notice the strong response at AOA of the desired signal, 0.2 rad, while the jammer is strongly nulled at -0.2 rad—the information signal had almost no effect in the final array receptivity pattern. Finally, Fig. 40 shows a plot of the cross-correlation between the feedback error signal and the pseudo-random
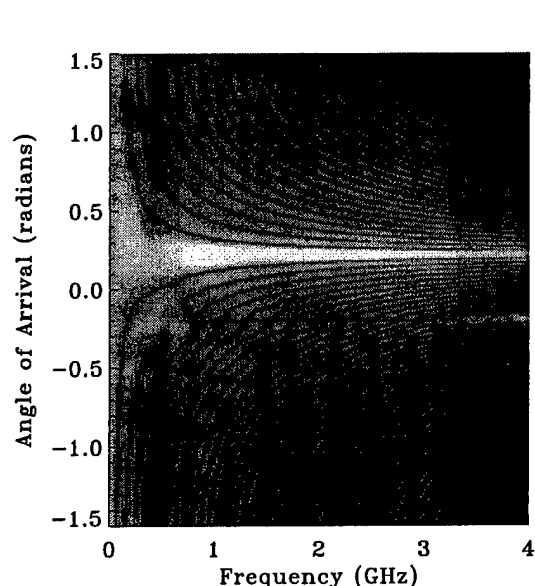
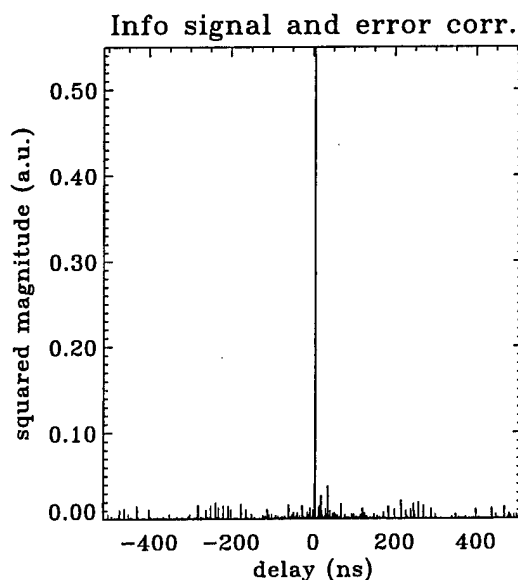Figure 39: Receptivity pattern after adaptation, showing a deep null at the jammer AOA.

Figure 40: Cross-correlation between error feedback signal and pseudo-random sequence, showing successful signal detection.

sequence. The strong correlation peak proves that this unknown information is present in the error signal and allows for various spread-spectrum communication techniques to be used in order to convey unknown information to the antenna array with the full antenna gain and jammer nulling capabilities of a BEAMTAP system.

5.3 Adaptive Array Algorithm Progress

Described below is the algorithm development for advanced array processing statement of work from original MURI '97 Photonics for RF Array Processing proposal. Because Prof. Griffiths assumed the duties of Dean at George Mason University with a primarily advisorial role to the MURI team, the character of the algorithm project evolved substantially. The proposed plans for phase 1 and 2 are highlighted below; then the actual progress is discussed.

5.3.1 Proposed Phase 1 SOW

1. Novel spatio-temporal array processing algorithms that are compatible with the capabilities and limitations of RF photonic array processing will be investigated and applied to both the BEAMTAP and OCT systems.

2. The algorithms to be investigated will incorporate arrays of blocking weights. Specific approaches include both p-vector steering, and other advanced beam steering and jammer nulling methodologies. The development will consist of theoretical evaluation and detailed

simulations.

5.3.2 Algorithm development phase 2 original plans

1. Optimization of convergence time under different scenarios will be investigated, and the results incorporated into system architectures.

2. The effects on algorithm performance of noise introduced by the optical hardware will be investigated. Robust algorithms that can mitigate these effects will then be developed.

Prof. Griffiths has played a key advisorial role to the MURI team on algorithm development and practical applications of adaptive array technology in a wide variety of important scenarios including (among others): circular adaptive arrays, hot clutter jammers, noise in array processing, Doppler processing, beam-space vs element space adaptation, and radar imaging.

5.3.3 Progress

Progress in algorithms during the past 3 years is highlighted below.

1. Year 1.

   (a) Development of the BEAMTAP algorithm: rigorous mathematical derivation of the BEAMTAP algorithm applied to the RF photonic array scenario.

      - Established solid background to support further investigations and to enable computer simulations

   (b) Design and development of simulation tools: computer algorithmic simulations have been created from basic principles and adapted to the adaptive antenna array scenario.

      - Creation of an IDL based GUI Array Processing simulation program.
      - Verification of the efficiency and operation of the LMS BEAMTAP algorithm.
      - Measurement of primary algorithmic metrics (convergence rate, misadjustment, computational complexity, etc.)

2. Year 2.

   (a) Simulation of complex scenarios: inclusion of realistic adaptive array system metrics in the simulations, such as the measurement of the array's receptivity pattern, inclusion of multiple broadband jammers, noise sources, etc.

      - Achieved a formal definition of jammer nulling.
      - Measured the dynamics of jammer nulling.

- Studied the effects of noise on the convergence rate, final convergence and final SINR.

(b) Simulation of specific scenarios of interest: study on the convergence rate, jammer nulling capacity and final receptivity pattern for the following realistic scenarios.

- Circular arrays.
- Presence of non-linearities in the input modulators.
- Information bearing capacity of the pilot signal.
- Presence of multiple signal sources (multi path).
- Investigation of adaptation in the presence of mutual coupling of array elements.

(c) Development of the adaptive array transfer function: rigorous analysis leading to a frequency domain transfer function capable of describing the system behavior in detail.

(d) Expansion of the BEAMTAP algorithm to multiple outputs: rigorous algorithmic analysis leading to the expansion of the BEAMTAP algorithm to adaptive antenna arrays which present multiple simultaneous outputs.

3. Year 3.

(a) Simulations showing the effect of signal binarization and photorefractive weight decay on the adaptive array. Effects on the convergence rate and final SINR, and final directivity pattern.

(b) Study on the effect of the number of jammers on the final SINR: investigation on the relation between the number of jammers and the degrees of freedom available to the adaptive system, and how this relation affects the final jammer nulling.

(c) Development of the delayed feedback temporal back-propagation algorithm, used in multi-layer, non-linear BEAMTAP.

(d) Analysis on the effect of noise sources (thermal noise, RIN noise, shot noise) on the final SINR. Determination of the upper limit on the maximum jammer nulling capacity.

6   The Optically Smart Antenna Array

Principal Investigator: Dana Anderson JILA, University of Colorado, Boulder

Adaptive processing in smart microwave antenna systems[5] is conventionally done after down conversion, using digital signal processing (DSP).[6] The adaptive DSP techniques have the advantage of being economical, flexible, and reprogrammable. However, they are typically power inefficient, have only modest bandwidth and exhibits relatively slow adaptation speeds. We present an X-band smart antenna array in which the adaptive processing is performed by nonlinear optical circuitry. Our goal is to develop a system that uses nonlinear optical techniques to simplify adaptive antenna systems by relieving the computational burden placed on DSP. The proposed optical circuit uses principal component extraction to separate a strong signal from other weaker ones. The optical processing alternative offers the advantage of higher bandwidth and shorter processing time, which is approximately independent of the number of signals. Furthermore, the optical approach offers the possibility of merging well with fiber link technology.

In the following we introduce a prototype of the optically smart antenna array. The architecture discussed is intended to be extended to applications with many antenna receivers, but for demonstration purposes, the current system uses only two antenna receivers and two test-sources. The optical portion of the system does not substantially change as the number of array elements grow.

The system is schematically shown in Fig. 41. The front end consists of a 30-element discrete lens antenna array followed by active antenna receivers positioned along the H-plane focal arc of the lens. Different receiver positions correspond to different angles of incidence for plane waves incident on the array. This provides a pre-separation of signals, but the signal isolation is limited by the gain pattern of these small antennas. Each receiver signal is down converted and is imposed on an optical carrier via electro-optic modulators. The modulated optical beams then go through the nonlinear optical circuit consisting of the carrier suppression stage and the auto-tuning filter. The carrier suppression precedes the auto-tuning filter and prepares the signals for the latter. The auto-tuning filter uses correlations between its input signals to distinguish between them and select the principal component. The incoming modulated beams contain a common optical carrier, which results in an unwanted correlation between the signals. The purpose of the carrier suppression is to remove this unwanted correlation by removing the common carrier, and carrier suppression is achieved by a two-beam coupling interaction[7] within a photorefractive barium titanate crystal and uses the principles of an optical novelty filter.[8] Similar techniques have been used for optical heterodyning,[9] the logical opposite of our problem. A more thorough explanation of the carrier suppression process is given in Section 6.3.1 below.

The auto-tuning filter is the core processor of the system. Its input is the direct output of the carrier suppression stage: an optical beam carrying only the sidebands of the phase modulated RF signals. The filter extracts the principal component from the various signals presented at
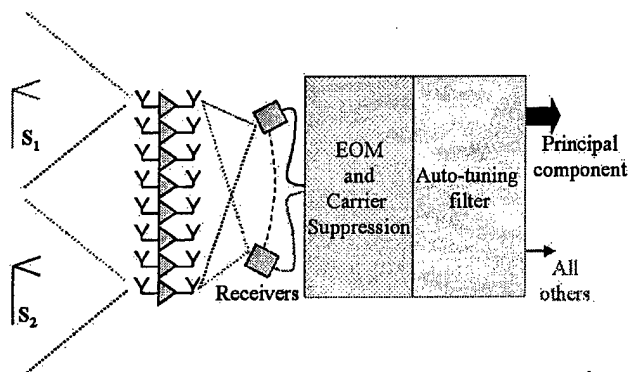
Figure 41: Block diagram of the prototype optically smart antenna array. The active receivers are positioned on the focal arc of the discrete lens antenna. The IF signals are then imposed onto the optical beam and processed by the adaptive optical circuit.
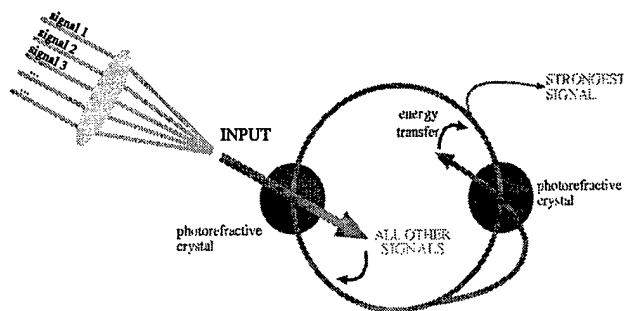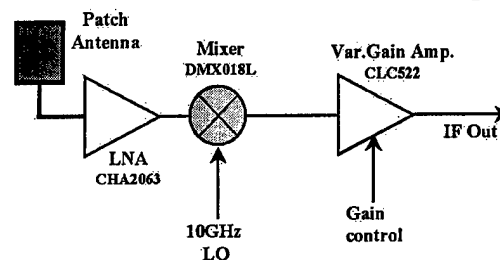

Figure 42: Schematic of the auto-tuning filter.

Figure 43: Block diagram of integrated active antenna and receiver.

its input. Figure 42 shows a schematic of the auto-tuning filter. The two disks in Fig. 42 represent photorefractive barium titanate crystals. One disk is a gain unit (left) and the other, a reflexive unit (right). The gain unit provides gain to the ring oscillator via a two-beam coupling interaction, and the input signal with the most power wins the gain competition necessary to establish oscillation in the ring, inhibiting all other weaker signals from also oscillating. The reflexive unit boosts the competition by enhancing the power contrast in the ring between the strongest signal and the others. Ideally, in steady state, the strongest signal is the only one to oscillate in the ring and therefore exits in output 1, whereas all the others exit in output 2 (see Fig. 42). On the next section we give a summary of last year's developments, followed by a more detailed account on each of the three basic components of the optically smart antenna array: the RF front end, the carrier suppression, and the auto-tuning filter.

6.1 Highlights of progress

In replacement of the 130 MHz transmission link previously used, an X-band link with down conversion on the receiver side has been implemented in close collaboration with Prof. Popović's group. A tunable source at 10 GHz and a horn antenna forms the transmitter. The present RF front end is composed of two sections: a lens antenna array (analogous to a Rotman lens) and the active receivers. The lens antenna performance has been measured for quantification of the pre-processing of the incoming signals in the form of angle-of-arrival detection. The two active receivers have been designed and assembled with the use of commercial devices in a small box.

Carrier suppression is a commonly needed task which is conventionally done using Mach-Zehnder interferometers[10] and other methods as well.[11] However, such methods prove to be difficult to obtain a carrier reduction ratio of more than 40 dB. We are now able to report a carrier reduction of more than 64 dB, which to our knowledge is the best ever reported. Such successful results come from the development of an original operator theory[12] for carrier suppression and the subsequent implementation of a new generation carrier suppression system using an evolved design and more compact optics, including an improved electro-optic phase modulator. Section 6.3 gives more details on the this year's progress of the carrier suppression stage. The three most significant figures of merit for the auto-tuning filter are the minimum input optical power, the bandwidth and most importantly, the contrast enhancement. The latter is a measure of how much the auto-tuning filter enhances the difference in power between the stronger and the weaker signals. We seek to improve these figures by following two avenues: one immediate and short-term project and another longer term one. In fulfillment of our short-term goal, we have designed and implemented a new, 2.5 cm diameter, auto-tuning filter using free-space technology and a novel crystal cut. The new compact filter is shown in Fig. 51(a). The contrast enhancement, minimum input power and bandwidth for this filter are, respectively, 26 dB/dB, less than 5 mW, and 3 GHz. This is a significant improvement when compared to the figures of the previous filter of 8 dB/dB, 50 mW, and 300 MHz. These improvements were necessary for assembling the two optical stages of the RF photonics system. On a longer-term project, we have investigated interesting, previously unknown, oscillation patterns occurring inside a barium titanate spherical disk. We observed a range of patterns, from the brighter triangles, the lowest order allowed, up to very faint hexagons. Pictures of the triangle and square are shown in Figure 53. These miniature oscillators, which are confined within a single crystal, could eventually lead to an ultra-compact, high stability and high bandwidth version of the filter, and therefore merits attention. The occurrence regions of the triangle patterns were mapped on an appropriate parameter space. We developed a simple model for the appearance of such patterns based on conventional two-beam coupling theory. This model is in close agreement with the measured occurrence regions for the triangles. Section 6.4 offers a more thorough description of the advances on the auto-tuning filter, both for the current system and for the spherical disk patterns.

6.2 The RF front-end: pre-separation of signals

Last year a low frequency (134 MHz) transmission link was implemented with the use of simple dipole antennas and commercial TV antennas for both the transmitter and the receiver. In particular, a 134 MHz carrier modulated by a noise source filtered around 100 kHz was transmitted. The receiver front-end was a filtering stage followed by a power amplifier driving the electro-optic modulator. This year we implemented an X-band link using a horn antenna on the transmitter side and a passive discrete lens with 30 patch antenna elements followed by
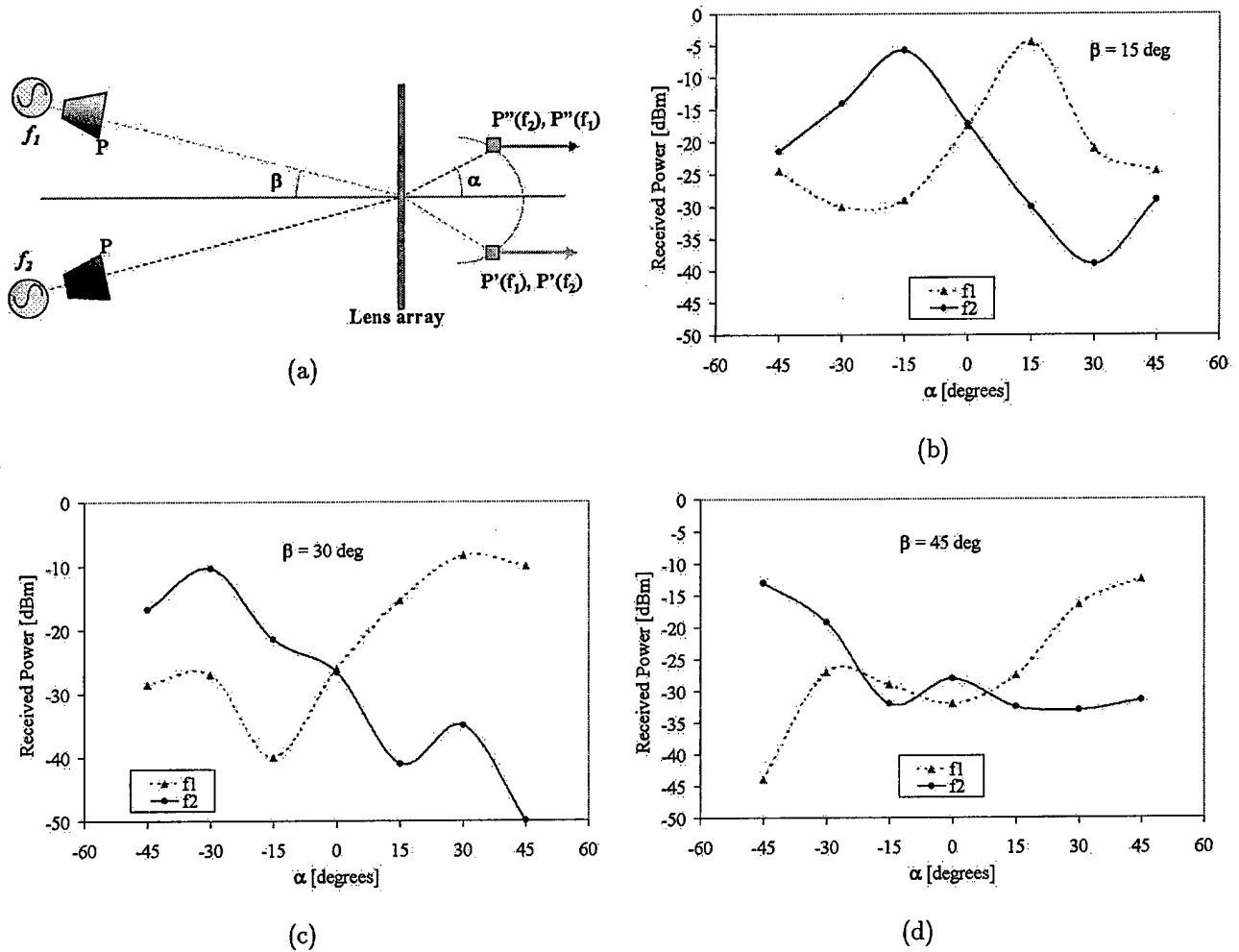
Figure 44: (a) Schematic of measurement setup used to characterize the multiple-receiver lens antenna array. Each transmitting antenna is located 0.8 m from the lens and transmits 25 dBm at frequencies 10 MHz apart around 9.9 GHz. Measured "cross-talk" between the two signals as a function of the receiver position along the focal arc (α) for different transmitter position: (b) β=15 degrees; (c) β=30 degrees; (d) β=45 degrees.

active antenna receivers (the RF front-end). The lens has a number of imperfect focal points, and in this demonstration we use two of these points along the focal arc to place receivers, each preferentially receiving one spatial beam from a specific angle of incidence on the lens array.

Each receiver is an active integrated antenna. The patch antenna feed is connected directly to a low noise amplifier (LNA) and then to a mixer down converter together with a dielectric resonator oscillator (DRO). The IF amplifiers then deliver the signal to the electro-optic modulator's drivers. Each receiver position on the focal arc corresponds to a specific direction of the plane wave incident on the lens array. The isolation, or "cross-talk" between the imperfect focal points for two signal sources was measured using the setup shown in Fig. 44(a).

The two sources have equal power levels at frequencies f_1 and f_2, which are within the bandwidth of the lens array and the receiving antennas on the focal arc. The two transmitters are in the far field equally away from the lens array and co-polarized with the receiving side of the lens array. The angle between the optical axes and the line of sight corresponding to each transmitter is β. The receiver is translated along the focal arc and signal powers are measured for different angles α in Fig. 44(a). For positions where $\alpha = \beta$, the receiver preferentially receives from one of the sources, but some signal from the other source is also present, and is referred to as the "cross-talk" signal.

The relative amount of the cross-talk depends on the spatial separation between the sources and is shown in Fig. 44(b)-(d). In most cases, the level of cross-talk is below 20 dB, e.g. when the transmitters are at $\pm 15°$ off the lens optical axis (Fig. 44(b)), the receivers placed at the corresponding positions will receive the two signals with a contrast ratio of about 25 dB. The contrast ratio depends also on the radiation pattern of the lens. The patch antenna is designed for 10 GHz, with a 2:1 VSWR bandwidth of about 150 MHz. The LNA amplifies the X-band received signal with optimal noise figure for the down conversion, while the IF amplifiers are wideband variable-gain amplifiers in order to balance the two IF channels. This is important for proper optical processing. They provide more than 40 dB gain control through a single high impedance voltage input.

6.3   The electro-optic modulation and carrier suppression

Last year we reported a carrier suppression system composed of two stages. The first stage consisted of the conventional approach of achieving carrier suppression by using an interference null and modulating around that null, for which, we used commercially available KTP amplitude electro-optic modulators (EOMs) with 350 V half-wave voltage. The following second stage consisted simply of a photorefractive two-beam coupling (TBC) interaction in a novelty filter configuration. This second stage suppressed any residual carrier resulting from the finite contrast of the EOM. That system provided a carrier reduction of about 30 dB, comparable to other reported carrier suppression systems.[10,11] This year, we redesigned the carrier suppression system to increase the carrier reduction, reduce the electrical and optical driving power requirements, and increase the optical stability. Throughout the process, we developed a new operator theory for carrier suppression.[12] This theory proved to be crucial in the development of our second carrier suppression generation system. Among other considerations, it showed that the photorefractive two-beam coupling stage alone was capable of perfectly suppressing the carrier, therefore dispensing the use of the prior stage which used an amplitude modulator to pre-null the carrier. This allowed us to greatly simplify the system by switching to an electro-optic phase modulator. We designed and built a phase modulator which significantly reduced the electrical power requirements on the input signals. Furthermore, we switched to 1"-high optics,
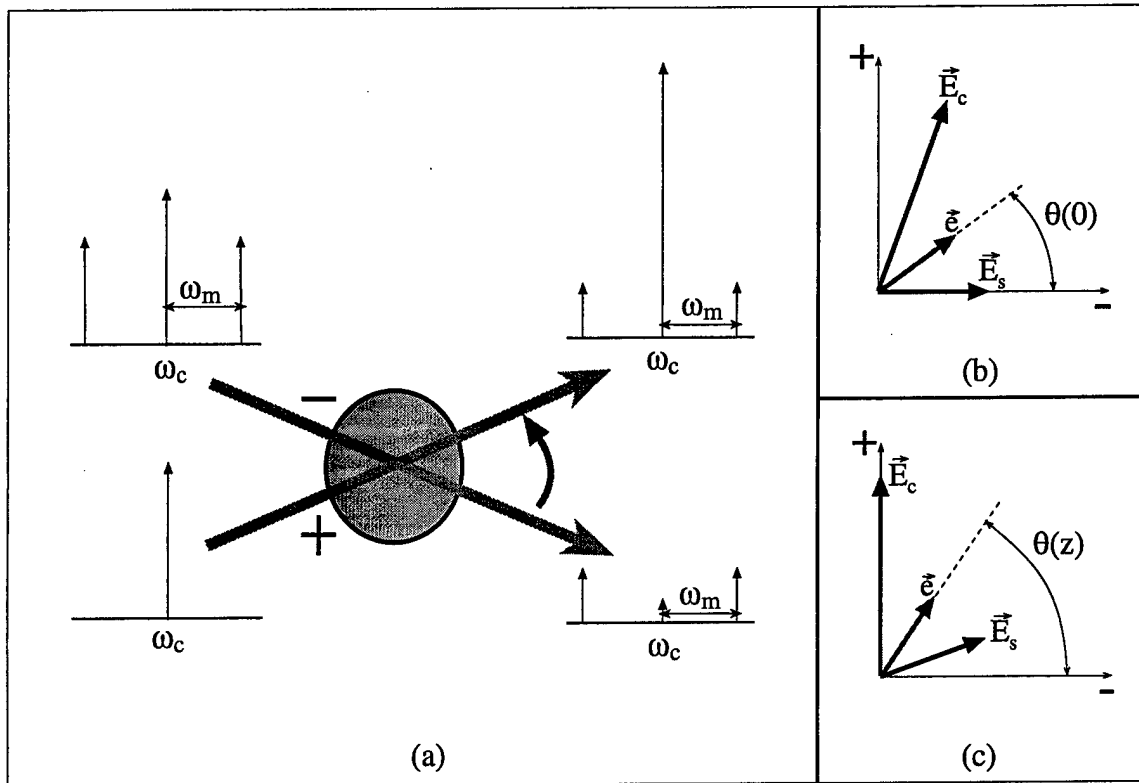
Figure 45: (a) Schematic diagram of carrier suppression. The input to the minus port is a modulated laser beam while that of the plus port is an unmodulated beam from the same laser. Two beam coupling causes the carrier at the minus port to be transferred to the plus port at the output. (b) Representation of the carrier and sideband vectors on plus-minus coordinate system. The principal eigenvector $\vec{e}$ embodies the dynamics of the system. (c) Position of vectors after rotation, such that the projection of the carrier into the minus-axis is null, resulting in a carrier suppressed output on that port.

which along with the smaller modulators, allowed us to build a more compact carrier suppression system, increasing the optical stability. In the next sections, we give a more detailed description of the carrier suppression theory, discuss the new EOMs, and, finally, demonstrate a new carrier suppression system which takes advantage of the new improvements.

6.3.1 A theory for carrier suppression

This last year, we developed the first theory for the photorefractive carrier suppression process.[12] This theory allowed us to better understand, and thereby optimize, the carrier suppression system. In the following, we give a summary of the theoretical development and its results.

In Fig. 45 we show a schematic of a two-beam coupling interaction in a novelty-filter configuration. The input to the "minus" port is a phase-modulated signal composed of the optical carrier, given by ω_c, and the upper and lower sidebands spaced by ω_m from the carrier. The

input "plus" port contains unmodulated carrier. The two beams cross inside the photorefractive crystal where optical energy is transferred from the minus to the plus beam, ideally depleting the carrier from the output minus port, while attenuating the sidebands by only about 3dB. The energy-transfer process depends on the crystal's gain and the intensity ratio between the two input beams. The gain, on its turn, depends on the crystal length and other geometrical parameters. To describe the carrier suppression process we use the following two experimentally convenient parameters: the intensity ratio between the plus and minus input ports, c, and the ratio between the power on the sidebands over the total power in the input minus port, the modulation depth m. We define the carrier suppression by the quantity S, the ratio of the power in the modulation sidebands to the power in the carrier at the output of the minus port.

The carrier suppression problem can be more easily visualized within the scope of the theory if we assume the electric fields for the different frequencies to be real, and represent them as vectors in a plus-minus plane as shown in Fig. 45(b). The carrier frequency is present on both input ports, plus and minus, and therefore is represented by a "carrier" vector $\vec{E}_c$ which lies somewhere in the middle of the plane; whereas, since the sidebands are only present in the minus port, they are all aligned with the minus axis, and can therefore be summed into one single "sideband" vector $\vec{E}_s$ representing all the sidebands.

One can show that the input system of vectors, corresponding to the various optical frequencies, can be represented by one single vector, the principal eigenvector $\vec{e}$.[12] The dynamics of the two-beam coupling interaction simply correspond, in this representation, to a rotation of this principal eigenvector. The amount of rotation depends on the photorefractive gain. It is important to note that, since all the fields in the crystal share the same grating, all the vectors rotate together—one can think of the eigenvector as "pulling" the other vectors with it. Notice, however, that as the eigenvector rotates towards the plus-axis, there will be a location where the projection of the carrier vector on the minus-axis is zero. This means that, for a gain value resulting on that particular rotation, there is no carrier present in the output minus-port, i.e., the carrier is suppressed.

To study the behavior of the carrier suppression S, we write it as a function of the above defined parameters c and m, and the gain z. From the above theory, one can show that it is given by

$$S(z) = \frac{m}{\sqrt{1-m} - \sqrt{c}\left[\arctan\left(e^{\Lambda z}\tan\theta(0)\right) - \theta(0)\right]},$$

where Λ is a parameter that depends on the vectors' initial configuration. For a specific value of the crystal's gain $z = L$, there exists a particular value of m for which the carrier is perfectly suppressed, i.e. $S \to \infty$. Figure 47 shows four different curves for S as a function of m. The peak for carrier suppression occurs at lower modulation depth for higher gain. To adjust the gain according to the signal's m, we propose an automatic-gain control on the IF amplifier stage. In addition, we find that, for fixed modulation depth, perfect carrier suppression requires the least

gain when $c = 1$.

6.3.2 The electro-optic phase modulator

The first step in designing a modulator is selecting an appropriate material that will fulfill the specifications, such as modulation efficiency. A magnesium-doped lithium niobate crystal (Mg:LiNbO3) resisted developing significant optical damage with up to a 500 W/cm^2 laser beam, which for our applications is considered high intensity, and is therefore an appropriate material for the phase modulator. Phase modulation was chosen due to its simplicity. It is interesting to note that once the carrier is suppressed, mixing will be required to recover the signal, regardless of it having been generated by phase or amplitude modulation. The new phase modulator contained a (45.0 x 1.5 x 1.5) mm^3 crystal and a resonant circuit mounted directly on the modulator. The resonance was tuned to 129 MHz and resulted in a modulation efficiency of 0.7 rad/V. The phase modulated output is composed of a superposition of components described by Bessel functions of the first kind, $J_0(\beta)$, $J_1(\beta)$, etc., where $J_1(\beta)$ is the component of interest containing the signal information and $J_0(\beta)$ is the carrier, which should be suppressed. Given its efficiency, the new modulator requires less than 3 V to be driven in the linear slope of $J_1(\beta)$. Additionally, the modulator mount was machined to be compatible with the new 1"-high optics.

6.3.3 The new carrier suppression system

Using the theoretical results from Section 6.3.1, we built a new carrier suppression system significantly more compact than the previous one to reduce instabilities. This system has only one channel since its purpose is to test how well the carrier suppression can perform. Figure 46 shows a schematic of the system. A polarizing beam splitter preceded by a half-wave plate splits the laser beam. We adjusted the splitting intensity ratio to $c = 1$, which, as mentioned in the theoretical results, minimized the gain necessary for peak carrier suppression. One of the beams then entered the electro-optic modulator and was modulated by a 129 MHz signal and proceeded to cross the other unmodulated beam inside a photorefractive barium-titanate crystal. The carrier and sideband peaks from the output of the crystal were measured using heterodyne detection. The part of the setup inside the dotted line is the heterodyne beam, which was shifted 80 MHz with respect to the optical carrier via an acousto-optic modulator. The modulator drive voltage was used to set the value of the modulation depth m.

The dotted curve in Fig. 48 shows the experimentally measured carrier suppression S as a function of m. The shape of the curve and the position of the peak agree well with the theoretical curve. The maximum observed value of S of about 40 dB is measurement limited. Another significant figure of merit is the reduction of the carrier peak on the output (minus port) as compared to the input, measured to be more than 60 dB. The measurement limit is due to a combination of detector noise and carrier feedthrough from the acousto-optic modulator.
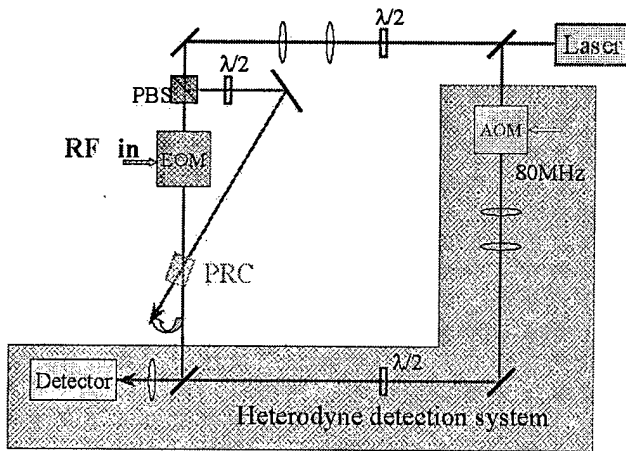
Figure 46: Setup for the carrier suppression test-system. The electrooptic modulator generates a phase-modulated signal. The signal beam crosses another unmodulated beam inside the photorefractive barium- titanate crystal. The energy transfer interaction suppresses the optical carrier. The beam, shown inside the blue box is shifted by 80MHz and is part of the heterodyne detection scheme.
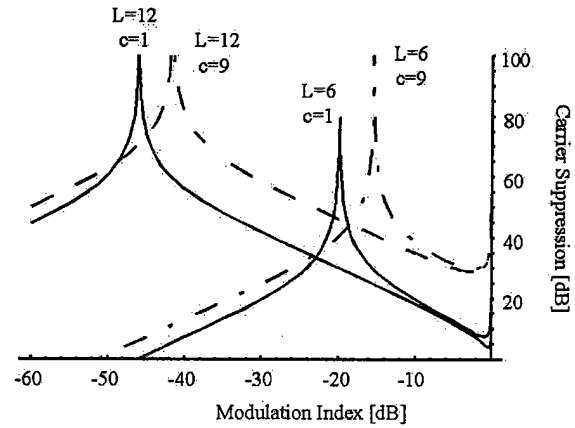

Figure 47: Carrier suppression as a function of modulation strength, for different combination of the input intensity ratio, c, and the gain, L.
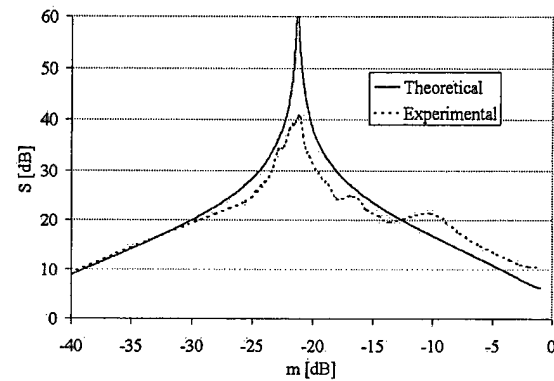
Figure 48: Theoretical and experimental curves of carrier suppression vs. modulation strength. The peak of the theoretical curve is infinite.

6.4   The auto-tuning filter

Last year we reported a 10x15 cm^2 filter using fiber optics interconnections and a novel spherical cut for the photorefractive crystals, which allowed us to reduce the size of the optical circuit. From the length of the optical loop we estimated the filter's bandwidth to be 300 MHz. The filter required a minimum input optical power of 50 mW. Input signals were generated with acousto-optic modulators to test the performance of the filter independently from the carrier suppression stage. We evaluated the performance of the auto-tuning filter by measuring how much it enhanced the difference in power between two input signals. Of particular interest is the worst case scenario for small input power differences. Two signals with a power ratio of 1 dB at the input, resulted in a power ratio of 8 dB at the output, yielding a contrast enhancement of 8 dB/dB for small input power differences. The goal of increasing the contrast enhancement, reducing the minimum input power requirements, and increasing the bandwidth, has spawned

two projects: one, the design and implementation of a new version of the auto-tuning filter, and two, the investigation of oscillation patterns within a single barium titanate spherical disks with a potential application for a future filter version. The two most salient features of the new filter design as compared to the previous version are the use of free-space technology and a novel crystal-cut. This features also made it possible to reduce the filter's size to a 2.5 cm diameter disk. The new, so-called, "gold-bar" shaped crystal-cut significantly increased the performance of the two-beam coupling interaction and reduced passive losses, as discussed in the next section. These gold-bar-shaped crystals are used in the new version of the filter, discussed in Section 6.4.2. As to the second project, the oscillation patterns inside a spherical disk are actually low-order optical whispering gallery modes,[13] observed for the first time in barium-titanate. Section 6.4.3 gives more details on this project.

6.4.1   A novel crystal cut

In the case of TBC with optical fibers, the use of photorefractive spherical disks provides the advantage of dispensing the lenses typically necessary for collimating and focusing the beams from and into optical fibers. However, for the free-space filter design, such an advantage no longer applies and we therefore switched back to using non-focusing rectangular crystals. We introduce a geometry that would reduce the losses in the filter. The high index of refraction of barium titanate ($n = 2.4$) resulted in a 17 % reflection-loss at an air/crystal interface. Additionally, and perhaps more seriously, "active" losses result from scattered-light reflections within the crystal which can decrease the two-beam coupling gain by partially erasing the grating. To reduce the passive reflection losses, the entrance and exit surfaces of the crystal were cut at Brewster's angle. In addition, the sides have been cut with a tilt such that scattered light will not be reflected back to the grating. In these gold-bar-shaped crystals, shown in Fig. 49, the resulting two-beam coupling gain is uncommonly high (up to 23 cm^{-1}) and the saturation is low (two equal intensity input beams result in a gain of 2).

6.4.2   The compact free-space auto-tuning filter

The new filter, measuring 2.5 cm in diameter, is shown in Figure 51(a). This filter uses the crystal-cut described in the section above. Competition for a finite photorefractive gain among the RF signals requires, amongst other considerations, a highly multi-mode oscillating pattern in the resonator. In the previous filter, a multi-mode fiber feedback loop ensured the multi-mode cavity mode. In this new filter version, although we no longer use fibers, the free-space multi-mode pattern of the oscillating beam is still possible due to the spatially broadband gain of the photorefractive crystals. Free space propagation of light yields two advantages. One, we are no longer constrained to a minimum radii of curvature for bending the fibers, so we can make the system smaller. Two, our linear input polarization is not scrambled upon propagating, which
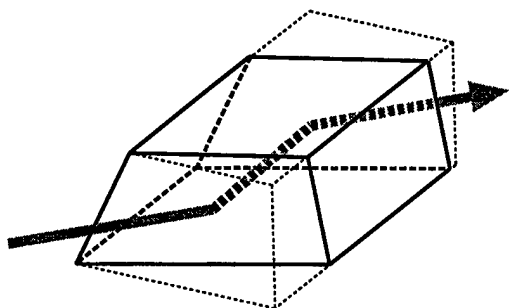
Figure 49: The input and output faces of the crystal are cut so that the incidence angle of the beam is at Brewster's angle, thus eliminating p-polarized reflections.
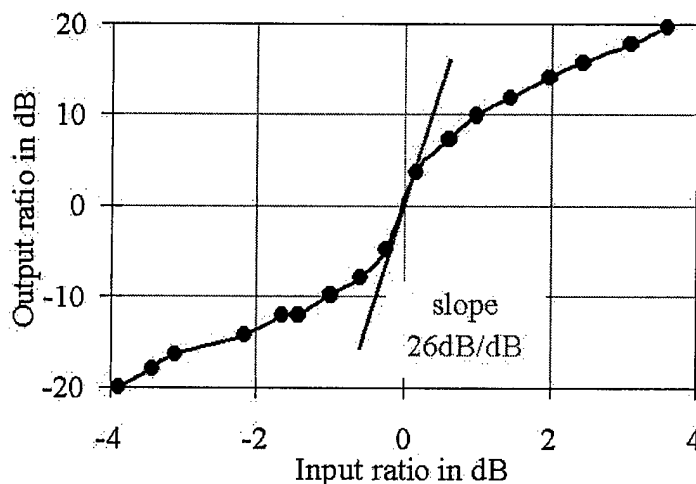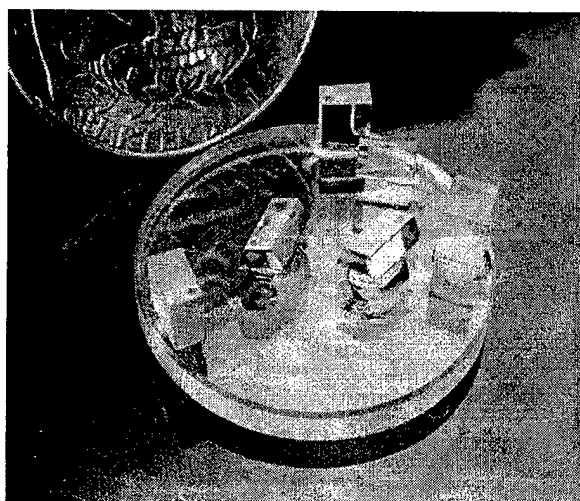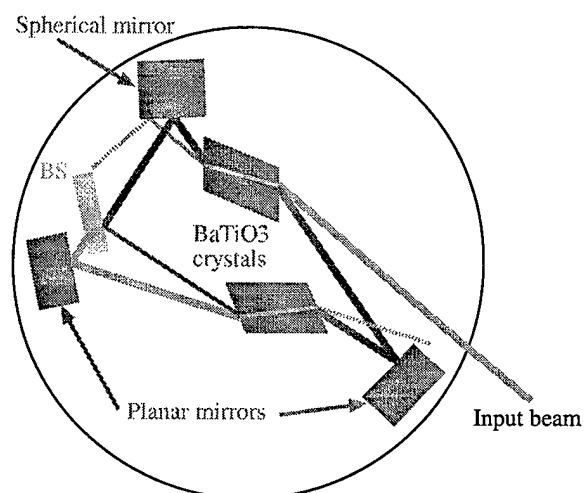

Figure 50: The performance of the filter is evaluated by how much an input signal ratio is enhanced at the output.

(a)

(b)

Figure 51: (a) Photograph of the auto-tuning filter, compared to a U.S. quarter. the substrate is glass is order to use the aligning template. (b)The template uses ray tracing to determine the orientation of the optical elements in order to obtain a loop path for the oscillator.

increases the filter's efficiency, since for barium titanate, only the parallel polarization effectively contributes for the photorefractive gain.

We developed a technique for aligning the optical elements by the use of templates, shown in Figure 51(b). We calculated the rays' path through the system's elements using the condition of a closed path for the oscillator. Such calculations yielded a template which was transferred to a glass substrate. The different optical elements were then aligned to the pattern in the substrate
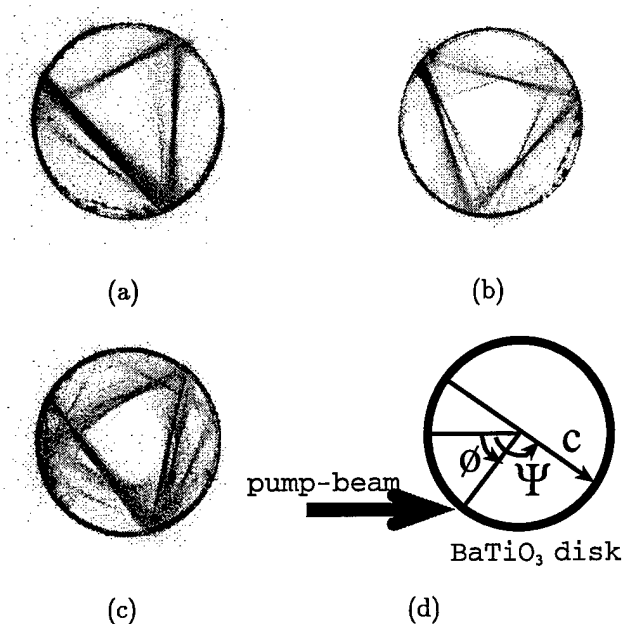
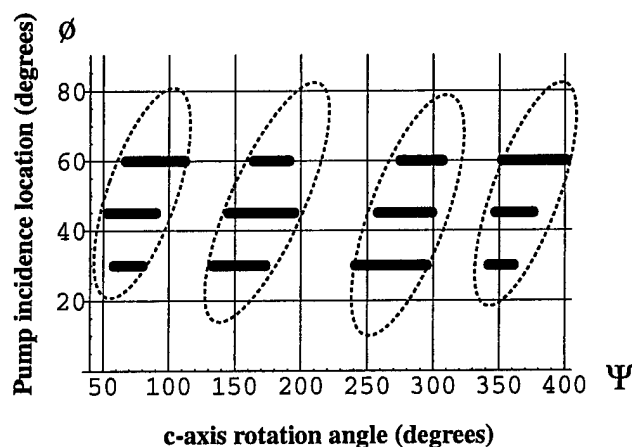Figure 52: (a) Picture with up-side-up and (b) up-side-down triangle and (c) square, (d) geometry.

Figure 53: Occurrence map of triangles

and finally fixed.

To evaluate the performance of the filter we used the same acousto-optic test bed used for the previous filter version (see Section 6.4 above). Figure 50 presents the power ratio between the two RF signals at the output versus the input. The slope at the origin of 26 dB/dB is more than three times the obtained in the previous system. The optical circuit is about 30 times smaller and requires less than 5 mW of input optical power. The bandwidth of the filter, extrapolated from the round-trip path length, should be 3 GHz.

6.4.3 The spherical disk

We have investigated interesting oscillation patterns that occur when a single Gaussian (free-space) pump beam is incident on the spherical disk. Figure 52 shows pictures of generated triangles and a square. The oscillating patterns are understood to be low-order whispering gallery modes which are generated by total internal reflection at the crystal's boundaries. They are excited via TBC interaction with the incident pump beam. Due to the high refractive index of barium titanate, total internal reflection occurs for angles greater or equal to about 24°, which allows triangles as the lowest-order oscillation mode (reflection angle for the triangle is 30°).

Figure 53 shows a measured occurrence map for triangles with respect to the incident pump displacement from the center (ϕ) and the orientation of the crystal axis (ψ). (Both angles are referenced to the line that crosses the center of the disk and is parallel to the external incident

pump.) We used TBC theory to predict the occurrence of four triangle regions. There are two geometrical positions inside the crystal that results in optimal inter-beam angle for the pumping of triangles. The first geometrical position, the "up-side-up" triangle (as in Fig. 52(a)), occurs with a vertex aligned with the pump input. The second, the "up-side-down" triangle (as in Fig. 52(b)), occurs with a vertex aligned with the first pump reflection. The TBC theory also predicts two maxima in the pumping gain with respect to the crystal axis orientation ψ for each of the two up-side-up and up-side-down triangles, totaling four occurrence regions.

Higher order patterns experience decreasingly less gain and therefore become increasingly more difficult to observe. Hexagons were the highest order observed. David stars (two triangles shifted by 60°) were also observed. To determine whether the oscillating patterns are uni- or bi-directional, we looked for a counter-propagating phase-conjugated pump beam which, in the case of bi-directional oscillation, would be generated by four-wave mixing. The absence of a phase-conjugated pump suggests that the patterns are unidirectional oscillations, therefore carrying the possibility of using these patterns for future ring circuits such as the auto-tuning filter.

6.5 Future work

In the near future, our main targets are to integrate our whole system and to increase the wall plug efficiency. Reducing the dimensions down to a portable size implies making the parts smaller and the system more robust. In addition, we intend to design and build a multi-channel EOM which will require only one crystal for the two channels. Improving the wall plug efficiency mainly consists of bringing down the minimum optical power needed by the auto-tuning filter and by enhancing the electro-optic modulation efficiency. The former has already been achieved with 5 mW of optical power necessary to operate the filter. The latter will involve using a thinner crystal and improving the resonant impedance matching circuit. Longer term goals include increasing the number of channels (i.e. the number of active receivers) as well as the RF bandwidth of the system. Most of the effort will be directed towards modifying the EOM in order to meet our objectives.

6.6 Progress

Our goals were to produce a compact optical processor (the auto-tuning filter) for RF signals, and to continue to reduce the size of the processor in order to increase the processing bandwidth. Part of the optical processor is a carrier suppression system that eliminates the optical carrier from output of an electro-optic modulator. A surprising result from our design calculations shows that our photorefractive system can theoretically perform perfect suppression under certain conditions. Our experimental results achieved 65 dB of suppression, which is better than any published data of which we are aware. In particular, 30 dB suppression is normally considered

very good performance.

The next generation of auto-tuning filter that we produced this past year provided much more than simply bandwidth improvements. We measure a four-fold improvement in the signal contrast enhancement relative to previous version. We believe that part of the improvement was due to a new photorefractive crystal prism geometry that avoids various parasitic effects of beam fanning by eliminating internal feedback paths.

6.6.1   Plans for year 4

Our plan is to integrate the entire RF optical system from the antenna receiver array to the output of the optical processor, including the laser, into a single, portable system. We intend to assess the signal extraction performance of the system using a pair of uncorrelated transmitters. From there we intend to increase the number of RF channels processed by the optical system to seven, and to increase the bandwidth of the EO modulator to 0.5 GHz. We have begun the development of a multi-electrode electro-optic modulator that can impose all the RF signals from a multi-element antenna array simultaneously. The reduction of crosstalk between electrodes is a primary design issue.

6.6.2   Plans for year 5

We plan to include feedback from the optical processor to the RF front-end to increase dynamic range and establish a signal tracking capability for the optical system. We also intend to develop a more complex optical system capable of super-resolution, so that the signals from two sources too close to be resolved by the antenna, can nevertheless be separated. The design will require the development of improved numerical techniques for photorefractive optical circuit calculations.   .

7 An Optically-Switched Transmit/Receive Active Antenna Array

Principal Investigator: Zoya Popović, University of Colorado, Dept of ECE

A possible realization of multiple-beam arrays are active antenna array lenses (AAAL) with spatial feeds.[14,15] Some properties of this architecture are: phase-shifterless beam forming; lower feed losses than those associated with corporate feeds for large number of array elements; improved dynamic range in reception; high EIRPs in transmission; and graceful degradation in both transmit and receive modes.[16,17] As part of this project, we have been developing designs for half-duplex operation using microwave SPDT switches to route the transmitted and received signals. **Our goal has been to show that very large arrays can be switched between transmit (T) and receive (R) at nanosecond speeds and with low switching energy, using optical control of the microwave switches.**

Figure 54 shows an example of a cylindrical active lens with half-duplex operation. A brief description review of the main features of such an array are as follows. Each array element contains two antennas (shown here as patch antennas on each side of the lens), a power amplifier (PA), a low noise amplifier (LNA), and two SPDT switches. In transmission mode, the patch antennas on the feed side receive signals from one or more feed antennas (represented by horn antenna in the figure) located along the focal arc of the lens. In each element, the signal is delayed in relation to their position in the array: unit cells in the center have longer delays than edge elements, in analogy to an optical lens being thicker in the center than on the edges. The switches then route the signals through PAs before re-transmitting a coherent combination of all the element powers. In reception, the signals are routed through LNAs in each element. Different positions of a feed along the focal arc correspond to different main beam angles. In addition, for linear amplifiers in the lens, several feeds can be used simultaneously for beam forming.

In half-duplex T/R lens arrays demonstrated to date, the switches are controlled in parallel and the bias and control lines contain capacitors that suppress bias-line oscillations.[16,17] As a result, the rise and fall times of the array when it is switched between T and R increase with the number of array elements. Individual control of each element, however, increases the complexity of the control lines and the cost. A possible solution is to optically control switches in each unit cell of an array. In this case, the switching speed of the array is independent of its size and equal to the switching speed of each element. Further, optical fibers that guide the switching control signals do not affect the microwave fields.

Previously demonstrated optically controlled microwave switches use optical power to generate carriers in microwave *pin* diodes.[18–20] The disadvantage to this technique is the fact that the insertion loss (IL) and isolation of the switch depend strongly on optical power, and as much as 40 mW of optical power can be required to achieve an IL of 1.2 dB and an isolation of 30 dB.[20]
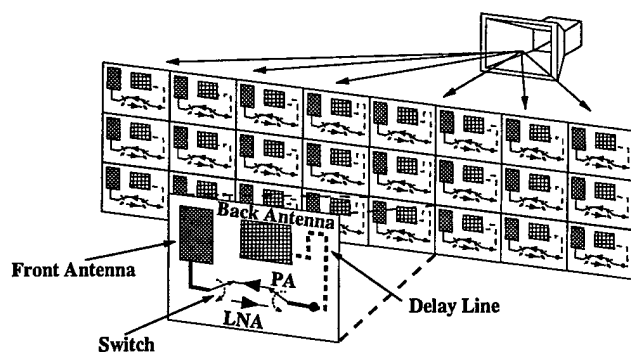
Figure 54: Sketch of a cylindrical T/R active antenna lens array with half-duplex operation. Insert shows details of the array element (unit cell).
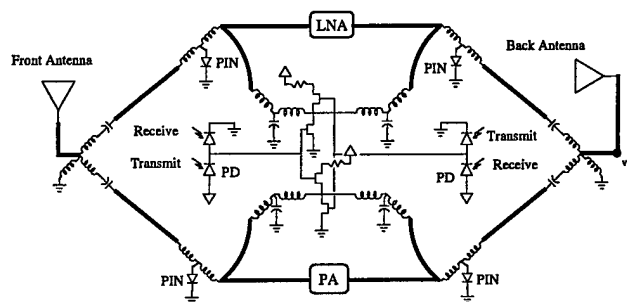

Figure 55: Circuit diagram of the active antenna element. The light incident on the PDs controls the *pin* diode SPDT switch through push-pull FETs. The switches route the signal between the two antennas a PA in transmission and LNA in reception.

The optically controlled microwave switch that we developed uses a small amount of optical power to control the bias of chip *pin* diodes. The advantage of this technique is that only the switching speed (rise and fall times) is a function of incident optical power, while the IL and isolation are independent of it. Our approach is to use off-the-shelf microwave and optical components in a low-cost circuit designed to be optimized for both RF and optical performance.

7.1 Design and Layout of Microwave Switch Circuit

Figure 55 shows the schematic of the array element used in this work. 10 GHz patch antennas with a common ground plane and vias between the two sides of the active antenna are used to improve isolation between in the input and output of the amplifiers. Off-the-shelf MMIC amplifiers are used for the PA (HP HMMC-5618, 14 dB gain from 6 GHz to 20 GHz with 18 dBm power at the 1 dB compression point) and LNA (United Monolithic Semiconductor CHA2063, 16 dB gain from 8 GHz to 13 GHz with a noise figure of 2 dB). MA/Comm MA4GP032 *pin* diodes, with a 3 Ω on-resistance at 3 mA and 0.12 pF capacitance in the off state are used for the microwave switch. 25 μm diameter and 0.5 mm long gold bond wires are used as 1 nH inductors in a T network with the *pin* diodes to improve performance by reactance cancellation. The resulting single-pole single throw (SPST) switch has a measured IL of 0.75 dB and an isolation of 20 dB from 6 GHz to 13 GHz.

Compact high-pass (HPF) and low-pass filters (LPF) are needed to separate the bias/control and RF signals. In the unit cell, a second order HPF isolates the bias control for each side of the SPDT switch. This filter exhibits at least 20 dB rejection below 1 GHz and 0.1 dB loss at 10 GHz, and is implemented with a 2 nH shunt bond wire and a 1 pF chip capacitor at 10 GHz. An additional bond wire is needed to connect the chip capacitor to the microstrip line
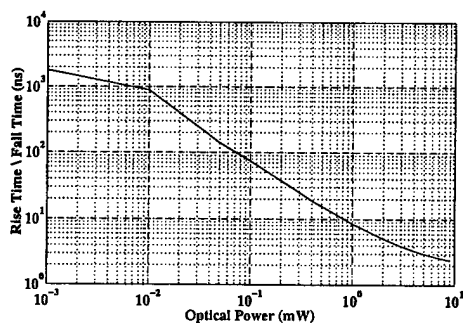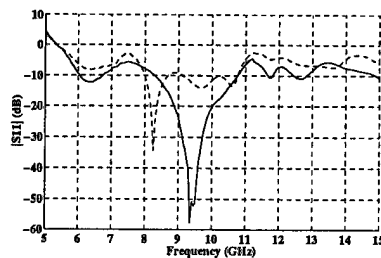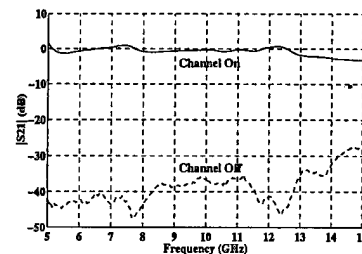
Figure 56: SPICE simulation of rise and fall times of the optically- controlled microwave switch as a function of optical power per photodiode.

(a)

(b)

Figure 57: Measured performance of the SPDT microwave switch: return loss (a); and (b) isertion loss and isolation.

and is designed to be resonant with the capacitor at 10 GHz. A third order LPF biases the *pin* diodes implemented with 0.85 nH bond wires and 3 pF capacitors. The low impedance of this combination is transformed into a high impedance with a λg/4 long microstrip line causing a 0.1 dB transmission loss at the bias line junction and 33.9 dB bias line RF leakage.

The switch circuit was designed to be extremely compact, having in mind its inclusion in a unit cell of an antenna array with a half-wave period. Note that most of the circuit elements are implemented with lumped bond wires and capacitors, also enabling broadband operation.

7.2 Design and Measurements of Optically Controlled RF Switch

The optically-controlled bias to the *pin* diodes is implemented with a HP ATF26836 general purpose MESFET (9 dB gain, f_T=16 GHz, C_{gs}=2.2 pF) and Fermionics FD80S3 1300 nm photo-diodes (PD) (0.95 A/W responsivity, active area 80 μm diameter, $C_j = 0.12$ pF). The MESFETs are used to sink and source the current of the *pin* diodes, allowing for small on/off response times. Push-pull PDs controls the gate bias point for the MESFETs. The switch is supplied from the MMICs bias line through a current limiting resistor, eliminating the need for extra bias lines.

The MESFET gate capacitance and PD on-resistance dominate the rise and fall times of the bias control circuit. Figure 56 shows SPICE simulation results for rise and fall time as a function of optical power per PD. The SPICE models for each component are based on physical measurements. It can be seen that the fastest expected response for the back-to-back SPDT switches is 2.4 ns at 9 mW per PD, and is determined by the RC time constant resulting from the two *pin* diode junction capacitance in parallel and the current-limiting resistor. Faster rise time may be achieved by reducing the impedance of the current limiting resistor at the cost of increased *pin* diode current or providing a separate supply bias line for the switch. For only 1 μW of incident optical power, the switch rise (and fall) time is approximately 1700 ns.
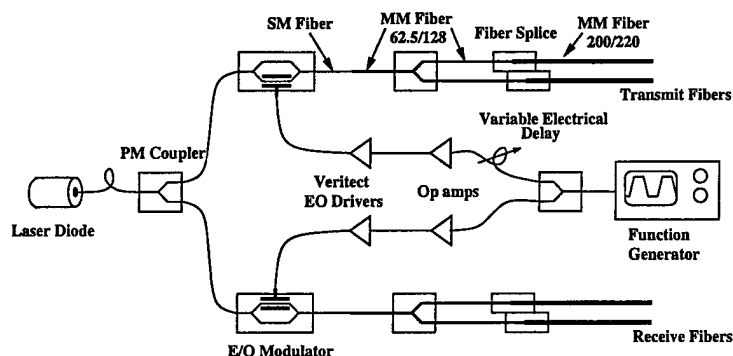
Figure 58: Block diagram of test setup used to character-
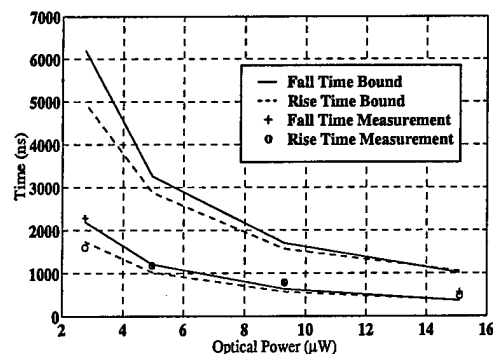ized the optical control circuit.

Figure 59: Measured back-to-back
SPDT switch rise time and fall time as
a function of incident optical power.

The measured SPDT switch in the active antenna element has an IL of 0.31 dB and an
isolation of 36 dB over a 2.5 GHz with 2:1 VSWR bandwidth (8.36 GHz to 10.8 GHz), Fig. 57(a).
From the SPICE simulations, 90 % of the spectral energy for the switching currents is below
700 MHz, allowing the removal of the shunt inductor in the HPF to improve the reflection loss.
The series capacitor in HPF reduces the *pin* diode switching voltage by 10 dB, which is sufficient
to prevent the other *pin* diode form turning on. 0.25 μW of optical power/diode maintains the
switch state. Therefore, the optical power from Figure 56 is required only during the period of
time in which the switch is changing state.

For testing the optical switching rise and fall times, variable length complimentary optical
pulses with fast edges were needed. Two 3 GHz Uni-Phase intensity electro-optic (EO) modu-
lators were used to generate the optical pulses. They were controlled by a function generator,
inverting/non-inverting op-amps, and two Veritect EO drivers. An Ortel 10 mW 1300 nm fiber-
pigtailed laser diode was the optical source, shown in Figure 58. The resulting optical pulses
were 25 ns to 7000 ns with constant rise (fall) time of about 1 ns. The single mode (SM) fiber
outputs of the EO modulators were coupled to a 62.5/128 μm multi-mode (MM) fiber splitter,
and then spliced to 200/220 μm fibers for easier free-space alignment to the PDs. Baffles between
the optical fibers and the PDs prevented cross-coupling between the transmit and receive optical
control signals. The loss due to the free space coupling of the fibers to the PDs limited the
testing range of the switch from 3 μW to 15 μW of optical power per diode, but this is not a
fundamental limitation.

Two back-to-back optically controlled microwave switches were constructed to test the switch
response of the active antenna element. In these measurements, an HP 83620 sweeper was
connected in place of the patch antenna, and an HP 54750 50 GHz oscilloscope in place of the
MMIC amplifiers. The oscilloscope measured the change of the *pin* diodes bias; however, the
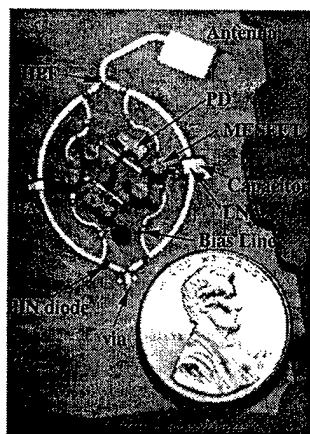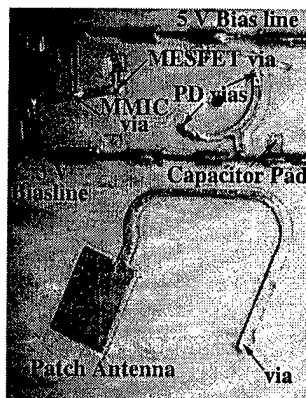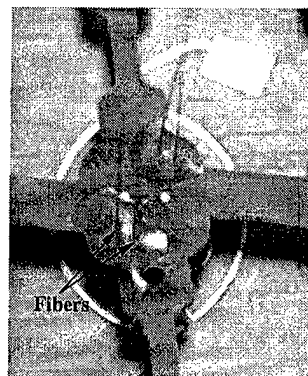
(a)   (b)

Figure 60: Photographs of the antenna element without the fiber optic mount: The active circuit side layout (a); and (b) the passive side layout.

(a)   (b)

Figure 61: Photographs of optical fiber mount: (a) the top of the optical fibers mount; and (b) the bottom of the optical fibers mount with the 1.5 mm baffle holes.

bias circuitry was loaded, resulting in a slower response. The SPICE model was modified to include the effects of the oscilloscope, as well as the uncertainty in optical power delivered to the PDs (+1.7 dB and -2.7 dB).

Figure 59 shows a comparison of the simulations with measurements, which fall within the modeled bounds. In the active antenna, the switching should be faster, since measurements of the MMICs using a network analyzer indicate a nearly perfect reflection (-0.6 dB) at each port for frequencies below 700 MHz.

7.3   Active Optically-Controlled T/R Array Element

The active circuit side of the antenna element, Figure 60(a), contains the two SPDT switches, LNA, PA, and patch antenna. The push-pull MESFETs and PDs were packed into the center of the circuit with the 50 Ω microstrip lines of SPDT switch encircling them. 30 dB isolation was maintained between any two elements that carry the 10 GHz signal, in order to prevent oscillations.

The 5 V and -2.3 V supply bias lines are on the passive side of the active antenna element, Figure 60(b). The bias lines consisted of sections of high and low impedance λg/4 microstrip lines to prevent propagation of the 10 GHz signal. A 22 AWG wire was soldered down the center of the bias line to reduce the DC impedance with a reduction of 0.5 dB in filtering performance at 10 GHz. The overall bias line suppression is -7.1 dB/λg. 100 pF chip capacitors on the active circuit side decoupled the MMIC amplifiers from the 5 V supply bias line.

An optical mount shown in Fig. 61 aligned the optical fibers to the PD, while protecting

the circuit bond wires. Free space coupling from the fibers to the PDs allowed access to the microwave circuit during testing. The optical mount used five posts (one in the middle and four in each corner) to achieve a placement accuracy of 40 μm. Unfortunately, the overall alignment of the fibers to the PDs was 200 μm, limited by the packaging of the commercial PDs. The optical fiber was placed approximately 1 mm above the PDs, allowing natural diffraction of the light to cover the area where the PD was mostly likely to be. This resulted in an approximately 15.7 dB loss in optical power. The patch antenna radiated through a 20 mm by 20 mm aperture in the FR4 mount which had measurable effects on the RF active antenna.

The active T/R antenna was characterized with respect to an aperture of the same electrical size (0.75 λ_0 by 1 λ_0). First the aperture, and then the active antenna, were placed between two orthogonally polarized antennas connected to the ports of an HP70820A Transition Analyzer. The gain over the power transmitted through the aperture was measured for the active antenna for both T and R paths, with the amplifiers on and off. The gains of the PA and LNA were then estimated within a 2 dB accuracy from the active antenna gain and by using the Friis transmission formula. The losses due to the aperture efficiency of the antennas, the via holes and the switch insertion loss were taken into account, yielding gains of 14 dB and 16 dB contributed by the PA and LNA, respectively. These gain levels are in agreement with the manufacturer's specifications for the MMICs. The bandwidth of the gain in transmit and receive modes was dictated by the patch antenna bandwidth (a few %), whereas the switch itself was broadband. The isolation was measured to be 30 dB or more for cases when: the active antenna was in receive mode while transmitting; the active antenna was in transmit mode while receiving and when the active antenna was in the off state. These measurements were limited by edge diffraction and feed cross-polarization quality.

7.4 Optically-Switched Active Lens Array

Using the array element described in detail in the previous sections, a cylindrical lens as shown in Fig. 54 was designed with an F/D=1, with 24 elements. A photograph of the lens is shown in Fig. 62, and a photograph of the fiber mount for all of the switch control signals in Fig. 63. When the mount was aligned with the PDs in the array, either the path with the PA or the path with the LNA was on. Because of poor alignment of the PD chips in the commercial PDs, not all of the switches were fully on. The result was that the unit cells corresponding to these switches contained a loop with high loop gain (PA plus LNA gain), and therefore broke into oscillation. These oscillations were outside of the design bandwidth of the T/R array and are interesting to observe. They did not affect appreciably the performance of the overall array within the operational bandwidth. We are currently working on improving the illumination of the PDs in the array to ensure all switches are in the proper state when illuminated. The approaches we are taking are: using more optical power, bundling the fibers for better uniformity, and looking into
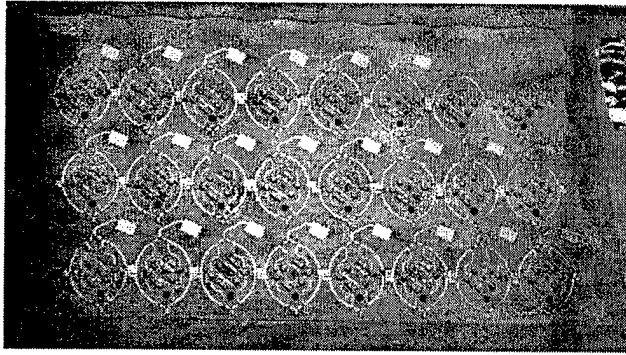
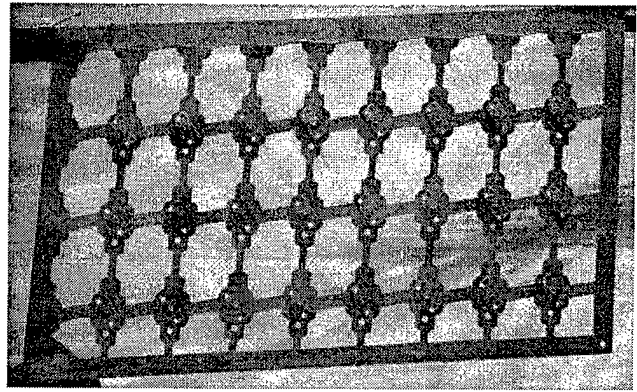Figure 62: Photograph of 24-element cylindrical T/R lens array.

Figure 63: Photograph of the optical fiber mount for routing control signals to the 24 antenna elements containing 48 SPDT switches.

planar integrated optical waveguides that could replace the fiber bundle.

The radiation pattern of a passive array identical to the active one, but with through lines instead of the MMICs, was measured with the fiber bundle present and compared to the pattern of the array with no fiber control lines. Even at the scan angle directly through the fiber bundle, there was not noticeable change in the pattern, confirming that the optical control lines did not interfere with microwave performance. Full characterization of the array is in progress (awaiting completion of a new improved anechoic chamber currently under construction in the Active Antenna Array Lab (AAA Lab) at CU).

7.5 Discussion

In this report, we describe the design and demonstration of a high-speed optically controlled T/R active antenna. This active antenna was designed as an element of a 6 λ_0 by 3 λ_0 cylindrical active lens array with a focal distance to diameter (F/D) ratio of 1, a directivity of 20 dB and a 10-degree beamwidth in the focusing plane. The lens array implemented beam switching and forming in both transmit and receive modes and its performance, as applied to radar and communication systems, is currently being characterized.

The optically controlled SPDT switches used to route the signal in the active antenna have 0.31 dB insertion loss, 36 dB isolation and -10 dB return loss from 8.36 to 10.8 GHz. Unlike in previously-demonstrated optically-controlled microwave switches, these microwave parameters do not change with the amount of incident control (optical) power. However, the optical power level conveniently controls the switching speed alone, making the switch easily integrated into applications with different switching speed requirements. Microsecond switching required in most T/R applications can be accomplished with only milliwatts of optical power, but some applications, such as phase shifters in phased array or polarization switching in multipath environments

could benefit from nanosecond switching speeds. Even though the 2.6 ns speed demonstrated in this report requires relatively large optical power (about 10 mW), the optical energy is quite low, 21 pJ. For comparison, the fastest reported MEMS microwave switch has a rise time of about 1 μs to 5 μs and requires about 2 nJ of control energy.[21,22] The switch presented here drew more electrical power (3 mA per *pin* diode) than a MEMS switch, but the required DC current is a small fraction of the 160 mA drawn by the LNA and PA. However, the optically controlled microwave switch required significantly less control energy than a MEMS switch, since the energy distribution is fundamentally different. In some respects, it is easier to generate fast optical pulses than to generate fast high voltage (30 V - 50 V) electrical pulses.

The active array element was designed with off the shelf components not optimized for speed or low power, and the coupling of light from the fibers was not optimal. Therefore, the presented results are by no means fundamentally limited and we expect that significant improvements can be made by using PDs with better placement tolerances, using chip MESFETs for the *pin* diode bias control and by improving the coupling efficiency of the light into the PD (using, e.g. microlenses and printed optical waveguide structures). Ultimately, a large portion of the switch, and in principle the entire switch circuit, could be implemented monolithically.

7.6 Progress in Quasi-optical Antennas

Progress as compared to the original statement of work are elucidated below.

1. We will design, fabricate, and characterize an X or Ku-band hybrid lens amplifier array with 50 to 100 elements and an F/# between 1 and 2. The design will optimize the type of antenna elements, the array topology, the type of substrate and active devices, and the compatibility with available EO modulators. The design will evolve as new photonic components are developed by the MURI team and inserted into the RF front end.

   - We have designed several X-band lens amplifiers with up to 49 elements with tight focusing (F#s between 0.6 and 1). The lenses were designed to be compatible with any EO modulator that can be connected to a 50-Ω transmission line. In specific, the following two lenses were tested with photonic components included:

     – a 49-element patch antenna lens with F/D=0.6 with up to 7 receivers placed along the focal arc. Currently, two of the receivers are connected to a multi-channel EO modulator (100 MHz IF). This is a receiving front end only and interfaces with Prof. Anderson's optical processor.

     – a 28-element cylindrical lens array antenna using patch antenna elements with transmit (T) and receive (R) amplifiers integrated with each element. The 10-GHz signal is routed between T and R paths through two optically-controlled

RF SPDT switches integrated in each unit cell of the array and activated with multimode fibers.

2. After the antenna array is completed, high-performance EO modulators will be designed. The EO modulators will need to receive the power-combined signal from free space. We will investigate lithium niobate antenna modulators, as well as the possibility of using quantum-well modulators. The latter type lends itself more naturally to a non-guided RF signal incident from free space. In the lithium-niobate modulators, the type of antenna used to detect the RF signal will determine to some degree the necessary RF power for a required EO voltage, and we will investigate different receiving antennas with power minimization in mind.

- We have designed some narrowband high-efficiency EO modulators, since the signals we currently have are limited to bandwidths of hundreds of megahertz. The unique feature of our LiNbO3 modulator is that it is a multi-channel device. This means that we only need one modulator with as many electrodes as there are receiver elements, reducing the cost of the EO portion of the array. Currently, we need -5 dBm of RF power into a 30-dB driver for a 50-Ω modulator to get 100 % phase modulation. The design involved: electrode design on lithium niobate, impedance matching for a low V_π to a 50-Ω driver amplifier, understanding of the mutual coupling between modulator electrodes, equalization of the two channels in the receiver stage, and designing of a optical line generator and crystal cut for efficient coupling of the optical carrier into the modulator.

3. In this design, there will be several EO modulators located at the focal arc of a receiving lens amplifier array. The EO devices will couple at RF frequencies and the coupling will determine the number of independent beams that can be received. In this phase, mutual interactions will be investigated and quantified, as they will affect the antenna impedances, and therefore the RF signal incident on the photonic devices.

- As we designed a single, multi-electrode modulator, the mutual coupling between receiving antennas is not the only concern, but the coupling between the modulator electrodes also becomes a concern. We have quantified both of the coupling mechanisms and have come up with ways to minimize and control the coupling:

  - the mutual coupling between receive antennas was measured for incident signal arrive angles between -90 and +90 degrees. The measurements agree with predictions for patch antenna and small E-plane horn receivers.

– the coupling between the several channels within the modulator is minimized using techniques borrowed from VLSI circuit design, as well as using resonant coupling.

4. Optically-controlled RF frequency-selective surfaces (FSSs) will be developed and demonstrated using commercial optical detectors or ones donated by our industrial supporters (Hughes). We will demonstrate an optically controlled 1-Gb RF switch at X or Ku band as a proof of concept. We will also demonstrate a high-speed optically controlled digital phase modulator (BPSK) that can be cascaded with a quasi-optical transmitter for external modulation.

- We have demonstrated the fastest, lowest power optically controlled X-band switch. The switch has excellent microwave properties: 0.3 dB loss, good input match and 36 dB isolation over several gigahertz bandwidth. The optical power only controls the speed of the switch and we have demonstrated 2 ns switching speeds (order of gigahertz) with milliwatts of optical power and about 10 pJ of optical energy.

- We did not demonstrate a FSS, but instead a T/R active antenna. The FSS was not needed for any of the other parts of the project. However, the switch is the main element that needed to be developed, and it would be an easy task to design an optically-controlled FSS with a desired frequency response.

- We have demonstrated an electrically controlled BPSK modulator; with the developed switch it is again, a simple matter to redesign it so that it is optically controlled, but it did not seem to us that the overall RF-photonic project would benefit from spending the time to do this. Instead, we decided that it would be much more beneficial to work on integration of an entire front end, focusing on both transmit and receive portions of an optically controlled active array (a much desired one).

Key additional progress beyond that originally envisioned in the statement of work includes substantial efforts in the following areas:

1. Complete T/R QO front end with optical control.

2. Integration of a QO front end with an operating photorefractive optical processor for signal extraction (with Prof. Anderson).

3. Investigation of adaptive algorithms as applied to a lens array (with Prof. Griffiths).

7.6.1 Plans for Years 4 and 5

1. Continue working on the front end portion of arrays with optical processing to include feedback from the optical output to the RF front end. For example, after optical processing,

resource allocation can be done at the front end using appropriate feedback, making the system more efficient.

2. Apply some quasi-optical techniques developed under this project to systems other than radar. In particular, we are interested in passive millimeter-wave ranging arrays that use QO lens antennas.

8 High Speed Polymeric Modulators for Photonic Array Antenna

Principal Investigator: A. Knoesen, Department of Electrical and Computer Engineering, University of California, Davis, CA 95616.

This project was incorporated within the MURI in April 1999 as a collaboration between Prof. Knoesen of UC Davis and Ted Weverka of Photonic Data Systems. During the December 1999 Review, when it was announced that Weverka will be leaving the MURI in January 2000, the MURI technical advisory board recommended broadening the scope from the existing strict focus on only broadband inline fiber modulators to activities that include

1. Free-space microwave polymer analog modulators: Expand the polymer thin film modulator concept towards a device suitable for free-space optical interconnect modulator arrays that could operate in the microwave regime.

2. Resonant analog polymer modulators: While the previous activities focused on very wideband modulators, investigate narrower band resonator modulators that make use of thin film electro-optic polymers.

3. Polymer inline fiber modulators: Continue the work to improve the modulation efficiency.

Free-space modulation is achieved by reflecting the optical beam off a Fabry-Perot electro-optic modulator. We have designed, fabricated and characterized a Fabry-Perot reflecting structure, which uses a thin electro-optic polymer, to modulate an optical beam at microwave frequencies. We demonstrated modulation in excess of 5 GHz.

We investigated thin film microwave resonators that can be implemented with fabrication techniques consistent with electro-optic thin film polymer modulators. The low dielectric constant of polymers in combination with the losses in thin conducting films limits the Q. We have implemented a series LC resonant structure on a polymer thin film with a resonance at 4 GHz.

The inline fiber modulator has several unique attributes compared to conventional fiber optic modulators, such as the spurious free dynamic range and a mechanically robust configuration. However, the modulation efficiency demonstrated to date is too low. The challenge is to increase the modulation efficiency to at least the 5 % and 5 V modulation range. Towards this objective, we improved the current understanding of electromagnetic fundamentals present in these devices. Our investigation made clear the need for an electrical conducting layer with lower optical loss in the 1300 nm range, and we identified such a conducting polymer. We initiated a collaboration with Prof. Dalton's group at USC and are integrating a high r-coefficient polymer into the inline modulator. Finally, we have developed micro-machined fabrication techniques for rapid prototyping of inline modulators which integrate new materials into thin film structures with well-defined microwave and optical characteristics.
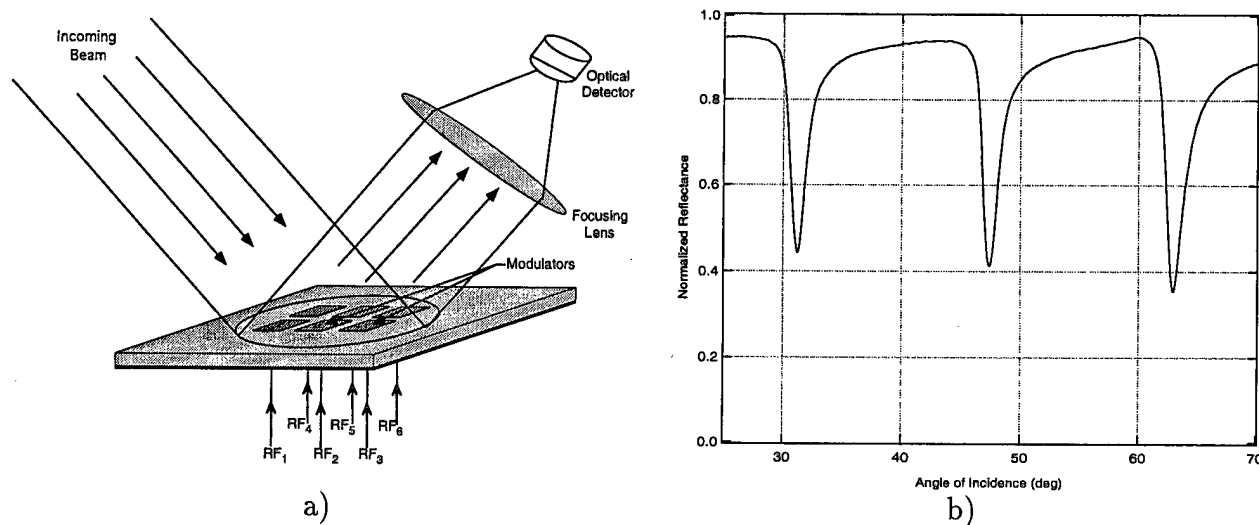
Figure 64: (a) Free space optical interconnect arrays. (b) Reflectance of the Fabry-Perot resonator as a function of the angle of incidence.

8.1 Free Space Microwave Polymer Analog Modulators

While optical fiber is an attractive means for transporting modulated optical carriers, connecting large arrays of electro-optic modulators to individual optical fibers is problematic. Free-space optical interconnect architectures, such as the one shown in Figure 64a, provide an elegant solution to this problem. An important component is a free-space modulator that can be modulated at microwave frequencies. The immediate objective of this research is to investigate and demonstrate the feasibility of a reflective analog modulator that operates in excess of 1 GHz using electro-optic polymers.

8.1.1 Reflection Fabry-Perot Polymeric Modulator (RFPPM)

In 1994 UC Davis reported on lumped-capacitor free-space polymer modulators with a bandwidth of 100 MHz.[23] In this research, we extend the concept to devices that operate in the microwave regime. We have implemented a RFPPM that consists of a partially reflecting gold layer, an electro-optic polymer, and a highly reflecting bottom layer. The structures are designed to be an asymmetric Fabry-Perot cavity at a specific angle of incidence. The dimensions of the polymer modulator are compatible with microwave electronics driving an array of modulators.

8.1.2 Fabrication of the RFPPM

Optically, the modulator is a Fabry-Perot cavity while electrically, it is a parallel plate capacitor. The size of the modulator is determined by meeting both microwave and optical requirements. The electro-optic polymer has a low dielectric constant which results in high speed modulators with dimensions that are not so small as to complicate optical alignment, but small
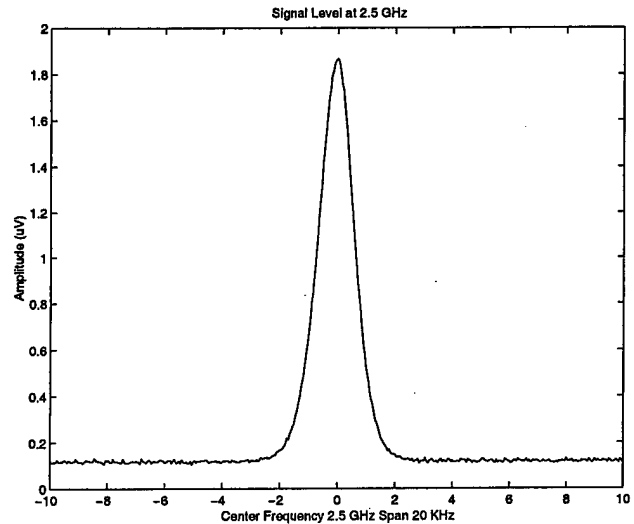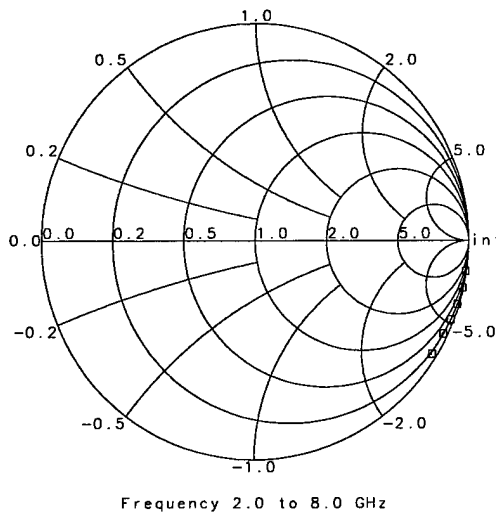
Figure 65: (a) Smith chart plot of the capacitor used in the modulator. (b) Received signal spectrum for the detected signal from RFPPM at 2.5 GHz.

enough that large array densities can be achieved. An analog modulator which performs well at high frequencies (≥ 1 GHz) must have a low capacitance, which implies a small surface area. However, from optical considerations the device area should not be so small that alignment becomes impractical. As a compromise, we chose a 140 μm square for the prototype demonstration. The thickness of the polymer was determined by the angle of incidence and wavelength where the device had to be optically resonant. Typical film thickness are on the order of 6 μm. The reflectance of the Fabry-Perot resonator as a function of the angle of incidence for the test sample is shown in Fig. 64b. The devices were designed to be modulated at an angle of incidence of approximately 47° which corresponds to a dip in the reflectance at 1064 nm. At this angle of incidence, a small change in index of refraction of the polymer layer produces large changes in optical reflectance.

The multi-layer structure consists of a bottom optically-thick gold electrode, a corona-poled electro-optic polymer layer, and an upper partially transmitting thin top gold electrode. The two electrodes are thermally evaporated. The electro-optic polymer was adhered onto the surface using the lift-off polymer deposition technique.[24] Laser ablation was used to make a capacitor.

8.1.3 Microwave Characterization

The lumped capacitor of the RFPPM set the high frequency limit of the modulator. A vector network analyzer was used to measure S_{11}. A Smith chart plot of the S_{11} measurement shown in Fig. 65a confirms that the structure behaved well as a capacitor to frequencies well above 5 GHz.

8.1.4 Microwave Electro-optic Testing

A pair of optical beam probes, which consist of optical fiber with integrated GRIN lenses, are used to launch and collect the light. The optical source is a 1064 nm diode pumped laser. A microwave signal is applied across the capacitor using a coplanar waveguide probe, and the detected signal is measured by a spectrum analyzer. Polarizing loops in the optical path allow adjustment of the polarization to optimize the received signal. A graph of received signal strength is shown in Figure 65b. The optical signal was detected by a high speed detector with 25 GHz of bandwidth. The RFPPM has a 5 GHz optical half power modulation bandwidth.

8.1.5 Future Work

The future work should expand the concept to an array of modulators. It will be essential to ensure that uniformity of the structures can be maintained over large areas. During the initial experiments non-uniformity was observed and is attributed to either non-uniform thickness or poling. A determination of the optimum size and shape of both the optical beam and the modulator will be investigated. A system level study is needed, that accounts for the small modulation efficiencies achievable in the polymer arrays, so the technological gains provided by the free-space microwave analog modulated arrays can be determined.

8.2 Electrically Resonant Thin Film In-line Fiber Modulators

In RF-photonic systems that do not require a bandwidth that extends from DC to microwave, trading bandwidth for modulation efficiency is attractive since electrical resonance can be used to greatly increase the voltage applied to a modulator across the capacitor. The objective of our electrically resonant modulator research is to investigate modulators that achieve enhanced modulation performance compared to their wider bandwidth counterparts.

8.2.1 Approach

We are focusing our immediate efforts on resonant optical modulators that are compatible with the free space structures described in Sec. 8.1. Once the general principles have been demonstrated, similar concepts will be applied to resonant inline modulators.

The voltage across a capacitor in a series circuit at resonance can be very high, which implies good modulation efficiency at the resonant frequency. The lumped element capacitor that will be used in a series resonant circuit is the free space modulator described in Sec. 8.1. The challenge is to fabricate a good low loss inductor operating in the microwave range using a thin film polymer.
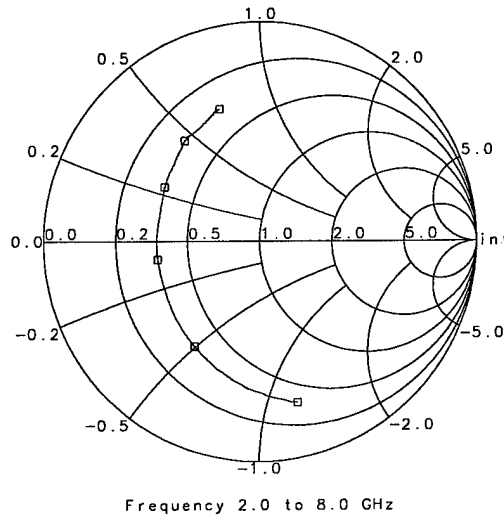
Figure 66: Smith chart plot of a series resonant circuit with promising characteristics for use in a resonant modulator.

8.2.2   Modulators Incorporating Series Resonance

Several resonant microwave circuit designs were fabricated on a PMMA dielectric layer and characterized. A capacitor, similar to the modulator, and a meander line inductor were fabricated on the top metal layer using the micro-machined laser ablation techniques (see Sec. 8.4 for more details). It was found that meander line inductors with good microwave performance can be implemented provided if the stray capacitance between the inductor and the ground is minimized by placing a gap in the ground plane below the structure. The results of these experiments were very encouraging.

The LC thin film structures fabricated with PMMA were characterized with a vector network analyzer. A coplanar waveguide probe was used to contact the circuit. Figure 66 shows a measurement of a structure where the measured resonant frequency corresponds to the design frequency of 4 GHz. The circuit is resonant at the frequency where it passes through the real axis on the Smith chart. The resistance is approximately 35 ohms, indicating a low Q for the resonant circuit. In the resonant modulator the modulating voltage will be twice as large as any achievable non-resonant capacitive modulator, even with this low Q.

We have started the fabrication of modulators that use the electro-optic polymer as the dielectric layer forming the capacitor in the series LC circuit. The capacitor is the reflective Fabry-Perot modulator described earlier.

8.2.3 Future Work

New RF-photonic concepts could be implemented if arrays of efficient resonant thin film polymeric modulators can be fabricated. Such electro-optic modulators are compatible with the processing used in microwave multi-chip modules and can be integrated into hybrid microwave-optical systems using phase shifters or quadrature modulators.

The initial results from the resonant structures are promising, and there are ways to further improve the circuit Q. The main limitation is the inductor and improvements to the inductor design—thus fabrication are needed. Once the resonant free space modulators have been completed, the same methods will be applied to the in line fiber modulators to enhance their modulation efficiency at a single frequency.

8.3   Microwave in-line fiber analog modulators with an improved modulation efficiency

The in-line fiber modulator is an amplitude modulator that operates by changing the optical transmittance of an uninterrupted optical fiber. The modulator consists of a lower, partially transmitting thin metal electrode, a corona-poled electro-optic polymer waveguide layer, and an upper, optically thick metal electrode deposited onto the surface of a fiber half-coupler. The electrodes form a microstrip line used to modify the coupling between the fiber and the polymer planar waveguides. The device is designed so that its optical transfer function has a steep slope at the optical bias point (wavelength of operation). To date, we have been able to obtain a bandwidth that well exceeds 20 GHz, although the maximum modulation efficiency (0.5 % with 5 V) is too low. Presently the modulation efficiency is limited because the interaction length is limited to less than a millimeter and the electro-optic coefficient of the polymer that was used is less than 10 pm/V. Since the bandwidth goals have been largely met, efforts are now being concentrated on to increase the modulation efficiency to at least 5 % at 5 Volt.

To meet this objective, we focused our efforts in the past year on:

1. Obtaining a detailed understanding of the fundamentals involved in the evanescent coupling over long distances occurring between the optical fiber and the electro-optic overlayer.

2. Identifying materials that satisfy the specific needs of long interaction devices. In addition to a large r-coefficient electro-optic polymer that is physically and chemically stable, a thin film is needed that has high conductivity and also low optical loss in the 1.3-1.5 μm range.

3. Developing flexible micro-fabrication techniques that are consistent with the processing requirements of new materials and capable of prototyping new long interaction length structures.

8.3.1 Mode-coupling in long interaction length inline fiber devices

The mode coupling over long interaction lengths between the cylindrical optical fiber waveguide geometry and the planar waveguide geometry of the polymer layer is significantly more complicated than couplers that use waveguides of similar shape. When two waveguides, with propagating modes with comparable effective indices are brought into proximity, two compound modes form with a slight difference in the propagation constant, $\Delta\beta$. Thus $\Delta\beta$ induces a relative phase difference between the two compound modes which accumulates as the modes propagate along the device. At a relative phase difference of π, the light has coupled from one waveguide to the other, and at 2π it has returned to the first waveguide. However, as the wavelength changes, $\Delta\beta$ also changes because of material and waveguide dispersion, leading to a change in the period of oscillation between the waveguides. This gives rise to the oscillatory exchange of power between the two waveguides that is dependent upon wavelength. Over a long interaction length, the light may undergo multiple oscillations between the fiber and the planar guide while propagating through the device.

Moreover, the coupling in inline devices is complicated by several factors. For example, the strength of the coupling changes over distance because the distance between the fiber and the polymer waveguide is not constant. The combination of the half-coupler and waveguide results in an asymmetric directional coupler. While the effective indices of the modes are matched, the field profiles in the two waveguides are vastly different. This fact alone makes the existing coupled mode analysis too simplistic. For such reasons, to obtain an improved understanding of the interactions that take place in an inline fiber device over long interaction lengths, we have conducted a detailed theoretical investigation using the beam propagation method (BPM) and compared the theoretical results to experimental measurements on precisely controlled geometries.

Experiments were conducted using a half-coupler that consists of a side-polished 1.33 μm single mode optical fiber affixed in a segmented silicon v-groove. This particular half-coupler had a very large radius of curvature. When a polymer film was placed on the side-polished fiber, the large radius of curvature of the v-groove half-coupler ensured that the length of the polymer film, and not radius of curvature, mainly determined the interaction length. Using a lift-off polymer deposition technique,[24] a film of the electro-optic polymer was adhered onto the surface of the half-coupler. Transmittance scans (Figure 67a) of the inline half-coupler were measured with a polarized white light source and an optical spectrum analyzer. The BPM was used to numerically simulate the coupling between the fiber and the planar guide as the light propagated through the half-coupler. Figure 67b shows the simulated transmittance scan. The BPM results not only quite accurately predicted the minimum transmittance wavelength, but also the ripples in the wings that were not predicted in previous simulation attempts using coupled mode theory methods. A detailed description of the experimental and theoretical work has been reported.[25]

This theoretical and experimental investigation indicated that the transmittance spectrum
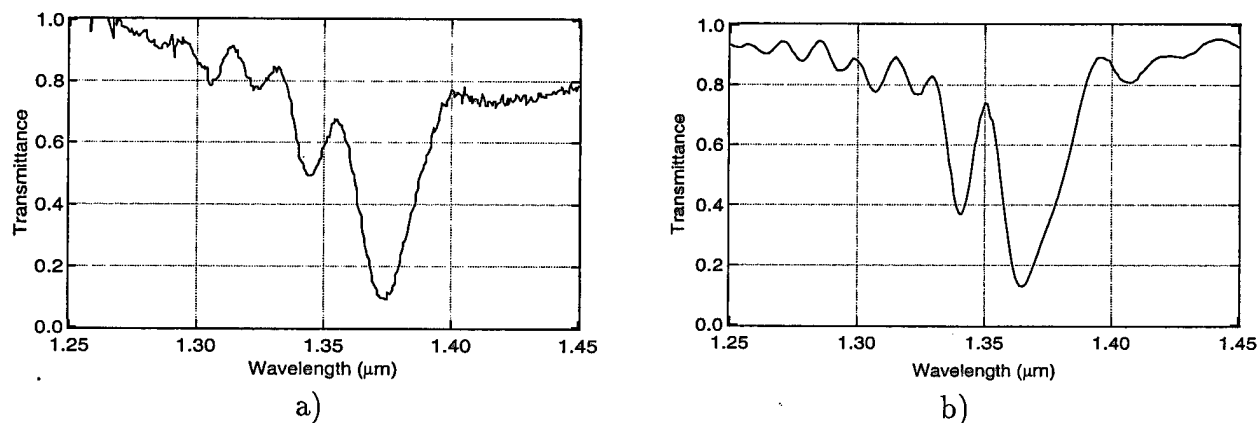
Figure 67: (a) Experimental and (b) simulated transmittance scans for a half-coupler with an electro-optic polymer overlayer. The device interaction length was trimmed to a 1 mm length by laser ablation.

of light leaving the device present sharp spectral features. These narrow transmission features offer the potential of increasing the modulation by at least a factor of 6 - 7, provided that a) the interaction lengths can be well-defined and b) there is no excessive loss mechanism over the interaction length that will damp coupling between the fiber and planar waveguides.

8.3.2 Materials for long interaction length inline couplers

Low loss propagation

The microstrip line is the most efficient modulator geometry because it offers the largest electric field in the electro-optic poled polymer. The electric field is applied over a thin film directly along the largest r-coefficient induced by corona poling, and is applied with the microstrip and a thin conductive layer between the fiber and the planar waveguide. The main challenge in obtaining a narrow, sharp transmittance feature is to fabricate a microstrip with an electrode plane that has a low optical absorption in the 1.3-1.5 μm range. Modulators do not yield ripples when fabricated with a partially transmitting Au ground layer between the polymer and the polished fiber because the optical losses are too large.

The first conducting, optically transparent material considered was indium tin oxide (ITO). However, this commonly used transparent electrode has two main drawbacks for inline modulators. ITO has a significant absorption at 1.319 μm and the deposition procedure involves temperatures around 300 degrees Celsius. An alternative is a commercially available conductive polymer 3,4 ethylenedioxythiophene (EDT) that can be deposited with excellent adhesion to glass surfaces. An EDT film can be deposited by spin coating, dipping, or spraying. Furthermore, we performed conductivity and transmittance measurements which were encouraging. A spin-coated EDT 1.7 μm thick film had an 85 % transmittance at 1.3 μm and a conductivity of approximately 4.0 kΩ/sq. In comparison, a 15 nm semi-transparent Au film has larger electrical conductivity, but has a transmittance of less than 15 % at 1.3 μm. Work is continuing towards

integrating EDT into an inline modulator.

Large r-coefficient Polymers

We have initiated collaboration with professor Larry Dalton's group at the University of Southern California to integrate their electro-optic polymer, which has very large r-coefficients, into inline fiber modulators. Being able to precisely control the thickness of the polymer is very important. We confirmed that we could process (spin-coating, pole, lift-off) the USC polymer to a well-controlled thickness required for an inline fiber device operating at a fixed wavelength in the 1.3-1.5 μm range. The polymers have a large r-coefficient but at the present time the relatively low glass transition temperature is presenting a problem for the fabrication of inline modulators. We have identified a metal deposition-processing step during the fabrication process that exposes the polymer to close to 100 degree Celsius for an extended time-period. If the processing temperature is close to the polymer glass transition temperature, the polymer depoles and the electro-optic coefficient is reduced. As a result, we are in the process of integrating sputtered metallic films into the fabrication process of inline fiber modulators which will reduce processing temperatures.

8.4   Micro-fabrication techniques for inline modulators

The development of a new device concept is traditionally performed using well-established materials. This is not the case in the development of inline fiber modulators. Instead, the materials (e.g. electro-optic polymers and low optical loss conducting polymers) continue to evolve with the evolution demanding a highly flexible fabrication technique for the microwave thin film electro-optic structures. We have developed laser micro-machining techniques for inline fiber structures to a) implement microwave transmission line structures on the electro-optic polymers, and b) define the optimal interaction length that provides the narrowest optical transmission features. The laser ablation system that we used was a doubled Nd:YAG laser, coupled through a microscope. The laser ablation system was fitted with a video system and a variable rectangular marker that indicated the region to be removed. For a 20X objective, the marker dimensions varied from 10 to 160 μm.

Microstrip transmission lines for inline fiber modulators were fabricated using the laser ablation technique and it was confirmed that acceptable performance could be obtained. For the inline microstrip geometry, the ground plane was placed between the optical fiber and the electro-optic polymer. The signal electrode was fabricated on top of the electro-optic polymer. Starting from a 1.0 nm Ti, a 200 nm thick Au layer uniformly evaporated onto the surface of the electro-optic polymer, and a 50 ohm characteristic impedance transmission line was laser ablated onto the surface. The dimensions of the signal conductor are 20 μm wide and 800 μm long. The length of the signal electrode corresponds to optimal interaction lengths predicted
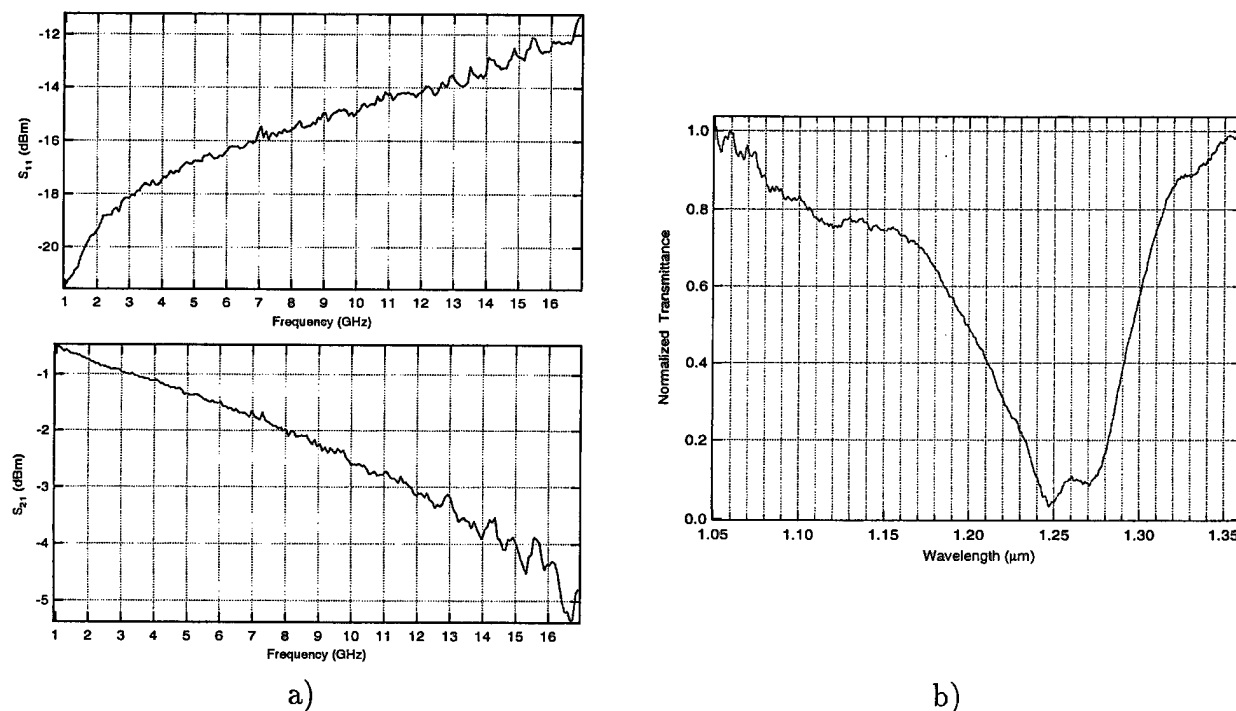
Figure 68: (a) Scattering parameters for the laser-ablated microstrip transmission line. (b) Transmittance characteristics of the laser ablated traveling wave in-line modulator.

by BPM. During the ablation process the signal electrode was aligned to the fiber by observing the fiber cladding edges. Network analyzer measurements are shown in Figure 68a. At 11 GHz, S_{21} is -3 dB while S_{11} is -14 dBm. This indicates that the laser-ablation fabrication method can produce RF transmission lines with optimum characteristics.

Unfortunately, the interaction length was too short on the half-couplers that we used in our previous demonstrations. Thus, the long interaction length half-couplers that we now use are developed in collaboration with Dr. Shiao Min Tseng of the National Tsing Hua University in Taiwan. The new half-coupler's fiber cladding has a flat polished surface at approximately 0.75 μm proximity to the fiber core and approximately 15 mm interaction length. This interaction well exceeds the optimum length. The approach that we follow is to deposit a polymer film that exceeds the optimum length and then, while performing in-situ white light optical transmissions measurements through the optical fiber, we reduce the polymer length by laser ablation until optimum optical transmission characteristics are obtained. The ablation procedure is stopped once the wavelength of operation falls in the edge of the transmittance dip. Figure 68b shows a transmittance scan after the ablation procedure for a device that incorporates a semi-transparent Au layer between fiber and planar guide. Considering the losses inherent to the Au layer, the transmission features are considerably narrower that what was measured at longer interaction lengths. In future devices, to reduce the optical losses, the gold electrode will be substituted by a conductive polymer. The expectation is that we will be able to obtain narrow transmittance

dips comparable to that shown in Figure 67a.

8.4.1 Future Work

The material and fabrication improvements are important milestones towards obtaining our goal of demonstrating a microwave inline analog modulator with 5 % modulation efficiency at 5 V. To meet this objective we are establishing a reliable process flow that integrates the new developments of a) the low optical loss conducting polymer for thin bottom electrode, b) the low-temperature deposition of metallic films for the signal electrode, c) the laser ablation fabrication technique to define the optimum transmission characteristics, and d) the laser ablation fabrication technique to define a microstrip transmission line.

8.5 Other Related Activities

The flexibility of integration of half-couplers with materials other than electro-optic polymers have made possible a collaboration with J. S. Harris' group at Stanford University. The new devices incorporate GaAs/AlGaAs as electro-optic material for efficient, but low speed, amplitude modulation. Other GaAs/AlGaAs devices were also fabricated that exploit the transfer of light from the fiber to the planar waveguide for distributed optical detection applications.

The GaAs/AlGaAs multiple-quantum-well in-line fiber optic intensity modulator is based on the evanescent wave coupling between a GaAs/AlGaAs multiple-quantum-well waveguide and a single-mode fiber. This device concept combines the inherent advantages of in-line fiber devices with GaAs integrated optoelectronics. The modulator consists of a GaAs/AlAs multiple quantum well (MQW) core layer, and a AlAs/AlGaAs distributed Bragg mirror (DBR). When the wafer is attached epi-side down to a half-coupler, waveguiding is achieved in the core layer by reflection from the DBR and total internal reflection from the fiber cladding. The difficulty of phase matching between the semiconductor waveguide and the fiber, made up of two materials with vastly different refractive indices, is overcome by the use of the Bragg mirror, which is designed to provide high reflection for a specific mode angle. The optical wave in the semiconductor waveguide can therefore propagate with very low effective indices, making it possible to phase match to the single mode fiber. Because the two waveguides have very different dispersion curves, phase matching occurs only at specific wavelengths. By applying an electric field perpendicular to the plane of the quantum wells, the complex index of refraction of the MQW layer is changed through the quantum confined Stark effect, which results in both a shift in the phase-match wavelength and a change in the shape of the resonance dip. Therefore, intensity modulation of the transmitted light through the fiber can be obtained. Initial structures show a modulation contrast $\Delta T/T$ of more than 53 %, with an applied voltage of 5 V.[26]

The optical detector has a construction very similar to the amplitude modulator but, to maximize quantum efficiency, the quantum well was placed at the center of the core where the

intensity of the guided GaAs/AlAs waveguide mode was maximum. As in other half-coupler devices, the photodetector extracts, and therefore detects, light at a specific wavelength traveling through a fiber. The extracted light is absorbed by the quantum well, generating a photocurrent. The detector's distributed absorbing configuration is conducive to high-speed, high-power operation. The full width at half-maximum of the photocurrent response is 1.6 nm, and the external quantum efficiency is 75 %.[27]

8.6 PILF modulator progress

Table 7 describes the activity schedule for the period between February - September 2000. The table indicates if the activities have been completed or are still in progress.

8.6.1 Planned Activities for years 4 and 5.

The activities outlined below for year 4 are explained in more detail in the March-August 2000 report. The activities for year 5, to be initiated in year 4, constitute a new research avenue based on findings in a previous period.

Year 4:

Activities will need to continue to improve the efficiency of microwave in-line fiber analog modulators. This will involve increasing the slope of the device transfer function by precisely controlling the device interaction length and by using a transparent electrode between the fiber and nonlinear polymer waveguide. Also, we will continue activities to incorporate the latest high r-coefficient polymers under development by the University of Southern California.

With respect to the resonant thin film in-line fiber modulators, activities will be conducted to incorporate the resonant circuits that have been tested into the in-line devices. Activities will be conducted to improve the Q of the resonant circuits in order to significantly enhance the modulation efficiency.

The feasibility study conducted during the last 6 months for RF optical interconnect free space high frequency polymer analog modulators was very successful and will be pursued in more detail. The final goal is to test a modulator arrays and test configurations where devices within the array are driven at different frequencies.

Year 5:

Research activities are proposed to increase the modulation efficiency to higher levels by using stimulated Brillouin scattering (SBS) carrier suppression techniques similar to the ones followed by D. Dolfi at Thompson-CSF. SBS in optical fibers with lengths of less than 1 km require optical powers that can easily exceed 100 mW. Carrier suppression becomes practical in inline modulators because it has been demonstrated that they can withstand the high optical carrier

Table 7: High Speed Polymeric Modulator Progress

Current Progress	Completed	In Progress
Microwave In-line Fiber Analog Modulators - Fabrication and test of laser ablated microstrips on glass slides using thin Au layer and DR1 on glass slides	×	
- Fabrication and test of laser ablated microstrips on glass slides using transparent electrode layer and DR1 on glass slides	×	
- Fabrication and test of laser ablated micrsotrip on glass slides using USC polymer and transparent electrode on glass slides	×	
- Optimization of ADCM dip position and width using USC polymer (polymer poled by USC)		×
- Fabrication of modulator with laser ablated microstrip and USC polymer	×	
- Measurement of USC polymer refractive index and r-coefficient		×
Free-space High-frequency Polymer Analog Modulators - Fabrication of Microstrip Reflection Fabry-Perot (MRFP)	×	
- Test of MRFP's	×	
Resonant Thin-film In-line Fiber Modulators - Design and fabrication of resonant thin film in-line fiber modulators		×
- Testing of resonant modulators		×

power levels. Testing will be performed using an intense narrow band optical carrier that will be amplitude modulated at microwave frequencies by an in-line modulator. The modulated carrier will then be injected into a length of single mode fiber in which SBS narrow band filtering will be used to suppress the optical carrier by a factor in excess of 2, while the intensity of modulated sidebands will be, to a very good approximation, not reduced. Considerable improvements in the modulation efficiency are expected while maintaining the large spurious free dynamic range available from the in-line modulators. Once efficient SBS carrier suppression is achieved, then the approach can also take advantage of the large dynamic range of the in-line modulator, which will result in microwave broadband electro-optic modulator technology that has modulation efficiency,

dynamic range, and noise figure parameters well in-excess of what can achieved with single and multiple modulators configurations using Mach-Zehnder devices.

9 Technical Summary

Our MURI functions as a well-integrated team consisting of three researchers specializing in the various aspects of optical systems, including Prof. Anderson (photorefractive systems), Prof. Wagner (acoustooptic and adaptive systems) both at CU, and Prof. Babbitt (photon echo systems) at MSU, who are assisted by the signal processing expertise and guidance provided by Prof. Griffiths at GMU, the RF and microwave expertise of Prof. Popovic at CU, and the new modulator technology of Prof. Knoesen at UC Davis. Numerous industrial collaborations with groups at Hughes, Lockheed-Martin, Rockwell, Boeing, Thomson CSF, and the Netherlands Foundation for Radio Astronomy (among others) help guide and focus our applications.

Key developments during the third year of this MURI in RF Photonic Systems include broadband adaptive beam forming using BEAMTAP, a fully-adaptive true-time-delay optical array processor operating at lower frequencies, a practical multiple exposure technique for photon echo time delay, a 5i GHz free space polymer modulator, an extremely compact novelty filter and two beam coupling carrier suppression system, and an integration between RF antennas and an all-optical photorefractive processor.

9.1 BEAMTAP

During year 3 various traveling fringe detectors from Thomson have been incorporated in the BEAMTAP processor and optimized for large time delay and good dynamic range. Read-write isolation has been incorporated using a novel polarization multiplexing scheme, which is a vital step towards the completion of the final jammer nulling system since it is required in order to close the adaptive feedback loop. Beam forming over an 80 MHz bandwidth with read-write isolation has been successfully demonstrated, and closed loop operation will be achieved shortly. In year 4 the bandwidth should be increased to 500 MHz so that the full broadband nature of the beam forming and jammer nulling BEAMTAP system can be realized.

9.2 Optical Coherent Transient True-Time-Delay

Theoretical and numerical studies of Maxwell-Bloch equations have identified a new regime capable of 7% diffraction efficiency at an absorption length $\alpha L = 3.5$, which is more than an order of magnitude improvement when compared to thin materials. Short-pulse multiple exposure programming of true-time-delay optical coherent transient gratings covering the full 17 GHz material bandwidth has been demonstrated and a 2 GHz 4-bit waveform has been programmably delayed by up to 12 ns. Novel Ti:Sapphire laser stabilization by locking to a spectral hole has improved laser stability from a 500 kHz linewidth to just 6 kHz, which has enabled multiple exposure recording of low bandwidth, dynamically-programmable delay gratings. Injection locking of a high power 70 mW laser to a 100 μw modulated signal, as well as a novel fiber amplifier at

793nm, have been developed to provide the necessary power for high bandwidth, optical coherent transient processing. Detection of a phase modulated signal by a novel demodulation scheme using spectral filtering in Tm:YAG has also been demonstrated out to 13.5 GHz without the complexities of interferometric heterodyne detection.

9.3 High-speed Polymeric Modulators for Photonic Array Antennas

Free space polymer analog modulators operating as off-axis electro-optic Fabry-Perot amplitude modulators at 1064 nm with 5 GHz bandwidth in an area of only 140×140 μm have been developed as miniature RF front-end modulators appropriate for high frequency array applications. More efficient and higher dynamic range polymer-in-line fiber (PILF) modulators are being developed which incorporate new high electrooptic-coefficient polymers and long interaction-length half-couplers utilizing laser-ablated micro machining with performances of .5 % at 5 V modulation at over 20 GHz bandwidth. The goal of 5 % modulation depth at 5 V has already been achieved using GaAs/AlGaAs quantum well DBR in-line fiber-optic modulators, and should soon be observed in improved polymer devices.

9.4 Optically Smart Antenna Array

An RF front end that down converts X-band signals from antennas provided by Prof. Popović into lower frequency EO modulators and then into the photorefractive optical processor has been developed. A photorefractive two-beam coupling carrier suppression system has been designed, analyzed, and optimized with a novel operator method which has resulted in a carrier suppression of 64 dB, which (to our knowledge) is the best carrier suppression achieved to date. A miniaturized auto-tuning filter has been developed with a contrast enhancement of 26 dB/dB, requiring only 5 mW of optical power, a bandwidth of 3 GHz, in a volume of only 3 cm³, all improved by an order of magnitude from last year.

9.5 Optically-Switched Active Antenna Array

The fastest, lowest power, optically controlled X-band switch to date has been demonstrated, achieving 36dB isolation over with only 0.3dB loss over several GHz bandwidth and a switching speed approaching 2 ns. A complete transmit/receive (T/R) quasi-optical (QO) active-antenna array with optical control was designed, built, and demonstrated using this switch, along with the low-cost multi-mode fiber control. The QO front end has been integrated into an optical processor capable of receiving two signals from any direction and adaptively separating the stronger signal from the weaker, while simultaneously increasing the contrast ratio between the two signals.

References

[1] G. Kriehn, A. Kiruluta, P. E. X. Silveira, S. Weaver, S. Kraut, K. Wagner, R. T. Weverka, and L. Griffiths, "Optical BEAMTAP beam-forming and jammer-nulling system for broadband phased-array antennas," *Applied Optics*, vol. 39, pp. 212–230, January 2000.

[2] G. Kriehn, G. S. Pati, P. E. X. Silveira, F. Schlottau, S. Weaver, and K. Wagner, "Experimental demonstration of broadband adaptive beam forming using the beamtap algorithm," in *PSAA-10*, DARPA, February 2000.

[3] G. R. Kriehn, P. E. X. Silveira, G. S. Pati, F. Schlottau, and K. H. Wagner, "Beamtap rf-photonic adaptive-array processing," in *Interactions between Microwaves and Optics*, OMW, August 2000.

[4] G. Kriehn, G. S. Pati, P. E. X. Silveira, F. Schlottau, K. Wagner, and D. Dolfi, "Demonstration of optical beam forming using beamtap," in *International Workshop on Photonics for Antennas*, MWP, September 2000.

[5] S. Meridith and A. Crowley, "Smart system antennas," in *Mobile Radio Technology*, 1997.

[6] B. Widrow and S. D. Stearns, *Adaptive Signal Processing*. Prentice-Hall, 1985.

[7] P. Yeh, *Introduction to Photorefractive Nonlinear Optics Chapter 4*. J. Wiley and Sons, 1983.

[8] D. Z. Anderson and J. Feinberg, "Optical novelty filters," *IEEE Journal of Quantum Electronics*, vol. 25, pp. 635–647, March 1989.

[9] J. Khoury, V. Ryan, M. Croningolomb, and C. Woods, "Photorefractive frequency-converter and phase-sensitive detector," *J-Opt-Soc-B*, vol. 10, pp. 72–82, 1993.

[10] R. Montgomery and R. Desalvo, "A novel technique for double side-band suppressed carrier modulation of," *IEEE Photonics Technology Letters*, vol. 7, pp. 434–436, 1995.

[11] S. Tonda-Goldstein, D. Dolfi, J.-P. Hiugnard, G. Charlet, and J. Chazelas, "Stimulated brillouin scattering for microwave signal modulation depth increase in optical links," *Electron. Lett*, vol. 36 no. 11, pp. 944–6, 200.

[12] D. Z. Anderson, R. Brockett, and N. Nuttall, "Information dynamics of photorefractive two-beam coupling," *Phys. Rev. Lett*, vol. 82 no. 7, pp. 1418–21, 1999.

[13] T. Baer *Opt. Lett*, vol. 12 no. 6, pp. 392–4.

[14] W. Rotman and R. F. Turner, "Wide-angle microwave lens for line source applications," *IEEE Transactions on Antenna and Propagation*, vol. 11, pp. 623–632, Nov. 1963.

[15] D. T. McGrath, "Planar three-dimensional constrained lens," *IEEE Transactions on Antenna and Propagation*, vol. 34, Jan. 1986.

[16] Z. Popović, "Quasi-optical transmit/receive front ends," *invited paper, IEEE transactions on Micorwave Theory and Techniques*, vol. 48, pp. 1964–1975, Nov. 1998.

[17] S. Hollung, A. Cox, and Z. Popović, "A bi-directional quasi-optical lens amplifier," *IEEE Transtransactons on Microwave Theory Techniques*, vol. 45, pp. 2352–2357, Dec. 1997.

[18] P. J. Stabile, A. Rosen, and P. R. Herczfeld, "Optically controlled lateral pin diodes and

microwave control circuits," *RCA Review*, pp. 443–456, Dec. 1986.

[19] J. Freeman, S. Ray, D. West, A. G. Thompson, and M. J. LaGasse, "Microwave control using a high-gain bias-free optoelectronic switch," *Optical Technology for Microwave Applications SPIE*, vol. 5, pp. 320–325, 1991.

[20] S. S. Gevorgian, "Short-circuit photocurrent-controlled microwave pin diode switch," *Microwave and optical Technology Letters*, vol. 7, pp. 553–555, Aug. 1994.

[21] C. L. Goldsmith, Z. Yao, S. Eshelman, and D. Denniston, "Performance of low-loss RF MEMS capacituve switches," *IEEE Microwave and Guided Wave Letters*, vol. 8, pp. 269–271, Aug. 1998.

[22] E. R. Brown, "RF-MEMS switches for reconfigurable integrated circuits," *IEEE Transtransactons on Microwave Theory Techniques*, vol. 46, pp. 1868–1880, Nov. 1998.

[23] D. Yankelevich, R. Hill, A. Knoesen, M. Mortazavi, H. Yoon, and S. Kowel, "Polymeric modulator for high-frequency optical interconnects," *IEEE Phot. Tech. Let.*, vol. 6, no. 3, pp. 386–390, 1994.

[24] G. Khanarian, M. A. Mortazavi, and A. J. East, "Phase-matched second-harmonic generation from free-standing periodically stacked polymer films," *Appl. Phys. Lett.*, vol. 63, p. 1462, 1998.

[25] C. Arft, D. R. Yankelevich, A. Knoesen, E. Mao, and J. S. Harris, "In-line fiber evanescent field electrooptic modulators," *J. of Nonlinear Optical Phys. & Mat*, vol. 9, p. 79, 2000.

[26] E. Mao, C. Coldren, J. Harris, D. Yankelevich, O. Solgaard, and A. Knoesen, "Gaas algaas multiple-quantum-well in-line fiber intensity modulator," *Appl. Phys. Lett.*, vol. 75, no. 3, pp. 310–312, 1999.

[27] E. Mao, D. Yankelevich, C.-C. Lin, O. Solgaard, A. Knoesen, and J. Harris Jr., "Wavelength-selective semiconductor in-line fibre photodetectors," *Electron. Lett.*, vol. 36, p. 515, 2000.